論文 / 著書情報
Article / Book Information

題目(和文)	
Title(English)	Simulation of Fluid Dynamics with Uncertainty Based on Polynomial Chaos Expansion
著者(和文)	ｼﾞﾝｼﾞｮﾝ ﾌﾝ
Author(English)	Jonghoon Jin
出典(和文)	学位:博士(工学), 学位授与機関:東京工業大学, 報告番号:甲第11267号, 授与年月日:2019年9月20日, 学位の種別:課程博士, 審査員:肖 鋒,奥野 喜裕,青木 尊之,末包 哲也,長﨑 孝夫
Citation(English)	Degree:Doctor (Engineering), Conferring organization: Tokyo Institute of Technology, Report number:甲第11267号, Conferred date:2019/9/20, Degree Type:Course doctor, Examiner:,,,,
学位種別(和文)	博士論文
Type(English)	Doctoral Thesis

Simulation of Fluid Dynamics with Uncertainty Based on Polynomial Chaos Expansion

by

Jonghoon Jin

Supervisor : Feng Xiao

A Dissertation Submitted in partial fulfillment of the requirements for the degree of

Doctor of Philosophy

Department of Mechanical Engineering

Tokyo Institute of Technology

June 2019

Contents

List of Figures

List of Tables

Chapter 1

Introduction

1.1 Background

Numerical simulation of fluid dynamics has been developed to analyze the behavior of fluid flow and attain useful knowledge for fluid flow related problems. A series of methodologies to numerically simulate the behavior of fluid flow using a computer is called computational fluid dynamics(CFD). CFD is mainly consisted by three separated elements: pre-processing, numerical solver, and post-processing. Pre-process is where the problem condition is interpreted as a numerical setting. Generation of geometric mesh and formulation of calculation condition is contained here. Selection of numerical scheme to conduct numerical simulation and determination of model parameter of a numerical model should be done in this step. Once a geometric mesh and calculation condition, a computer can simulate the determined numerical model according to the selected numerical scheme and calculate out numerically attained physical quantities. The coded numerical scheme to conduct this step is the numerical solver. These calculated quantities, also, can be processed and visualized to attained some useful information to get the knowledge to solve scientific or engineering problems.

Development of numerical simulation does not only restricted to generation and improvement of high precision numerical schemes by which the governing equation of fluid dynamics in numerically solved, but also includes enhancements of pre-processing and post-processing. Refined geometric mesh and development of the refined physical model

have contributed to the broad usage of numerical simulation in fluid phenomena. Also, post-process techniques of calculation results, such as Fourier transform or proper ordinary decomposition, enabled efficient analysis of simulation result. These developments of high precision numerical scheme and step up improvements in post-processing and pre-processing have made CFD the necessary tool for various fluid flow related engineering field ranging in classical hydrodynamics to turbomachinery with drastic development. Using developed CFD system, numerical analysis of the behavior of the fluid, which has not been solved from analytical approaches, has become enabled. Moreover, physical quantities of fluid flow, which could be difficult to be measured directly from the experiment, can be attained and visualized. These benefits of CFD provide engineers useful information to attain the knowledge to solve the fluid related engineering problems. There are increasing needs for more enhancement and continuous improvement of CFD for application and usage for the development of engineering.

With the increasing usage of CFD, how to validate the confidence and reliability of CFD system became an important problem. There are approaches to standardize validation methodology of CFD system[37–41,49]. These approaches have reached common validation process[38,41] in figure 1.1. In this validation process, a real phenomenon is evaluated based on experiment and computation, separately, and the computational solution is validated with the comparison of the experimental data. The difference between the computational solution and experimental data has resulted from the existence of error and uncertainty in computation and experiment.

For the experimental process, experimental data are attained from the experimental setup, which reproduces the real phenomenon in an experimental condition. Attained experimental data inevitably include experimental error and uncertainty. Lack of knowledge of the real phenomenon or assumption of the experimental condition could result in the difference between real phenomenon with the experimental setup. Moreover, measurement error always inherent in every experimental measuring process.

For computational process, the real phenomenon is conceptualized as a conceptual model, a theoretical representation of the real phenomenon, based on knowledge of fluid dynamics, engineering, and mathematics. As same as when I mentioned about the experimental setup, unknownness or intentional simplification result in error and uncertainty on

this step. With the conceptual model, a computational model based on discretize methodology, like the finite difference method, finite element method, or finite volume method, is generated. Due to spatial and temporal discretization and assumptions for discretization, error, and uncertainty are included in this step. Determination of physical quantities; viscosity, turbulence parameter, etc, also includes uncertainty. When the computational solution is attained from the computational model, numerical error, and uncertainty in calculation condition are included with the resulted solution.

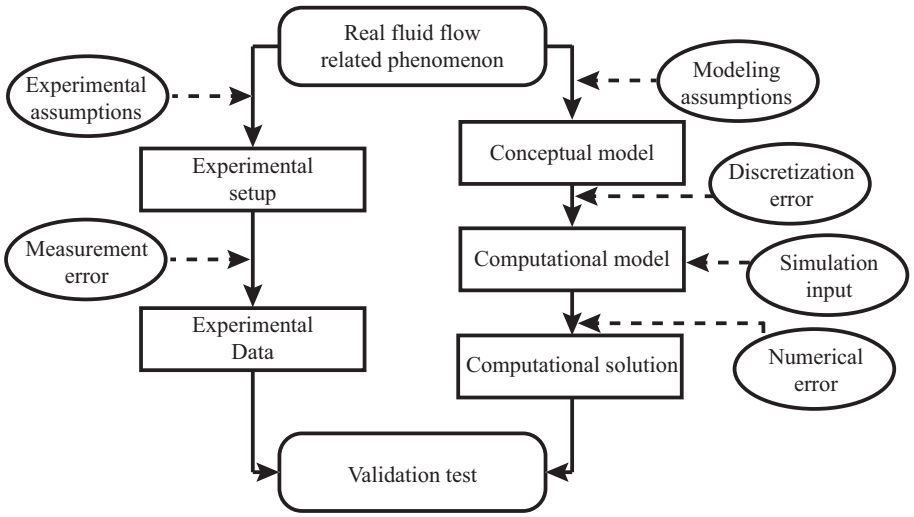

Fig.1.1: Validation process

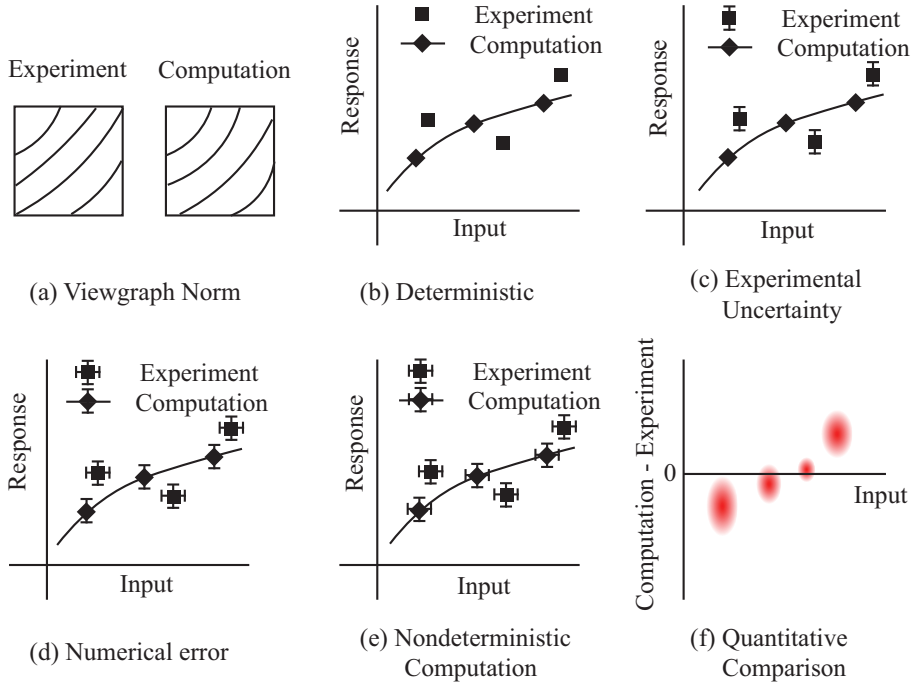

Fig.1.2: Validation metrics[66]

To validate the CFD system, the error and uncertainty in the computation solution and experimental data should be identified and quantified, at first. After quantification of error and uncertainty of the computation solution and experimental data, they could be compared to evaluate the validity of the CFD system. To help understanding the need of quantifying uncertainty of computation solution, I will represent the categorization of validation metrics by T.G Trucano et al.[66] in figure 1.2. Each validation metric is arranged in order to improve quality of validation in general aspect.

In the first figure, figure 1.2 (a), the viewgraph norm comparison of experimental data and computational solution based on the experimental picture and computational visualized figure are shown. With this veiwgraph norm, an expert could figure out the validity of the computational solution based on his knowledge about the problem phenomenon. Although the visualized figure gives us fluent information which cannot be attained with simple line graphs or scatters, viewgraph norm is not fordable to evaluate validity for general cases, because the quantitative comparison between experimental data and computational solutions is hardly attained.

Continuing 5 figures 1.2 (b-f) give us comparison of response (b-e) of computational

solution and experimental data or difference between compuational solution and experimental data(f). The deterministic validation metric, figures 1.2 (b), is the most simple validation metric with input–response space. Computational solution and experimental data are plotted as a deterministic dot inside input–response space and no information about reliability has provided. With consideration of experimental uncertainty, upper and downer whiskers representing the distribution of experimental data are introduced. The validity of the computational solution could be compared with the range of the error bars, as shown in figure 1.2 (c). For figure 1.2 (c), small improvement has occurred to experimental data, the uncertainty of input in the experimental setup has been considered as left and right whiskers. More importantly, the computational solution comes with upper and downer whiskers represent the numerical errors. From quantitative consideration of numerical error, validity could be discussed with more higher quality.

In remained two figures, figure 1.2 (e) and (f), the computational solution shows different characteristics compared with former explained figures. With these figures, not only the distribution of experimental data but also the distribution of input values has considered with the computational solutions. This statistical characteristic of the input values transfers to the computational solution, and the computational solution became a distribution. Because the input and the computational solution are not defined in a deterministic way, these computations are called as non–deterministic computation. For figure 1.2 (e), the statistical characteristic of the computational solution is represented by upper and downer whiskers. Standard deviation is generally chosen for these whiskers to represent statistical characteristic, and the marks indicate expectation value or mean. The most disable validation metric is a quantitative comparison between computation and experiment with the error and uncertainty are fully considered as shown in 1.2 (f). For the ideal quantitative comparison, the values are not discussed from the error bar. Instead, the values are discussed based on probability density function fully represent statistical characteristics, and it is represented as multidimensional distribution with red blurred ellipses.

As explained above precisely, for high quality validation of CFD system, not only the valid experience data , the numerical simulation itself should be performed with consideration of error and uncertainty. And the effect of uncertainty on fluid simulation result

should be represent explicit form using standard deviation or probability density function. In spite of this need and, error and uncertainty in experimental measurement has been a must do problem, the importance of the consideration of error and uncertainty in fluid flow simulation has a lot of rooms to study. In this thesis, simulation of fluid dynamics with consideration of error and uncertainty is performed based on polynomial chaos expansion.

1.2 Error and uncertainty in simulation of fluid dynamics

Before discuss about simulation of fluid dynamics with uncertainty, I will explain the definition of the word "uncertainty", because it has been used various concept. The term uncertainty had been broadly used in the field of measurement, before the discussion of uncertainty on CFD started.

A consensus in the word of error and uncertainty in measurement can be found in "Guide to the expression of uncertainty in measurement"(GUM) of the Joint Committee for Guides in Metrology[63]. In the document, error is define as "result of a measurement minus a true value of the measurand" and uncertainty of measurement is as "parameter, associated with the result of a measurement, that characterizes the dispersion of the values that could reasonably be attributed to the measurand ". They use variance and standard deviation concept to represent uncertainty as parameter, but explictly mentioning it is "for convenience of discussion only" and "evaluation are based on probablity distribition".

1.2.1 Classical classification

The term of error and uncertainty in communities related numerical simulation of fluid dynamics had been developed differently with measurement community[38–40,68], before recent verification and validation standard addressed by the American Society of Mechanical Engineers[41]. The approach of fluid simulation communities had been focused more on the procedures of validation process and philosophy of comprehensive validation. In spite, the current version of guideline adopted the definition of measurement community, mention of the guideline of the latter community will be precious for understanding characteristics of

error and uncertainty in CFD system and avoiding misunderstanding. In the classical approach, error is defined as "a recognizable deficiency in any phase or activity of modeling or experimentation that is not due to lack of knowledge" [40], and uncertainty as "a potential deficiency in any phase or activity of the modeling, computation, or experimentation process that is due to inherent variability or lack of knowledge" [40].

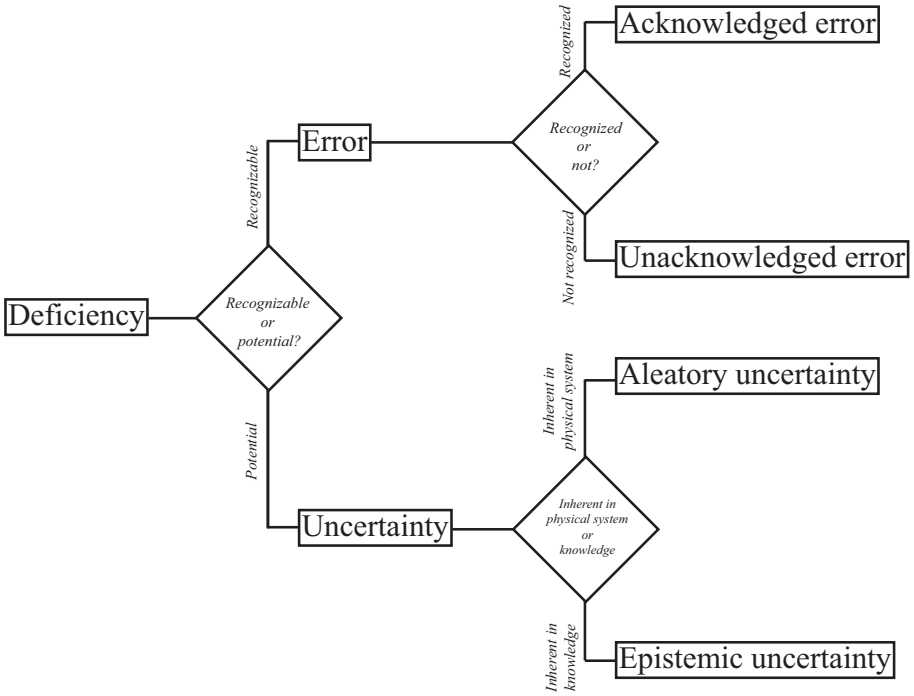

Fig.1.3: classical classification

Oberkampf et al. also have shown detailed clasification of error and uncertainty [39] as shown in 1.3. They categorized error recognized but accepted for limitation of computational resource as acknowledged error. Numerical error is an excellent example of this kind of error, and an expert can assume the effect of this kind of error on the computational solution. The human error or mistakes inside the code; so called bug, is categorized as an unacknowledged error which can be recognized but failed to be recognized. This kind of error is reducible, but the existence of this kind of error should be admitted and considered systemically.

About the uncertainty, they mentioned the existence of two different kind of uncertainty: aleatory uncertainty, inherent in a physical system based on the stochastic characteristic,

and epistemic uncertainty, caused by lack of knowledge. Uncertainty of simulation input: geometry, boundary condition, material properties, etc., is categorized as epistemic uncertainty, where a true value exists but cannot be attained generally. Stochastic features like turbulence and chemical reaction and uncertainties generated by simplifying assumption are classified as aleatory uncertainty.

1.2.2 Definition of uncertainty on current guideline

On the guideline of current version[41], the definition of measured community was applied to the simulation model. Without considering the characteristics of uncertainty classified with the classical approach, the current approach only considers the existence and size of uncertainty. With this definition of the current standard, a quantity distributes in the range is considered has uncertainty. With that quantity, the specific error is defined as a difference between a specific quantity and true value, which cannot be measured from its characteristics. And the uncertainty is discussed with the standard uncertainty range, where a certain percentage, mainly 95%, of the quantity inherent in that range as shown in figure 1.4(a). This concept of the standard uncertainty range enables consider uncertainty resulted from the experimental process and computational process coincidently and efficiently compared.

In this thesis, uncertainty is discussed with more developed form, a probability density function (pdf) as presented in figure 1.4(b). A quantity with uncertainty is considered as a random variable with continuous pdf reveals the probability of uncertainty. The nonlinearity of distribution can be considered from the shape of the probability density function. Moreover, the standard range can be easily attained from the probability measure.

1.2.3 Existence of uncertainty in CFD system

As shown in 1.1, each step of the CFD system source of uncertainty is inherent. For the simulation of a real phenomenon, an appropriate conceptual model should be constructed by specificating the case. In this modeling step, lack of knowledge to appropriate real phenomenon, mistake of model selection, or simplifying assumption with acknowledging for the existence of uncertainties. A mistake of model selection could be reduced with

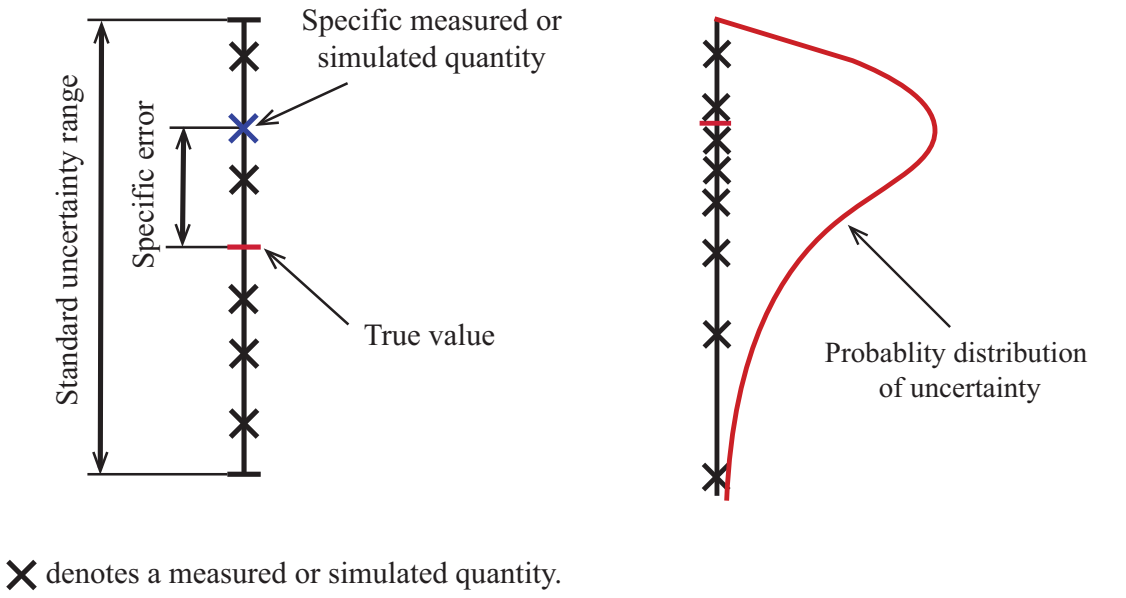

(a) Current standard (b) Probability distribution of uncertainty

Fig.1.4: standard definition of error and uncertainty in CFD

careful consideration with other unacknowledged errors. And simplifying assumption, categorized as an acknowledge error, is intentional and the effect of error could be estimated by experts. However, in case of lack of knowledge, a study or research to make clear the epistemic uncertainty, and disable converted as the acknowledged error. These uncertainties in modeling assumption should be considered and avoided priorly, but in case of acknowledged error, there is room for fluid flow simulation of uncertainty could clarify the effect of the acknowledged error. For the epistemic uncertainty on this step, the deterministic simulation could help understanding of the phenomenon.

When a computational model is generated from the conceptional model, discretization errors also generated. This kind of errors are acknowledged and should be carefully considered for continuing steps. The numerical error which has similar characteristics with the discretization error also considered and if possible, should be explicitly represented as 1.2(d).

The uncertainty included in simulation input is the most important uncertainty resource in this thesis. From the fact that the simulation input is also a measured or modeled value, the uncertainty is inherent. With different discretization error or numerical error,

the range of the uncertainty cannot be attained from analysis of CFD system. Instead, a simulation system should be able to transfer the uncertainty of simulation input to the calculation result. Projection of uncertainty in simulation input to simulation result is the essential concept of simulation of fluid dynamics with uncertainty.

1.3 Simulation of fluid dynamics with Uncertainty

Simulation of fluid dynamics could be represented as a projection via numerical solver from simulation inputs: calculation condition and model parameter, to a numerical solution, as shown in figure 1.5 (a). A deterministic numerical solver results out a unique numerical solution from the determined point from a determined calculation condition using a numerical model with model parameters. To consider the existence of uncertainty in simulation inputs, a non-deterministic formulation of the simulation system should be developed. Figure 1.5 (b) presents a breif formulation of a simulation system with consideration of uncertainty in simulation inputs. There is a red cross mark surrounded by a blue box inside the simulation input domain. The red cross is the expected value of simulation inputs, and blue box denotes the standard uncertainty range. Standard uncertainty range of calculation condition is represented as the width of the blue box, and that of the model parameter is as the height of the blue box. Due to this existence of uncertainty in simulation inputs, physical quantities inside the simulation system should be considered as a rand variable with stochastic characteristics, and the numerical solution also should be represented as an uncertain form with the standard uncertainty range. However, the non-linearity and non-monotonicity of fluid phenomena and flow solver makes it difficult to calculate the standard uncertainty range of numerical solution from the standard uncertainty range in the simulation input domain.

A preferred approach is to use of transfer of probability density function via numerical solver and evaluate the standard uncertainty range afterward. In this approach, the probability distribution of the uncertainty in simulation inputs is represented as a red blurred ellipse in figure 1.5 (c). This probability distribution is attained from the experimental measurement, theoretical consideration, or expert's assumption within the standard uncertainty range. This quantitative information of uncertainty is transferred via non-

deterministic numerical solver, and the numerical solution is attained as a form of the probability distribution. The attained probability distribution of the numerical solution could be represented as the expected value with the standard uncertainty range as figure 1.5 (b), using the statistical measures.

Simulation of fluid dynamics with uncertainty is strongly stimulated from the quantitative evaluation of uncertainty on the computational solution to validate the CFD system as above mentioned. However, the ability to analysis flow fluid phenomenon with non-deterministic way and attained stochastic characteristics inspired many other fields of research such as sensitivity analysis[60] , data assimilation[30], and machine learning[61].

1.4 Existing research of simulation with uncertain condition

The method to simulate the uncertainty condition has mainly three kinds of approach. The first one is random trial approaches. In random trial approaches, the response of the stochastic system is analyzed with a tremendous number of random trial. With this approach, the most accurate response could be attained with a sufficient number of trials, but extremely high calculation cost is needed. Monte Carlo simulation using complete random trial, and Latin hyperbolic sampling generated trial in evenly with the probability density function. The quasi-Monte Carlo method uses low discrepancy sequences.

The perturbative analysis effect of uncertainty from the response change of small perturbation. With assumption of small perturbation stochastic characteristics is usually solved analytically. But due to the assumption of the small perturbation, only small size of uncertainty could be analyzed.

With a spectral approach, the effect of uncertainty is represented as a series of orthogonal basis functions. From the orthogonality of basis function, the characteristic of uncertainty is evaluated with high convergence ratio. In Karhunen loeve expansion, a proper orthogonal function generated from eigenvalues is used as basis. With orthogonal polynomial basis polynomial chaos expansion has been developed[70,76]. Especially polynomial chaos expansion is research by many researchers after Ghanem[14] successfully adapted PCE method at finite element method. More detail about polynomial chaos expansion will be discussed on chapter 2. In this thesis, PCE is used to simulate fluid dynamics with

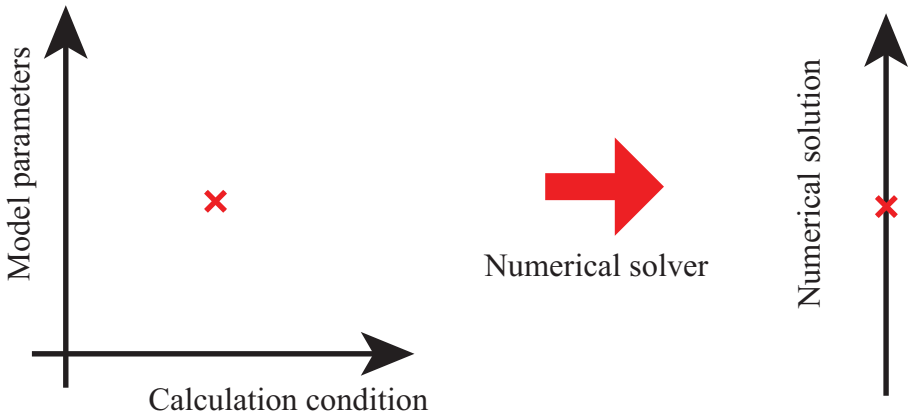

(a) Conceptional diagram of simulation of fluid dynamics

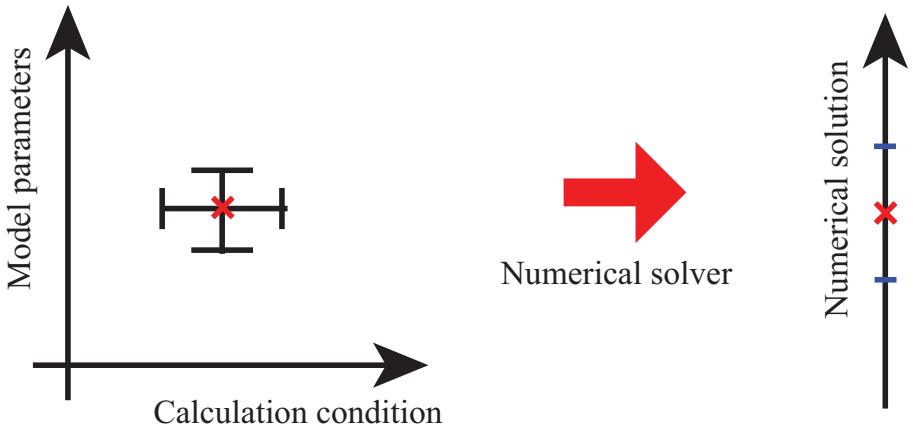

(b) Conceptional diagram of simulation of fluid dynamics with uncertainty in terms of the standard uncertainty range

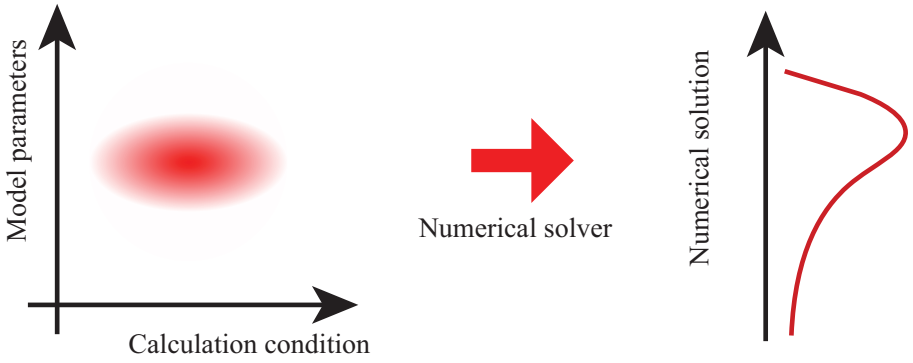

(c) Conceptional diagram of simulation of fluid dynamics with uncertainty in terms of pdf

Fig.1.5: Simulation of fluid dynamics without or with uncertainty

uncertainty.

1.5 Objectives of this research

The comprehensive objective of this study is to develop a framework to quantify the effect of uncertainty inherent in simulation input and to use the quantified characteristics of simulation system to enhance the utility of simulation system for real fluid phenomena.

The research target is representative problems in computational fluid dynamics; shock and interfacial multiphase fluid interaction which is sensitive to uncertainty inevitable in experimental condition, multi-scale wind forecast model where a most critical parameter to refine the multi-scale model should be found, and fluid flow inside a pneumatic throttle where fluid flow with determined direction and the measurement of outlet condition is only possible. The main purpose of the present thesis is to develop a simulation system of fluid dynamics with uncertain simulation inputs and make use of uncertainty transfer characteristic based on polynomial chaos expansion. For this purpose, I clarified characteristics of uncertainty quantification method based on PCE; construct uncertainty quantification system of fluid dynamic simulation with uncertainty of simulation input; established the usage of statistic information with the constructed uncertainty quantification system; and presented a method using quantified statistic characteristic to assimilate the simulation system with experimental data. Each step is briefly presented below.

1.5.1 Clarification of characteristics of uncertainty quantification method

The PCE is an orthogonal decomposition of probability space with polynomials where the statistic characteristics of the random variable appear. The relationship of statistical quantities; mean and variance, with PCE has explained. With the introduction of two approaches; stochastic Galerkin method and stochastic collocation method, formulation of each method with the Burgers equation is precisely represented. From the explicit formulation as a linear matrix system, the problem dimensionality on stochastic Galerkin method is represented and the relative benefit of stochastic collocation method is addressed. The accuracy of each method was also discussed with the numerical test of the

Burgers equation. The result of the different methods was well agreed with the high resolution. Also, in case of the numerical error exists, the numerical simulation result of the Monte Carlo method and the stochastic collocation method converged to the same solution. For the selection of numerical quadrature, convergence ratio of the Gauss-Legendre quadrature and the Clenshaw-Curtis were compared with numerical tests of the numerical quadrature and PCE reconstruction with various functions. With the tests, the benefit of the Clenshaw-Curtis quadrature address by Trefenthen[65] for numerical quadrature problem; similar convergence with Gauss-Legendre quadrature for a complex problem where the nestedness of the Clenshaw-Curtis quadrature benefits, is confirmed for the PCE reconstruction.

1.5.2 Construction of uncertainty quantification system of fluid dynamic simulation with uncertainty of simulation input

An uncertainty quantification system to evaluate shock-interfacial multiphase simulations with density uncertainty of fluid was constructed. With the constructed system, the effect of density uncertainty on the four representative shock-flat interface interaction (SFI) and two representative shock-bubble interaction (SBI) are quantitatively evaluated. The density is modeled as a random variable with the Gaussian distribution and represented as Hermite chaos using PCE, and their effects on the interaction between shock and interfacial multiphase are attained using stochastic collocation method. Interaction structure affected by the density uncertainty is clarified, and transfer of the uncertainty between structure is represented. It is also observed from these numerical experiments that there exist some insensitive regions in the solution domain where the density uncertainty does not significantly affect the numerical solution.

1.5.3 The usage of statistic information from the quantified results for multi scale wind forecast model

In this part, the usage of the uncertainty quantification technique to classify the most significant parameter between predetermined candidate parameters to improve the pre-

diction accuracy of the multiscale wind prediction model is presented.

Wind power is continuously developing with the growing demand for renewable energy. For effective usage of wind power, accurate prediction of the hub-height wind for the target wind farm is demanded. To this end, improvement of wind prediction with a multiscale model[8], where the wind prediction of a local region is conducted with a CFD model with boundary condition reconstructed from the prediction result of a mesoscale wind prediction model. To enhance the accuracy of this multiscale model, more study to classify important modeling parameters has been demanded.

To this end, statistic characteristics of the wind profile parameter on the common boundary between multiscale model and model parameters of the turbulence model are attained with the uncertainty quantification techniques introduced in chapter 2. By comparing the statistic characteristics between these parameters, the most significant parameter was discussed. For further improvement of the multiscale model, refinement of the classified parameter using real observation data is expected.

1.5.4 Development of assimilation-analysis system based on stochastic characteristics

In the last part of this thesis, a PCE based data assimilation method using a surrogate PCE model constructed from the stochastic collocation method was developed. In this method, simulation input and output is represented with the PCE representation, respectively, and the gradients of PCE coefficients of the input and output with respect to the ransom variable is explicitly attained using the surrogate PCE model based on the orthogonal polynomial. With the gradients of the PCE coefficients, the PCE coefficients of the input can be estimated from those of the output, which is available from experimental data. This method has been applied to identify the inlet pressure of a pneumatic throttle system using the experimental measurement of the outlet mass flow rate. The numerical results agree well with the measured inlet pressure regarding the distribution of probability density function, and exhibit a promising estimation within the IQR box range.

1.6 Outline of thesis

The left part of this thesis is constructed with representing order. In chapter 2, the uncertainty analysis method based on PCE is explained, and the characteristics important for developing uncertainty quantification system is discussed. In the following chapters, the effect of uncertainties is quantitatively evaluated on shock - interfacial multiphase fluid interactions. And dominant parameter of multi-scale wind forecast model are classified from the uncertainty quantification result. In chapter 5, usage of the stochastic characteristics is expanded for data assimilation, and a data assimilation - analysis is implemented for calculation condition estimation of a pneumatic throttle. In the final chapter, the achievement of the presented thesis will be summarized, and future works will be presented.

Chapter 2

Polynomial chaos expansion approach to uncertainty quantification

2.1 Elementary theory of PCE

2.1.1 Spectral representation of random space with polynomial chaos

The polynomial chaos concept was introduced by N. Wiener[70] using Gaussian distribution and later expanded for other kind of probability distributions by D. Xiu[77]. With a set of of random variables $\mathbf{\Xi} = \{\xi_i\}_{i=1}^{\infty}$, we can consider a set of polynomial with degree less or equal to p and denote the set $\hat{\Gamma}_p$. Then, the polynomial chaos of order p, Γ_p, is defined as a set of polynomials included in the set of p-th polynomial $\hat{\Gamma}_p$ and orthogonal to the set of $(p-1)$-th polynomial $\hat{\Gamma}_{p-1}$. The space spanned by Γ_p is refered as the p-th homogenous chaos[70] $\tilde{\Gamma}_p$. From the definition

$$\tilde{\Gamma}_p \cap \hat{\Gamma}_{p-1} = \emptyset \tag{2.1}$$

and

$$\hat{\Gamma}_p = \tilde{\Gamma}_p + \hat{\Gamma}_{p-1}, \tag{2.2}$$

or simply using direct sum $\bigoplus$

$$\hat{\Gamma}_p = \tilde{\Gamma}_p \bigoplus \hat{\Gamma}_{p-1}. \tag{2.3}$$

A the second order measure space Ω, where a second order measure is defined, is represented as[29]

$$\Omega = \bigoplus_{i=0}^{\infty} \tilde{\Gamma}_i. \tag{2.4}$$

This implicates we can find unique representation of any elements of the measure space Ω using the concept of the polynomial chaos.

Any random variable $R(\boldsymbol{\xi}) \in \Omega$ is represented as the polynomial chaos form

$$R(\boldsymbol{\xi}) = a_0\Gamma_0 + \sum_{i_1=1}^{\infty} a_{i_1}\Gamma_1(\xi_{i_1}) + \sum_{i_1=1}^{\infty}\sum_{i_2=1}^{i_1} a_{i_1 i_2}\Gamma_2(\xi_{i_1},\xi_{i_2}) + \sum_{i_1=1}^{\infty}\sum_{i_2=1}^{i_1}\sum_{i_3=1}^{i_2} a_{i_1 i_2}\Gamma_3(\xi_{i_1},\xi_{i_2},\xi_{i_3}) + \cdots \tag{2.5}$$

Notice $\Gamma_p(\cdot)$ indicates the p-th polynomial chaos constructed by any combination of input elements. Using a corresponding orthogonal polynomial basis set $\boldsymbol{\Psi} = \{\psi_i\}_{i=0}^{\infty}$ with the series of the polynomial chaos $\boldsymbol{\Gamma} = \{\Gamma_0, \Gamma_1(\xi_{i_1}), \Gamma_2(\xi_{i_1},\xi_{i_2}), \cdots\}$, the equation (2.5) is simply represented as the polynomial chaos expansion (PCE)

$$R(\boldsymbol{\xi}) = \sum_{k=0}^{\infty} a_k \psi_k(\boldsymbol{\xi}). \tag{2.6}$$

Despite the exact expansion should be done with infinity number of polynomial base, the expansion is truncated by PC for real implementation, where the infinite summation could not attained generally, and represented as

$$R(\boldsymbol{\xi}) = \sum_{k=0}^{PC} a_k \psi_k(\boldsymbol{\xi}) + \epsilon(PC). \tag{2.7}$$

$\epsilon(PC)$ denotes truncation error. Despite uncertainty analysis from multiple uncertainties $\boldsymbol{\xi}$ can be developed with PCE, this thesis focus only on one-dimensional analysis in uncertainty dimension and represent the uncertainty with simply ξ without the subscript. Then, equation (2.8) is represented as

$$R(\xi) = \sum_{k=0}^{P} a_k \phi_k(\xi) + \epsilon(P), \tag{2.8}$$

with a orthogonal polynomial basis $\Phi = \{\phi(\xi)\}_{i=1}^{\infty}$.

2.1.2 Evaluation of statistical quantities with polynomial chaos expansion.

One dimensional random variable ξ and a series of certain orthogonal polynomial $\Phi = \{\phi(\xi)\}_{i=1}^{\infty}$. The orthogonal polynomials are defined by the orthogonality of polynomial

$$\langle \phi_i(\xi)\phi_j(\xi)\rangle := \int \phi_i(\xi)\phi_j(\xi)w(\xi)d\xi = \delta_{i,j}\left\langle \phi_i(\xi)^2\right\rangle \tag{2.9}$$

with Kronecker delta

$$\delta_{i,j} = \begin{cases} 1 & \text{if } i = j \\ 0 & \text{if } i \neq j \end{cases} \tag{2.10}$$

with weight function $w(\xi)$.

If we choose the weight function as a probability density function

$$w(\xi) = p(\xi), \tag{2.11}$$

a probability measure is represented as

$$E[\cdot] := \int \cdot p(\xi)d\xi = \int \cdot w(\xi)d\xi = \langle\cdot\rangle\,. \tag{2.12}$$

And the M-th moment of a random variable $R(\xi)$ can simply represented

$$E[R(\xi)^M] = \int R(\xi)^M p(\xi)d\xi = \left\langle R(\xi)^M\right\rangle. \tag{2.13}$$

Especially, the first moment and the second moment is attained as a simple form from the orthogonality.

With PCE of a random variable $R(\xi)$,

$$R(\xi) = \sum_{n=0}^{\infty} \hat{R}_n\phi_n(\xi), \tag{2.14}$$

the first moment, also called as mean value, is

$$E[R(\xi)] = \int \sum_{n=0}^{\infty} \hat{R}_n\phi_n(\xi)\phi_0 p(\xi)d\xi = \int \hat{R}_0\phi_0^2 p(\xi)d\xi = \hat{R}_0 \tag{2.15}$$

with general characteristics of weighted orthogonal polynomial

$$\phi_0 = 1, \tag{2.16}$$

and the orthogonality on equation (2.9). With same procedure, the second moment is attained as

$$E[R(\xi)^2] = \int \sum_{n=0}^{\infty} \hat{R}_n \phi_n(\xi) \sum_{m=0}^{\infty} \hat{R}_m \phi_m(\xi) p(\xi) d\xi = \sum_{n=0}^{\infty} \hat{R}_n^2 \left\langle \phi(\xi)_n^2 \right\rangle . \tag{2.17}$$

The variance is attained by

$$V[R(\xi)] = E[R(\xi)^2] - E[R(\xi)]^2 = \sum_{n=1}^{\infty} \hat{R}_n^2 \left\langle \phi(\xi)_n^2 \right\rangle , \tag{2.18}$$

and standard deviation is square root of the variance. Third or more higher moment could be also attained using polynomial chaos expansion, but the simple representation does not show up. For instance, the third moment is represented as

$$\begin{aligned} E[R(\xi)^3] &= \int \sum_{n=0}^{\infty} \hat{R}_n \phi_n(\xi) \sum_{m=0}^{\infty} \hat{R}_m \phi_m(\xi) \sum_{\ell=0}^{\infty} \hat{R}_\ell \phi_\ell(\xi) p(\xi) d\xi \\ &= \sum_{n=0}^{\infty} \sum_{m=0}^{\infty} \sum_{\ell=0}^{\infty} \hat{R}_n \hat{R}_m \hat{R}_\ell \left\langle \phi(\xi)_n \phi(\xi)_m \phi(\xi)_\ell \right\rangle , \end{aligned} \tag{2.19}$$

but the term $< \phi(\xi)_n \phi(\xi)_m \phi(\xi)_\ell >$ cannot be simplified using the orthogonality.

2.2 Efficient calculation of PCE coefficients

PCE is used to analysis a input-output system with random variables. With a differential equation system

$$L(\boldsymbol{x}, t, \xi; u) = f(\boldsymbol{x}, t, \xi). \tag{2.20}$$

u denotes input and $f(\boldsymbol{x}, t, \xi)$ is source term. Truncated PCE of the input is

$$u(\boldsymbol{x}, t, \xi) = \sum_{n=0}^{P} \hat{u}_n(\boldsymbol{x}, t) \phi_n(\xi). \tag{2.21}$$

There are two approach to resolve this stochastic partial equation based on PCE approach.

2.2.1 Stochastic Galerkin method

The first approach is stochastic Galerkin method. In this method, the differential equation system of PCE coefficients are attained by measuring residual with the polynomial bases

of the governing differential equation system as shown in equation 2.22.

$$\langle L(\boldsymbol{x}, t, \xi; u)\phi_n(\xi)\rangle = \langle f(\boldsymbol{x}, t, \xi)\phi_n(\xi)\rangle \tag{2.22}$$

This formula yields deterministic equation system, which does not depend on the random variable ξ. The formulation of stochastic Galerkin method will be explained precisely in section 2.2.3.

2.2.2 Stochastic collocation method

In stochastic collocation method[74], solutions of a corresponding deterministic system are used to obtain the numerical approximation of the stochastic solution. The deterministic simulations are carried out with different values of the stochastic parameters of interest.

The numerical approximation to the solution of the stochastic system is realized by a discrete projection truncated by P-th polynomial,

$$d(\xi) = \sum_{k=0}^{P} \hat{d}_k \phi_k(\xi), \tag{2.23}$$

where the coefficients are calculated from the numerical quadrature with corresponding deterministic solutions $\tilde{q}(\xi^{(i)})$ as follows

$$\hat{d}_k = \frac{1}{\gamma_k} \sum_{i=1}^{P} \tilde{q}(\xi^{(i)})\phi_k(\xi^{(i)})p(\xi^{(i)})w^{(i)} \tag{2.24}$$

where $\xi^{(i)}$ means each quadrature point and $w^{(i)}$ the corresponding quadrature weight.

M is the number of the quadrature points and

$$\gamma_k = \int \phi_k(\xi)^2 p(\xi) \mathrm{d}\xi. \tag{2.25}$$

With proper quadrature rule, the discrete projection $d(\xi)$ converge to the solution $q(\xi)$ of the stochastic system with an error bound less than the summation of truncate error and the aliasing error[74] of the collocation method. Aforementioned, as we assumed a Gaussian distributed uncertainty, the Gauss-Hermite quadrature is used in this work.

2.2.3 Formulation of PCE methods with the Burgers equation.

Calculation cost of stochastic Galerkin method, stochastic collocation method, and Monte carlo method is numerically compared using the Burgers equation with uncertainty in viscosity $v(\xi)$

$$\frac{\partial u(x,t,\xi)}{\partial t} + u(x,t,\xi)\frac{\partial u(x,t,\xi)}{\partial x} = \nu(\xi)\frac{\partial^2 u(x,t,\xi)}{\partial x^2}, \tag{2.26}$$

where $u(x,t,\xi)$ denotes velocity of position x at time t. With PCE of the viscosity

$$\nu(\xi) = \sum_{n=0}^{PC} \hat{\nu}_n \phi_n(\xi) \tag{2.27}$$

and PCE of the velocity

$$u(x,t,\xi) = \sum_{n=0}^{PC} \hat{u}_n(x,t)\phi_n(\xi). \tag{2.28}$$

Stochastic Galerkin Method

Substituting equation (2.26),

$$\sum_{n=0}^{PC}\left(\phi_n \frac{\partial \hat{u}_n}{\partial t}\right) + \sum_{n=0}^{PC}\left(\sum_{m=0}^{PC}\phi_n\phi_m\hat{u}_m\frac{\partial \hat{u}_n}{\partial x}\right) = \sum_{n=0}^{PC}\left(\sum_{m=0}^{PC}\hat{\nu}_m\phi_n\phi_m\frac{\partial^2\hat{u}_n}{\partial x^2}\right). \tag{2.29}$$

The Galerkin formulation, (2.22) with ϕ_ℓ, is represented as

$$\sum_{n=0}^{PC} h_{n\ell}\frac{\partial \hat{u}_\ell}{\partial t} + \sum_{n=0}^{PC}\left(\sum_{m=0}^{PC} c_{nm\ell}\hat{u}_m\frac{\partial \hat{u}_n}{\partial x}\right) = \sum_{n=0}^{PC}\left(\sum_{m=0}^{PC}\hat{\nu}_m c_{nm\ell}\frac{\partial^2\hat{u}_n}{\partial x^2}\right). \tag{2.30}$$

In here,

$$h_{ij} = \langle \phi_i\phi_j \rangle \tag{2.31}$$

and

$$c_{ijk} = \langle \phi_i\phi_j\phi_k \rangle . \tag{2.32}$$

With finite volume representation with finite volume

$$\Omega := \left[x_k - \frac{\Delta x}{2} : x_k + \frac{\Delta x}{2}\right], \tag{2.33}$$

equation (2.30) is represented as

$$\sum_{n=0}^{PC} h_{n\ell}\frac{\partial}{\partial t}\int_\Omega \hat{u}_n dx + \sum_{n=0}^{PC}\left(\sum_{m=0}^{PC} c_{nm\ell}\int_\Omega \hat{u}_m\frac{\partial \hat{u}_n}{\partial x}dx\right) = \sum_{n=0}^{PC}\left(\sum_{m=0}^{PC}\hat{\nu}_m c_{nm\ell}\int_\Omega \frac{\partial^2\hat{u}_n}{\partial x^2}dx\right). \tag{2.34}$$

Using the volume represent value of the PCE coefficients with discrete time $T+s := t+s\Delta t$,

$$\bar{u}_n[k,T+s] := \frac{\int_\Omega \hat{u}_n(x,t+s\Delta t)dx}{\Delta x} \tag{2.35}$$

and

$$\bar{\nu}_n[k,T+s] := \frac{\int_\Omega \hat{\nu}_n(x,t+s\Delta t)dx}{\Delta x}, \tag{2.36}$$

each term of equation (2.34) is discretized as

$$\frac{\partial}{\partial t}\int_\Omega \hat{u}_n dx = \frac{\Delta x}{\Delta t}(\bar{u}_n[k,T+1]-\bar{u}_n[k,T]), \tag{2.37}$$

$$\begin{aligned}\int_\Omega \hat{u}_m\frac{\partial\hat{u}_n}{\partial x}dx = {}& \bar{u}_m[k,T+1]\left(\bar{u}_m[k,T]-\bar{u}_m[k-1,T]\right)\left(\frac{\bar{u}_n[k,T]+|\bar{u}_n[k,T]|}{2|\bar{u}_n[k,T]|}\right)\\ &+\bar{u}_m[k,T+1]\left(\bar{u}_m[k+1,T]-\bar{u}_m[k,T]\right)\left(\frac{\bar{u}_n[k,T]-|\bar{u}_n[k,T]|}{2|\bar{u}_n[k,T]|}\right),\end{aligned} \tag{2.38}$$

and

$$\int_\Omega \frac{\partial^2\hat{u}_n}{\partial x^2}dx = \frac{1}{\Delta x}\left(\bar{u}_n[k+1,T+1]-2\bar{u}_n[k,T+1]+\bar{u}_n[k-1,T+1]\right). \tag{2.39}$$

With these discretization, equation (2.34) is attained as follow

$$\sum_{n=0}^{PC}\left(P_{n\ell k}\bar{u}_n[k-1,T+1]+Q_{n\ell k}\bar{u}_n[k,T+1]+R_{n\ell k}\bar{u}_n[k+1,T+1]\right)=\bar{u}_\ell[k,T] \tag{2.40}$$

with

$$P_{n,\ell,k} = \sum_{m=0}^{PC} c_{nm\ell}\left(-\bar{u}_m[k,T]\left(\frac{\bar{u}_n[k,T]+|\bar{u}_n[k,T]|}{2|\bar{u}_n[k,T]|}\right)-\frac{\bar{\nu}_m}{\Delta x}\right)\frac{\Delta t}{h_{\ell\ell}\Delta x}, \tag{2.41}$$

$$Q_{n,\ell,k} = \left(h_{n\ell}\frac{\Delta x}{\Delta t}+\sum_{m=0}^{PC} c_{nm\ell}\left(\bar{u}_m[k,T]\frac{\bar{u}_n[k,T]}{|\bar{u}_n[k,T]|}+\frac{2\bar{\nu}_m}{\Delta x}\right)\right)\frac{\Delta t}{h_{\ell\ell}\Delta x}, \tag{2.42}$$

and

$$R_{n,\ell,k} = \sum_{m=0}^{PC} c_{nm\ell}\left(\bar{u}_m[k,T]\left(\frac{\bar{u}_n[k,T]-|\bar{u}_n[k,T]|}{2|\bar{u}_n[k,T]|}\right)-\frac{\bar{\nu}_m}{\Delta x}\right)\frac{\Delta t}{h_{\ell\ell}\Delta x}. \tag{2.43}$$

Let's introduce a vector with $N \times (PC+1)$ elements; N denoting number of finite volumes,

$$\boldsymbol{U}[T] = \begin{bmatrix} \boldsymbol{u}_1[T] & \boldsymbol{u}_2[T] & \boldsymbol{u}_3[T] & \cdots & \boldsymbol{u}_{PC}[T] \end{bmatrix}^T, \tag{2.44}$$

with

$$\boldsymbol{u}_i[T] = \begin{bmatrix} u_i[1,T] & u_i[2,T] & \cdots & u_i[N,T] \end{bmatrix} \quad (i = 1, 2, \cdots, PC), \tag{2.45}$$

for matrix formulation of the discretized equation of PCE coefficient, equation (2.40).

Then, with $N \times N$ matrix

$$A_{i,j} = \begin{bmatrix} \delta_{i,j} & 0 & 0 & \cdots & 0 & 0 \\ P_{i,j,2} & Q_{i,j,2} & R_{i,j,2} & \cdots & 0 & 0 \\ 0 & P_{i,j,3} & Q_{i,j,3} & \cdots & 0 & 0 \\ 0 & 0 & P_{i,j,4} & \cdots & 0 & 0 \\ \vdots & \vdots & \vdots & \ddots & \vdots & \vdots \\ 0 & 0 & 0 & \cdots & Q_{i,j,M-1} & R_{i,j,N-1} \\ 0 & 0 & 0 & \cdots & 0 & \delta_{i,j} \end{bmatrix}, \tag{2.46}$$

a $(PC \times M) \times (PC \times M)$ size matrix is attained

$$\mathcal{A} = \begin{bmatrix} A_{0,0} & A_{1,0} & A_{2,0} & \cdots & A_{PC,0} \\ A_{0,1} & A_{1,1} & A_{2,1} & \cdots & A_{PC,1} \\ A_{0,2} & A_{1,2} & A_{2,2} & \cdots & A_{PC,2} \\ \vdots & \vdots & \vdots & \ddots & \vdots \\ A_{0,PC} & A_{1,PC} & A_{2,PC} & \cdots & A_{PC,PC} \end{bmatrix} \tag{2.47}$$

for a matrix formulation of equation (2.40),

$$\mathcal{A}\boldsymbol{U}[T+1] = \boldsymbol{U}[T]. \tag{2.48}$$

The solution of this matrix system of PCE coefficients is attained from a linear solver.

In case of $i = j = 0$, the matrix $A_{0,0}$ is correspond with a numerical simulation system with a deterministic system and the solution of matrix $\mathcal{A}$ is corresponding solving a $PC \times PC$ numerical simulation system at the same time. The size of system increased with square of PC.

stochastic collocation method

With stochastic collocation method, as shown in equation (2.24), independent PC times numerical simulation is needed. Using the symbols forward section, the equation system

$$A_{0,0}\boldsymbol{u}[T+1] = \boldsymbol{u}[T] \tag{2.49}$$

is solved for quadrature points $\{u^{(i)}[T]\}_{i=1}^{PC}$, independently. Increase of the calculation dimension with introduce of the statistical characteristic is comparatively low for stochastic collocation method, and the independent calculation makes stochastic collocation method adequate for parallel computation. From these benefits, stochastic collocation is used in this thesis.

2.2.4 Accuracy of the PCE methods with the Burgers equation

To confirm the accuracy of the PCE methods, numerical test and comparison of the attained test result were conducted. The solution of the stochastic Burgers' equation with uncertainty on the left boundary condition was solved by the Latin hypercube Monte Carlo simulation (MC), stochastic collocation method (SC), and stochastic Galerkin method (SG), separately. Boundary condition was left high scaled with 1 and right low scaled with -1 and uniform uncertainty of distributes in 5% range introduced at the left boundary amplitude. For the stochastic collocation method and the stochastic Galerkin method, the Legendre chaos was used, and the Clenshaw Curtis quadrature, discussed in the following section, was used in the stochastic collocation method. The variance of the velocity u was compared between cases.

First, convergence of the Montecarlo method is shown in Figure 2.1(a). The number of mesh N used for the simulation was 2048. The convergence of the variance with increase of the number of trial is represented. The convergence of the other two method based on PCE were hard to figure out with graph, because the convergency were fast and the differences could not be noticed. The high resolution solution attained by the three method figured in frame (b) of same figure. The result of high resolution well agreed between cases, and I selected the high resolution result attained by SC as reference value and showed difference with each test cases on Table 2.1, 2.2, and 2.3. Aforementioned fast convergence of the

stochastic collocation method and the stochastic Galerkin method could be check from the table.

The effect of the numerical error on the uncertainty quantification method was studied using the change of the number of element N in distance direction. With large number of element the numerical error became small, but the numerical error remain significant with small number of element. The change of the solution attained by number of element is represented in figure 2.2. Each solution attained by different method changed with the number of element, but the change tendency was same. This tendency also can be check from Table 2.1, 2.2, and 2.3. Notably, the difference of MC with 2560 trail and SC with 8th order polynomial were same, which means the quantified result is unique, despite the value is different with the reference value due to the effect of the numerical error. Thus, we can conclude that the effect of the numerical error affects the uncertainty quantification result, but there exist unique result with high resolution uncertainty quantification method in case of existence numerical error does not change. Moreover, with high precision numerical method which the effect of numerical error is comparatively small, we can attain a reliable uncertainty quantification result.

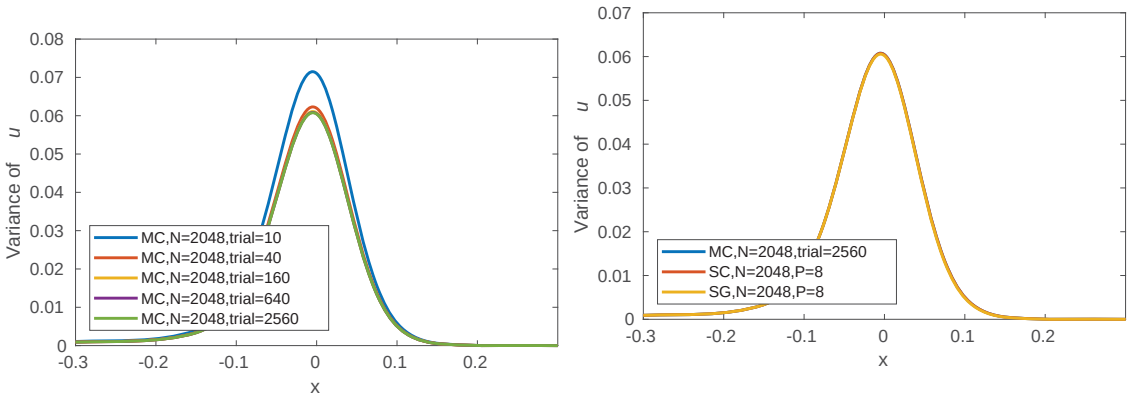

(a) Convergence of MC

(b) Agreement of solution attained by 3 method

Fig.2.1: Convergence of Monte Carlo method and high resolution solution of three method

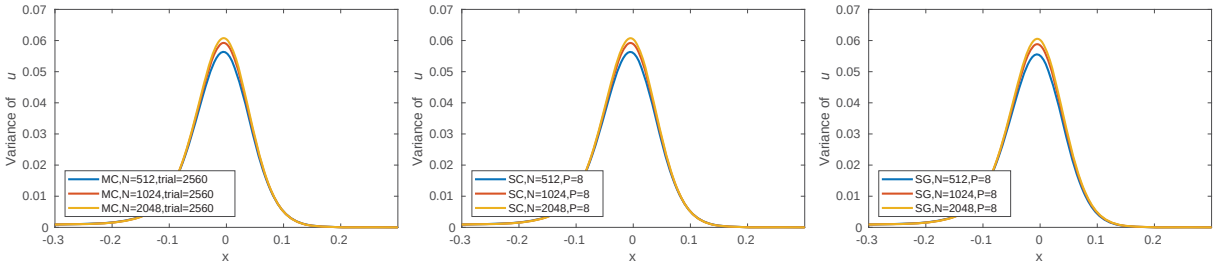

(a) MC (b) SC (c) SG

Fig.2.2: Effect of the numerical error on three method

Table 2.1: Accuracy test result of the latin hypercube Montecarlo simulation

Number of trial	$N = 512$	$N = 1024$	$N = 2048$
10	3.77×10^{-4}	8.63×10^{-4}	7.29×10^{-4}
20	6.53×10^{-5}	8.28×10^{-5}	1.25×10^{-4}
40	-7.98×10^{-5}	4.15×10^{-5}	1.05×10^{-4}
80	-1.37×10^{-4}	-2.54×10^{-5}	5.89×10^{-5}
160	-1.61×10^{-4}	-4.82×10^{-5}	2.17×10^{-5}
320	-1.81×10^{-4}	-5.22×10^{-5}	1.35×10^{-5}
640	-1.85×10^{-4}	-5.99×10^{-5}	6.42×10^{-6}
1280	-1.89×10^{-4}	-6.34×10^{-5}	2.85×10^{-6}
2560	-1.91×10^{-4}	-6.48×10^{-5}	1.56×10^{-6}

Table 2.2: Accuracy test result of the stochastic collocation method

Degree of polynomial	$N = 512$	$N = 1024$	$N = 2048$
2	-1.92×10^{-4}	-6.65×10^{-5}	-2.75×10^{-7}
3	-1.92×10^{-4}	-6.63×10^{-5}	-6.8×10^{-9}
4	-1.92×10^{-4}	-6.62×10^{-5}	-2.65×10^{-11}
5	-1.92×10^{-4}	-6.62×10^{-5}	-2.74×10^{-10}
6	-1.92×10^{-4}	-6.62×10^{-5}	-3.5×10^{-10}
7	-1.92×10^{-4}	-6.62×10^{-5}	-4.3×10^{-11}
8	-1.92×10^{-4}	-6.62×10^{-5}	0

Table 2.3: Accuracy test result of the stochastic galerkin method

Degree of polynomial	$N = 512$	$N = 1024$	$N = 2048$
2	-2.74×10^{-4}	-1.07×10^{-4}	-2.07×10^{-5}
4	-2.74×10^{-4}	-1.08×10^{-4}	-2.08×10^{-5}
6	-2.74×10^{-4}	-1.08×10^{-4}	-2.08×10^{-5}
8	-2.74×10^{-4}	-1.08×10^{-4}	-2.08×10^{-5}

2.3 Representation of PCE

The orthogonal polynomials are determined from orthogonality of the polynomial, equation (2.9), with weight function $w(\xi)$. Generation rule of the orthogonal polynomials are represented as various form. A differential form of generation rule of orthogonal polynomial is called as the generalized Rodrigues' formula

$$\phi_n(\xi) = \frac{1}{c_n w(\xi)} \frac{d^n}{dx^n} w(\xi) s(\xi)^n, \tag{2.50}$$

where $s(\xi)$ is a polynomial of ξ independent with n and c_n is coefficient only dependent with n[1]. A series of orthogonal polynomial with arbitrary weight function could be attained and the series is not unique due to the selection of c_n and $s(\xi)$, but some well known orthogonal polynomials are usually used.

For instance, with

$$c_n = (-1)^n, \tag{2.51}$$

$$s(\xi) = 1, \tag{2.52}$$

with

$$w(\xi) = \frac{1}{\sqrt{2\pi}} e^{-\frac{\xi^2}{2}} \tag{2.53}$$

yields the Hermite polynomial

$$H_n(\xi) = \frac{(-1)^n}{e^{-\frac{\xi^2}{2}}} \frac{d^n}{d\xi^n} e^{-\frac{\xi^2}{2}}. \tag{2.54}$$

With

$$c_n = 2^n n!, \tag{2.55}$$

$$s(\xi) = \xi^2 - 1 \tag{2.56}$$

with

$$w(\xi) = \frac{1}{2} \tag{2.57}$$

yields the Legendre polynomial

$$P_n(\xi) = \frac{1}{2^n n!}\frac{d^n}{dx^n}(\xi^2 - 1)^n. \tag{2.58}$$

2.3.1 Representation of well know probability density function with gPCE.

With usage of orthogonal polynomials to analysis stochastic phenomena, a strong relationship between orthogonal polynomials and probability distribution. R. G. Ghanem & P. D. Spanos developed Hermite-Chaos expansion for Gaussian distribution, and H Ogura developed Charlier-Chaos expansion Poisson distribution. D. Xiu[76] extended these concept to Askey-scheme of polynomials[3] and make relationship between the polynomials and probability distribution. In this approach, for polynomials of Askey-scheme, probability distributions use the weight of orthogonality as the probability density function is clarified as Table 2.4. And the PCE expanded by these polynomials of Askey-scheme has named as gPCE. In this thesis, I will use PCE to denote gPCE also for convenience.

Polynomials	Weight function	Probability distribution
Hermite polynomial $H_n(x)$	$\frac{1}{\sqrt{2\pi}}e^{-\frac{x^2}{2}}$	Gauss distribution
Laguerre polynomial $L_n^{(\alpha)}(x)$	$\frac{x^\alpha e^{-x}}{\Gamma(\alpha+1)}$	Gamma distribution
Jacobi polynomial $P_n^{(\alpha,\beta)}$	$\frac{\Gamma(\alpha+\beta+2)}{2^{\alpha+\beta+1}\Gamma(\alpha+1)\Gamma(\beta+1)}$	Beta distribution

Table 2.4: Polynomial and corresponding probability distribution

2.3.2 Convergency of Clenshaw curtis quadrature with Legendre polynomials.

With stochastic collocation approach, numerical quadrature is used to represent characteristics of a random variable in probability space. Because the accuracy of the representation of stochastic characteristics of a random variable determines the accuracy of

the collocation method, the convergence of representation is an important problem. In the case of the probability distribution is well know distribution introduced in the former subsection, the Gauss quadrature of a determined probability distribution; e.g. Gauss-Legendre quadrature for uniform distribution and Gauss-Hermite quadrature for Gauss distribution. But, in case of the probability distribution is not the aforementioned distribution, the selection of numerical quadrature is essential. To this end, the convergence of two numerical quadrature; the Gauss Legendre quadrature and the Clenshaw-Curtis quadrature. The Clenshaw-Curtis was chosen, because it has nestedness of quadrature point, whereas Gauss quadrature does not, and the almost same convergence ratio for approximation problem of complex functions[65].

Comparison of two quadrature rules is conducted in two way. The first one is simple numerical quadrature and the second one is reconstruction accuracy of PCE from stochastic collocation. The results are presented in figure 2.3 and 2.4. The evaluated function is represented in the caption of each figure. The left side is the result of simple numerical quadrature, and the right side is the result of PCE reconstruction. The error of simple numerical quadrature test was evaluated absolution value of true or high precision calculation value, and that of PCE reconstruction with Legendre polynomial was evaluated from the second norm of difference.

In the figure 2.3 (a-c), high convergence of Gauss-Legendre quadrature appeared. The Gauss-Legendre quadrature has two times convergence ratio compared with the Clenshaw-Curtis quadrature, which also confirmed from convergence analysis. But with more hard to approximate functions in figure 2.3 (d) and 2.3 (a-d), the convergence ratio of two quadrature with simple quadrature test show no difference as reported by Trefethen[65]. On figure 2.3(c-d), convergence ratio of PCE reconstruction also does not different. From these figures, the fact that difference of the convergence ratio achieved with simple cases quadrature converges with sufficient accuracy with a small number of quadrature point. But for the functions with late convergence which need to be evaluated with a large number of evaluation point for accuracy, convergence ratio between two quadrature shows no difference. And in case of a large number of evaluation is needed, the nestedness of the Clenshaw-Curtis quadrature benefit by halving evaluation point to improve accuracy as Trefethen found in simple numerical quadrature[65]. From these details, the Clenshaw-

Curtis quadrature was choosed for the last part, chapter 4 and 5, of this thesis.

2.4 Summary

In this chapter, the definition of PCE and implementation method has been precisely explained. Also, the choice of stochastic collocation method as coefficient calculation method for PCE in this thesis is explained from the formulation of the Burgers equation and comparison with the formulation from the stochastic Galerkin method. The accuracy of each method was also discussed with the numerical test of the Burgers equation. The result of the different methods was well agreed with the high resolution. Also, in case of the numerical error exists, the numerical simulation result of the Monte Carlo method and the stochastic collocation method converged to the same solution. Moreover, the merit of the Clenshaw-Curtis method used for the latter part of this thesis is explained from a quadrature test and PCE reconstruction test. For the last part of the thesis, PCE methodologies explained this chapter would be used.

.

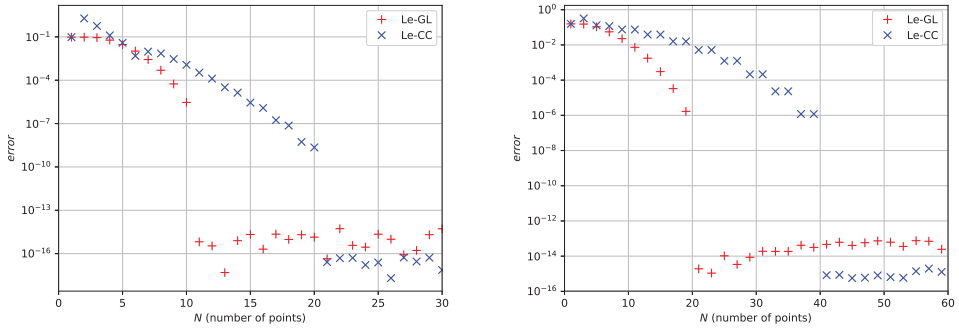

(a) x^{20}

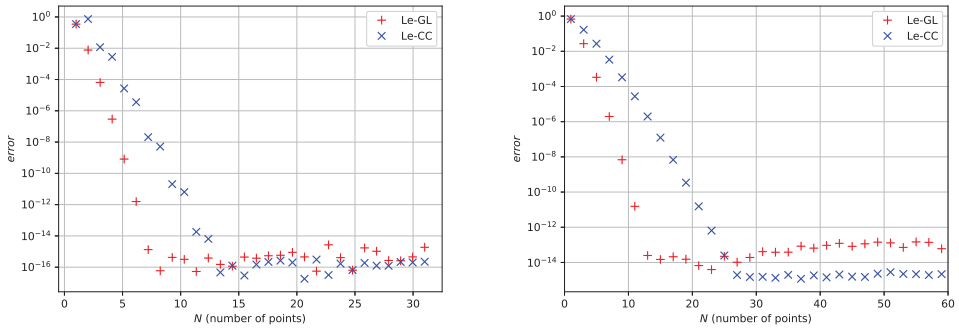

(b) e^{x}

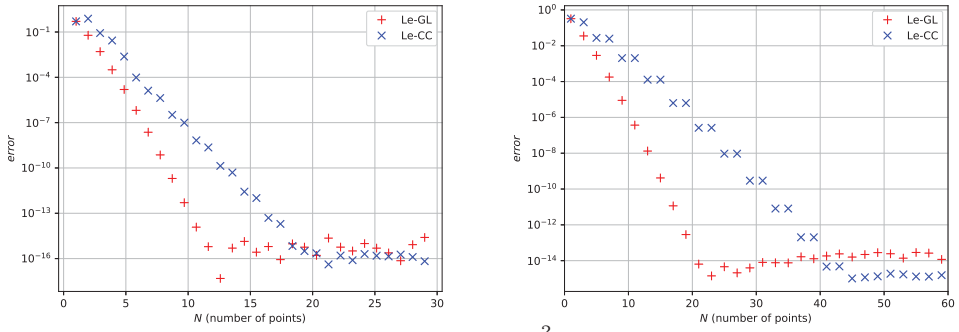

(c) e^{-x^2}

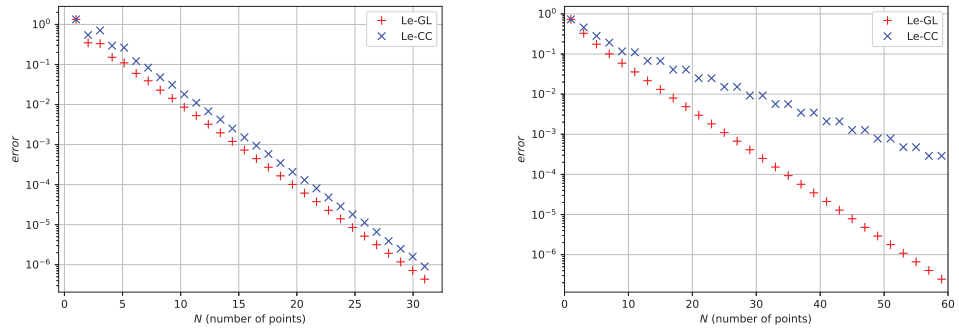

(d) $1/(1+16x^2)$

Fig.2.3: Convergence test of Gauss-Legendre quadrature and Clenshaw - Curtis quadrature

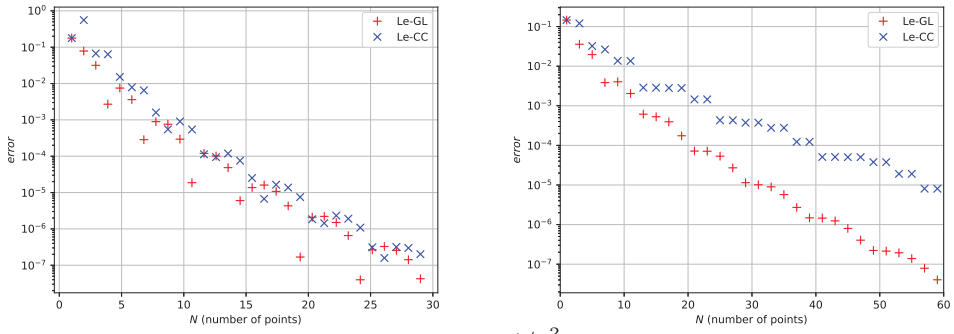

(a) e^{-1/x^2}

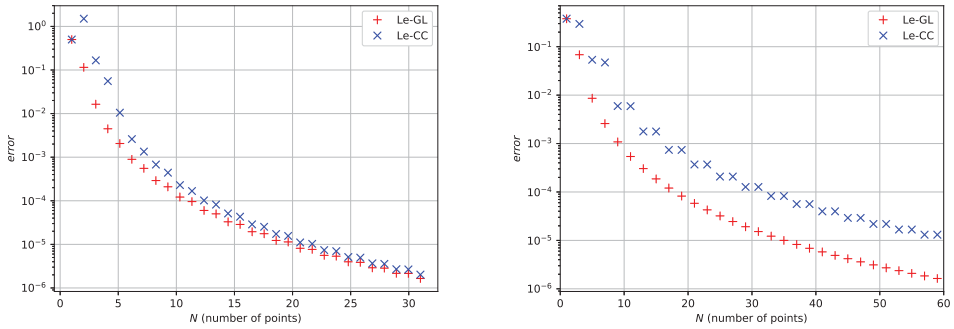

(b) $|x|^3$

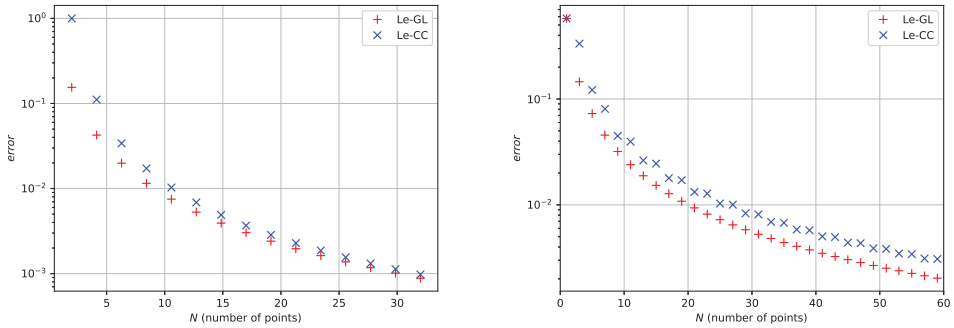

(c) $|x|$

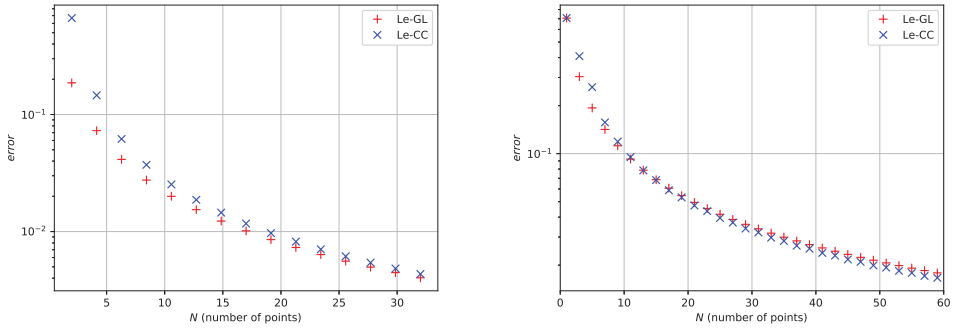

(d) $\sqrt{|x|}$

Fig.2.4: Same as figure 2.3.

Chapter 3

Uncertianty quantification for interaction between shock and interfacial multiphase fluid

3.1 interaction between shock and interfacial multiphase fluid and existence of uncertainty

In this chapter, uncertainty quantification result for interaction between shock and interfacial multiphase fluid is represented. The contents of this chapter are reported as reviewed paper [20] and conference presentation [22,23]. Although the existence of uncertainty in density for interaction between shock and interfacial multiphase fluid is acknowledged [16,18], the effect of the density uncertainty on interaction structures shock - interfacial multiphase interaction has remained unclear. In this study, the effect of the density uncertainty with shock-flat surface interaction and shock-bubble interaction is quantitatively evaluated using stochastic collocation method.

The interaction between shock and interfacial multiphase fluid is a fundamental and important phenomenon of compressible multiphase flow problems. When a shock wave incidents on the interface of a multiphase substance, the velocity relationship with the

shock wave propagating across the interface result in a complex reflection and refraction structure depending on the incident angle of the shock. Various studies have been done related to the reflection-refraction structure of the shock wave and its transition.

The interaction between the shock wave and the interface is divided into regular reflection and irregular reflection depending on the shape of the structure formed by the interaction. The transition of the two structures is theoretically proposed for the maximum reflection angle condition (the detachment criterion) which is possible for regular reflection, and the minimum reflection angle condition (the mechanical equilibrium criterion) which is theoretically possible for irregular reflection. However, there is a dual solution domain in which both integrated structures exist between these two criteria. Kudryavtsev et al.[26] suggested that the stability of each structure is important in the transition between regular reflection and irregular reflection in the dual domain. Sudani et al.[59] confirmed that the stability of the structure is important by transitioning the reflecting structure using water vapor in a wind tunnel experiment. Thus, it was proved that the stability of the shockwave structure is important in its transition.

The shock-bubble interaction (SBI) is a fundamental phenomenon in compressible multiphase flow. In the SBI process, the shock is refracted and reflected when it passes through the bubble which has material properties different from the ambient fluid, thereby interfering with the phase interfaces as well as other flow structures such as density inhomogeneity and turbulence. As such, the SBI involves complicated physics including the interactions among shocks and flows with inhomogeneous density, which enriches the flow structures with various waves and fronts.

SBI has been studied as an essential example for investigating more general shock-accelerated inhomogeneous flows[79] that have a broad application in various fields[46]. Hass and Sturtevant conducted experiments on SBI and measured the velocity of each shock quantitatively[16]. After Picone and Boris simulated the vorticity generation in SBI with two-dimensional numerical analysis[44], numerical simulation has been increasingly used as a powerful approach to investigate SBI. With the development of computational fluid dynamics on the compressible fluid, the numerical reproduction of SBI has been carried out by many researchers with different methods, such as[7,9,25,31,36,43,45,53,55] among many others. As illustrated in[45], the velocities of shocks and material interfaces can be quan-

titatively evaluated from numerical analysis, which rewards numerical simulation a big advantage over experimental measurement.

Another important and challenging issue in the experimental studies of SBI is that uncertainties are always involved in the experimental procedure. Hass and Sturtevant mentioned the existence of the variability from run to run in their measurement results due to contamination of the bubble and uncertainty in the strength of the incident shock[16]. Layes et al. also mentioned the variation in observational results due to some uncertainties in their experiments[28]. A few works have been so far reported on numerical analysis of uncertainties in SBI. Shankar et al. carried out numerical simulations and concluded that the density change in bubble remarkably affects SBI[51]. In[56], So used polynomial chaos to quantify the effects of bubble density on the flow structures generated in the interference process of SBI. Nevertheless, in spite of the great potential of numerical analysis in investigating the uncertainty effects on SBI, the relevant reports in the literature are very limited, and more exploration is demanded.

The purpose of this study is to obtain knowledge of the interaction between shock and interfacial multiphase fluid by evaluating the influence of impurities around the transition area of the interaction between shock and interfacial multiphase fluid using the uncertainty quantification based stochastic collocation method. We present comprehensive numerical study on the interaction between shock and interfacial multiphase fluid with uncertainties in density. An in-house high-resolution numerical model for compressible multiphase flow including moving interfaces was used to simulate representative shock-flat interface interaction (SFI) and the SBI processes. Deterministic computations with variation in density were carried out to produce a set of numerical results for implementing the non-intrusive stochastic collocation method. The statistics of various physical fields were then used to quantify the effects of the uncertainty in density on interaction structures.

3.1.1 Flow structure in SFI

The work of Henderson et al.[18] is prominent in the field of interaction structure at the interface of multiphase materials. They classified the structure of the interaction between shock and interfacial multiphase fluid at the interface of multiphase materials and clarified

that there is a transition between each structure according to the incident angle. In this work, as shown in Fig. 3.1, the interaction structure of shock wave/interface was classified into Regular refraction and Irregular refraction based on whether the refraction phenomenon of a shock wave at the interface obeys the general law of refraction. In the case of a weak shock wave (Weak shock[4]), since the shock wave refracted at the interface either becomes an expansion fan or maintains a shock wave structure, the regular refraction was classified into RRE and RRR. On the other hand, irregular refraction was classified into BPR and FPR according to the positional relationship between precursor and shock wave generated by the difference in impedance between two media. Irregular refraction was further classified into another case where Mach reflection is formed at the interface as FNR. The detailed study of each structure will be discussed in the Results and Discussions section with the results of numerical simulations.

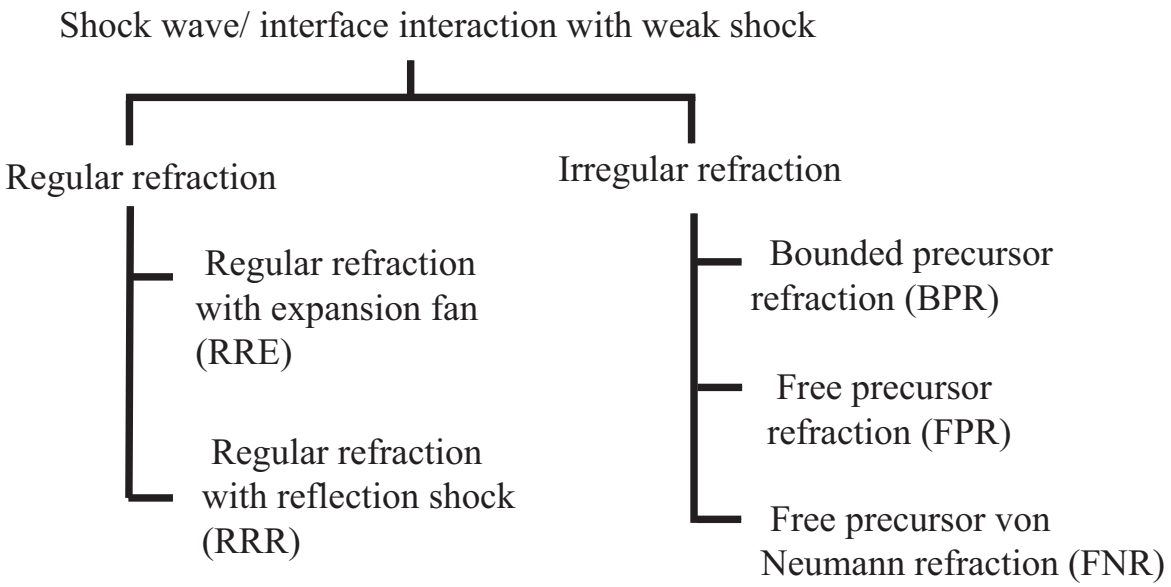

Fig.3.1: Various shock-interface interaction structures with weak shock.

3.1.2 Flow structure in SBI

In this thesis, we focus on the interference of shocks and bubble fronts in the planar SBI which has been extensively described in many studies[16,18,28,45,46].

In SBI, a complex unsteady phenomenon occurs due to a difference in acoustic charac-

teristics between the inner side and the outer side of the deformed curved surface interface. Not all unsteady phenomena and acoustic characteristics can be expressed, but Atwood number

$$A = \frac{\rho_{\mathrm{b}} - \rho_{\mathrm{air}}}{\rho_{\mathrm{b}} + \rho_{\mathrm{air}}} \tag{3.1}$$

is used as a general way of interpreting SBI for its representativity, where ρ_{b} and ρ_{air} represent density of the bubble and the ambient gas (air), respectively. In the sense of the Atwood number, two typical conditions; the light bubble case where the Atwood number is negative and the heavy bubble case where the Atwood number is positive, are possible.

The main acoustic characteristic determines the flow structures of SBI is acoustic impedance. If the acoustic impedance inside bubble is larger than the ambient fluid

$$\frac{\rho_{\mathrm{b}} c_{\mathrm{b}}}{\rho_{\mathrm{air}} c_{\mathrm{air}}} < 1 \tag{3.2}$$

where c_{b} and c_{air} are the acoustic speed of inside and outside of the bubble, respectively, the bubble works as a diverging lens to the incident shock wave. While if the acoustic impedance inside bubble is larger than the ambient fluid

$$\frac{\rho_{\mathrm{b}} c_{\mathrm{b}}}{\rho_{\mathrm{air}} c_{\mathrm{air}}} > 1, \tag{3.3}$$

the bubble acts as a converging lens to the shock.

Although there exists some condition that the Atwood number cannot express the acoustic characteristic in multiphase flow, e.g. $\rho_{\mathrm{b}} c_{\mathrm{b}} / \rho_{\mathrm{air}} c_{\mathrm{air}} > 1$ with $A < 0$ and vice versa, the diverging case will be referred as light bubble case, and the converging case will be referred as the heavy bubble case in this thesis for its representativity in case of fixed heat ratio γ.

Figure 3.2 shows schematic diagrams of the major structures of our interest for the diverging case at different evolution stages. Since the phenomenon is symmetric in vertical direction, we only show the upper half with the dot-dashed line representing the symmetric axis.

A shock propagates from the right and impacts a 2D cylindrical light bubble and generates consequently the interferences among the flow structures of different fluids. The semicircle of the dotted line in the early stage indicates the initial shape of the bubble

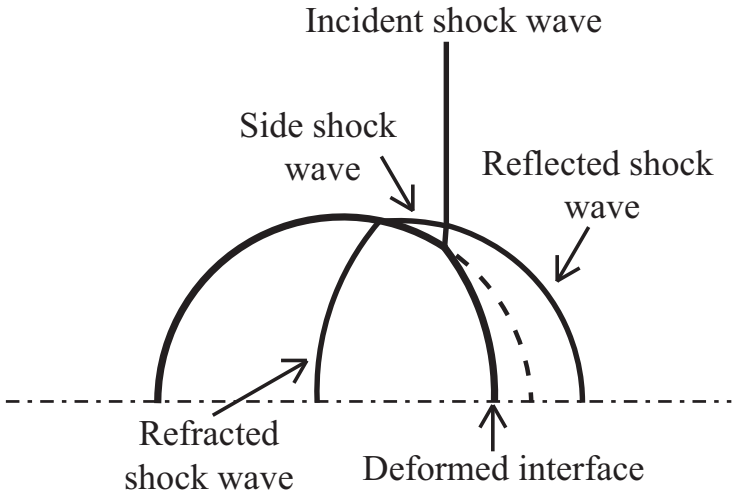

(a) Early stage of SBI.

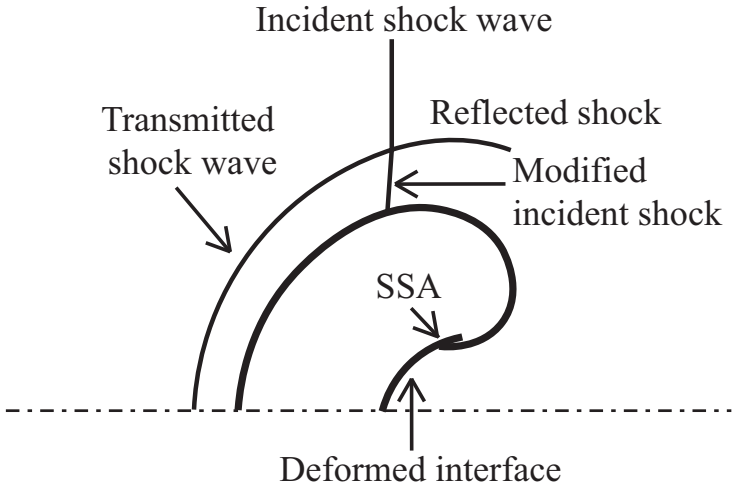

(b) Middle stage of SBI.

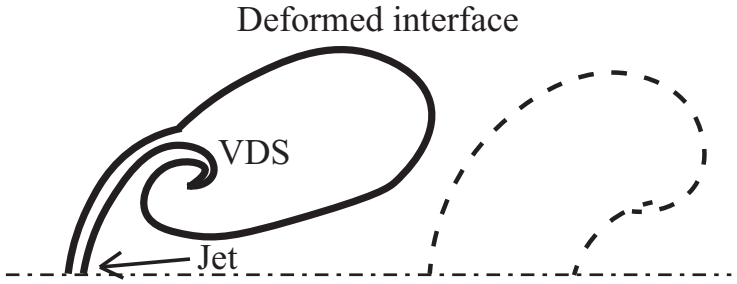

(c) Later stage of SBI.

Fig.3.2: The major flow structures at different stages of SBI process of diverging case. SSA stands for the strong shear area, and VDS for vortex dominant structure

surface, which is deformed and moves left due to the impact of the shock as shown in Fig. 3.2 (a). As a result of the interaction between the incident shock and the bubble surface, a reflected shock is generated and propagates backward outside the bubble, and a refracted shock is generated within the bubble. The refracted shock propagates faster than the original incident shock and forms a diverging curve. As the refracted shock propagates, a side shock connecting the refracted shock and the reflected shock develops as a result of the interaction between shocks and the material front. Eventually, the upstream side bubble surface deforms into a concave shape in the direction away from the struck surface. Henderson et al. categorized this interaction structure into the *regular and irregular* refraction transient with the angle between incident shock and fronts[18]. Hass and Sturtevant referred to this interaction structure as the *twin regular reflection-refraction*[16,18] where four shocks, i.e. incident shock, reflected shock, side shock, and modified incident shock, meet at a quadruple point as shown in frames (a) and (b) of Fig. 1. We will follow this terminology in the rest of this thesis.

Later on, as shown in frame (b), the refracted shock traveling inside the bubble reaches the opposite surface where it interacts with the bubble surface and generates refracted/reflected shocks again. In this thesis, we call this re-refracted shock as the transmitted shock to distinguish it from the refracted shock passing through the upstream wall of the bubble. Meanwhile, the reflected shock propagates inside the bubble and causes further refraction and reflection on the deformed surface. As a result of these interactions, the surface of the bubble deforms and a strong vortex develops in the entrainment region associated with the deformed bubble surface. This vortex evolves into a large vortex zone in the later stage as depicted in frame (c) of Fig. 1. Another remarkable feature of the flow structure at the later stage of the diverging case is a leftward jet that penetrates the downwind side surface of the bubble. The bubble itself is deformed into two completely separated small bubbles.

The flow structures in the converging case are sketched in Fig. 3.3, where the bubble density is larger than the ambient gas. The bubble works as a converging lens that focuses the flow toward the symmetrical axis after the shock passes through the bubble. The dotted semicircle in Fig. 3.3 (a) indicates the initial position of the bubble. As shown in frame (a), both refracted shock and reflected shock are generated when the incident

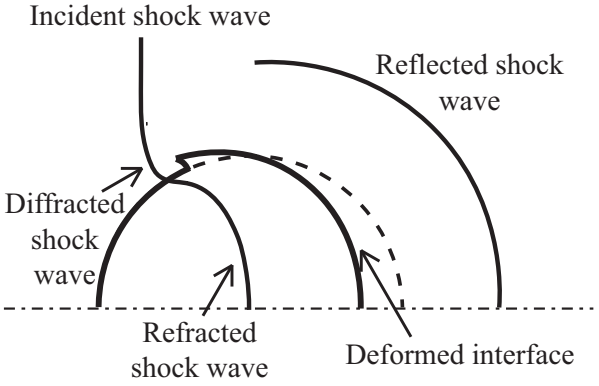

(a) Early stage of SBI.

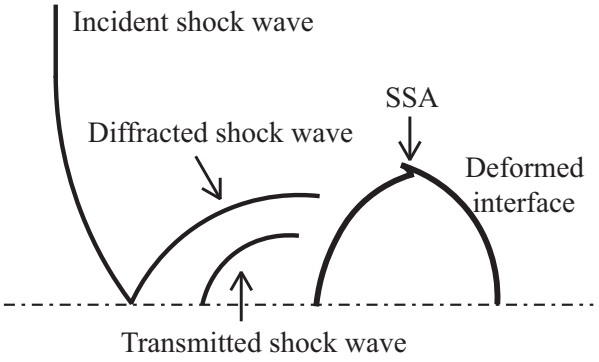

(b) Middle stage of SBI.

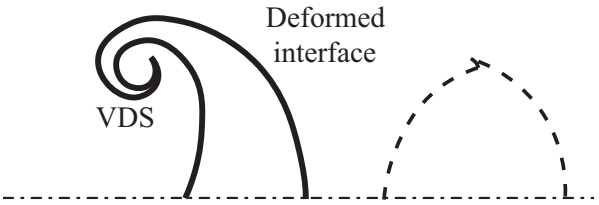

(c) Later stage of SBI.

Fig.3.3: Same as Fig.3.2, but for the converging case

shock collides with the bubble surface which undergoes a deformation but remains a less-distorted shape through the whole process (see Fig. 3.3 (b) and (c) as well). Different from the diverging case, the refracted shock wave within the bubble propagates at a rather slower speed. The incident shock propagates faster than the refracted shock inside the bubble, and a diffracted shock along the bubble surface develops. After a short period, as shown in frame (b), the diffracted shock detached from the surface when the upper

and lower components merge at the symmetrical axis. The transmitted shock, which is generated from the refracted wave passing through the downwind-side surface of the bubble, follows the diffracted shock. A strong shear area (SSA) forms around the tip of the bubble and results in at later time a vortical dominant structure (VDS) as shown in frame (c). The direction of the vortex is opposite to that of the diverging case.

3.2 Brief description of flow solver

3.2.1 Governing equations and numerical solver

In this work, we use the five-equation model developed by Allaire et al.[2] as the physical model, in which the material interface is assumed to be in an equilibrium of mixed pressure and velocity. The five-equation model consists of two continuity equations (one for each fluid), a momentum equation of mixture, an energy equation, and an advection equation of volume fraction as follows

$$\frac{\partial \alpha_1 \rho_1}{\partial t} + \nabla \cdot \alpha_1 \rho_1 \boldsymbol{u} = 0, \tag{3.4}$$

$$\frac{\partial \alpha_2 \rho_2}{\partial t} + \nabla \cdot \alpha_2 \rho_2 \boldsymbol{u} = 0, \tag{3.5}$$

$$\frac{\partial \rho \boldsymbol{u}}{\partial t} + \nabla \cdot (\rho \boldsymbol{u} \otimes \boldsymbol{u}) + \nabla p = 0, \tag{3.6}$$

$$\frac{\partial E}{\partial t} + \nabla \cdot (E\boldsymbol{u} + p\boldsymbol{u}) = 0, \tag{3.7}$$

$$\frac{\partial \alpha_1}{\partial t} + \boldsymbol{u} \nabla \cdot \alpha_1 = 0, \tag{3.8}$$

where $\alpha_1, \alpha_2 \in [0, 1]$ are the volume fractions of each fluid and ρ_1, ρ_2 their densities, respectively. $\boldsymbol{u}$, p, and E are the velocity, pressure, and total energy of the mixture, respectively. The density of the mixture is

$$\rho = \alpha_1 \rho_1 + \alpha_2 \rho_2. \tag{3.9}$$

With the Mie-Grünesen state equation[52] of the ideal gas, the pressure is obtained as follows

$$p = \rho e \Big/ \sum_{k=1}^{2} \frac{\alpha_k}{\Gamma_k}, \tag{3.10}$$

where $e = E - u^2/2$ and $\Gamma_k = \gamma_k - 1$ are internal energy and the Mie-Grünesen coefficient, respectively. γ_k is the heat capacity ratio of each fluid.

The numerical model detailed in [55] has been used for the deterministic simulation of the SBI phenomena. A finite volume method in wave propagation form[24] with the HLLC Riemann solver[64] is employed. The spatial reconstructions for physical variables are conducted with MUSCL[67] scheme except for the volume fraction field which is constructed by the THINC method[72,73]. The THINC method effectively prevents numerical dissipation errors that smears out the moving interface between different materials.

3.3 Uncertainty quantification method

For uncertainty quantification, we used the non-intrusive generalized polynomial chaos expansion[74] method with pseudospectral representation.

3.3.1 General polynomial chaos expansion (gPCE)

The generalized polynomial chaos expansion[78] represents uncertainty using basis polynomial expansion in terms of random variables. A solution $q(\xi)$ of a stochastic system can be represented by a set of orthogonal polynomial basis functions, $\boldsymbol{\phi} = \{\phi_0, \phi_1 \ldots, \}$, as follows

$$q(\xi) = \sum_{k=0}^{\infty} \hat{q}_k \phi_k(\xi). \tag{3.11}$$

The coefficients of gPCE are obtained from

$$\hat{q}_k = \int q(\xi)\phi_k(\xi)p(\xi)\mathrm{d}\xi \Big/ \int \phi_k(\xi)^2 p(\xi)\mathrm{d}\xi, \tag{3.12}$$

using the orthogonality of the polynomial basis. Here, $p(\xi)$ is the corresponding probability density function. In this paper, the Gaussian distribution

$$p(\xi) = \frac{1}{\sqrt{2\pi}} e^{-\frac{\xi^2}{2}} \tag{3.13}$$

is used as the initial distribution of uncertainty. Correspondingly, the probabilists' Hermite polynomial

$$\phi_k(\xi) = (-1)^k e^{\frac{\xi^2}{2}} \frac{\mathrm{d}^k}{\mathrm{d}\xi^k} e^{-\frac{\xi^2}{2}} \tag{3.14}$$

is employed as the orthogonal polynomial basis function to the Gaussian distribution.

The statistics of the random variable $q(\xi)$ can be then computed from the gPCE coefficients using the orthogonal characteristics of the basis. For example, the mean value is calculated from

$$E[q(\xi)] = \int q(\xi)p(\xi)\mathrm{d}\xi = \hat{q}_0, \tag{3.15}$$

and the second moment (standard deviation) is calculated from

$$E[q(\xi)^2] = \int q(\xi)^2 p(\xi)\mathrm{d}\xi = \sum_{i=0}^{\infty}\left(\hat{q}_i^2 \int \phi_i^2 p(\xi)\mathrm{d}\xi\right). \tag{3.16}$$

We quantify the uncertainties in a physical field by examining its mean value and standard deviation in this work.

In practice, a truncated gPCE is usually used with the polynomial basis up to N order,

$$q(\xi) = \sum_{k=0}^{N} \hat{q}_k \phi_k(\xi). \tag{3.17}$$

It is shown in[76] that the statistics evaluated with the truncated gPCE converges in a manner analogous to the spectral representation.

3.4 Uncertainty quantification of a flat interface - shock interaction

3.4.1 Numerical simulation setup

The configuration and initial conditions of numerical simulations are shown in Fig. 3.4, where the computational domain is a 200 mm $\times$ 89 mm rectangular region. The upper and lower boundaries are reflective walls. The right interface condition is set so as to sustain a left-propagating planar shock of pressure ration of upstream and downstream is 0.78, and the left side boundary allows free outflow. At the initial instant, a two-dimensional flat interface with a angle α is placed 50 mm from the right boundary. An initial planar shock is set along the cross-section 25 mm from the right boundary. The computational domain is partitioned by 1600 $\times$ 800 mesh cells of a Cartesian grid with uniform spacing $\Delta x = \Delta y = 0.0025D$.

We chose the Methane gas and CO2 gas for the upper and lower side of interface, respectively, in this work as those used in the prominent existing work[18]. The specific heat ratios γ and densities ρ for the gases and air used in the standard base simulations are shown in Table 3.1.

3.4.2 Uncertainty simulation on SFI process

In this thesis, we evaluate the discretized projection of the density and pressure due to the initial uncertainty of bubble density in the numerical simulation of SFI to obtain the statistics for physical quantities. Henderson et al.[18] in their study, showed that the experimental and simulation results agree well within the range. This was proved by considering the effect of impurities caused by gas penetration, comparing the experimental results and the simulation results, and using numerical simulation based on the transition between interaction structures. However, the arguments on the stability of each structure are found not to be sufficient. The uncertainty in the initial density of CO2 gas is set to 10% of the density. Assuming that the uncertainty follows a Gaussian distribution, we set the density of bubble gas, which is identified as fluid 2 in our context, with uncertainty as follows

$$\rho_2(\xi) = \rho_2^*(1 + 0.1\xi), \tag{3.18}$$

where ρ_2^* is the density of CO2 gas without uncertainty and ξ is a random variable following the standard Gaussian distribution. The number of quadrature points used to calculate the coefficients of the discretized projection is 17. A numerical solution at each quadrature point is obtained by the flow solver outlined in Section 3.2. Then, the coefficients of the discretized projection of 16th order are calculated from (2.24). Finally, the statistics are evaluated using the gPCE as shown in equations (3.15) and (3.16).

Table 3.1: Physical properties of pure gases

Name	γ	μ[g/mol]
Methan	1.288	16.04
Carbon dioxide	1.303	44.01

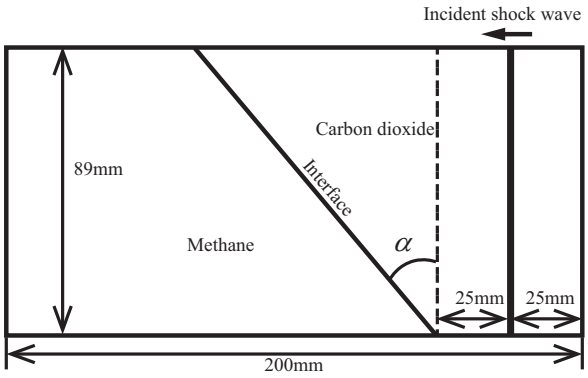

Fig.3.4: Configuration of computational domain and initial condition

3.4.3 Interaction structure of SFI

The effect of uncertainty on the interaction between shock wave and interface in multiphase flow is represented by four cases (RRE: The regular shock refraction, BPR: The bounded precursor refraction, FPR: The free precursor regression, FNR: The Report on free precursor von Neumann refraction). Fig. 3.5 to 3.8 shows shock/interface interaction structure and uncertainty for $\alpha = 32°, 38°, 38°, 50°, 65°$, respectively. Each figure is composed of two frames, where the left and right frames differ only in the minimum and the maximum values of the color map. In each figure, the contour of the density is shown by a gray solid line, and the standard deviation of the pressure caused by the uncertainty is shown by a white-red color map. The contour line of the density has an interval of 0.01 [kg/m3] which can locate the position of the shock wave and the interface.

The effect of uncertainty can be seen from the color map of the standard deviation of pressure. The impact of uncertainty on the shockwave can be divided into three aspects: strength, tilt, and position. In this thesis, we first discuss the influence of uncertainty on the location of the shock wave in order to focus on the change in the interaction structure due to the uncertainty. Therefore, in the left frame, in order to confirm the influence of the uncertainty in the position of the shock wave, a white-red gradient color map is drawn with minimum and maximum values of 300 Pa and 2000 Pa respectively. The influence of the uncertainty on the position of the interaction structure can be compared by the width of the portion drawn in red in the color map. The thicker the red region

around a structure, the more the position changes due to the effect of uncertainty, and the structure with a smaller width or a region that does not appear red is less affected by the uncertainty. The color map of the right frame represents 0 Pa as white and 200 Pa or more as red. In this color map, the influence of the uncertainty appears on the strength of the pressure field. The white region represents that the strength of the pressure field remains unchanged due to the influence of the uncertainty whereas the dark red region represents that the strength of the pressure field changes due to the influence of the uncertainty.

In each figure, structures classified as RRE, BPR, FPR, and FNR appear clearly. Here, each structure will be briefly described. The RRE structure appearing in Fig. 3.5 is typically a regular refraction structure. When the shock wave (Incident shock, f) joined to the shock wave (Reflected shock, r) reflected at the contact point (R) with the shock wave (Incident shock i), a Deformed surface (d in the figure) appears due to the combination of the transmission shock (t in the figure) and the combined action with the shock wave.

The Irregular refraction structure FPR appears in Fig. 3.7. In FPR, the transmitted shock (t) propagates earlier than the original shock wave (Incident shock). Therefore, the point of contact between the transmitted shock and the interface (Precursor P) leaves the point of contact between the original shock wave and the interface (R). At the contact point between the transmitted shock and the interface (P), the shock wave propagating in the methane gas layer is refracted to generate a new shock wave (Side shock s). Side shock interacts with Incident shock and leads to Reflected shock. The lower part (Modified shock) of Incident shock affected by Side shock forms a Centered expansion pan (e) at the interface, and finally leads to the Reflected shock (r).

BPR appears in Fig. 3.6. BPR is one of the types of Irregular refraction where the velocity of Transmitted shock and the interface with the precursor (P), and the velocity of the contact point of the incident shock and the interface (R) are same, but different from RRE. It can be distinguished from the shape of the transmission shock (t) bending in the propagation direction around it. Since, the incident angle to the interface of the Incident shock exceeds the critical angle with no solution applying to regular reflection, it is classified as Irregular reflection.

FNR structure appears in Fig. 3.8. FNR is a structure in which the precursor (P) and the setting of the interface (R) are clearly separated as in the FPR described above,

but the reflection at the interface becomes Mach reflection. The reflection structure is a typical Mach reflection that is Mach stem (n) and Reflected shock (r). In addition, after Side shock (s) developed from Precursor integrates with Incident shock, it joins with Reflected shock (r') and forms another shock wave (r).

3.4.4 Effect of Uncertainty on SFI

This section reports the effects of uncertainty on each structure. As described in the beginning of this section, the width of the red region in the color map of the left frame allows to assess the impact of uncertainty on each structure. On the other hand, the color map of the right frame can evaluate the influence of the uncertainty on the pressure field strength.

From the let frame of Fig. 3.5, it can be illustrated that Transmitted shock is affected by uncertainty in RRE. The impact of uncertainty on Reflected shock is very small. From this, it can be understood that in the case of regular refraction, uncertainty due to the mixing of carbon dioxide introduced into the methane layer has a major influence on the position of the transmitted shock. It is characteristic that the influence of uncertainty decreases on the interface side. The right frame shows that the pressure field strength is affected by the same degree of uncertainty both inside and outside the interface. In addition, it can be confirmed that there is a region less susceptible to uncertainty where the Expansion fan (e) starts to develop. There is an area that is less susceptible to uncertainty even near the interface behind Transmitted shock.

From BFR in Fig. 3.6, it can be confirmed from the left frame that not only Transmitted shock but also Reflected shock are affected by uncertainty. This means that the influence of the uncertainty of the methane layer is transmitted across the interface, and indirectly confirms that Precursor develops by the transmission shocks affected by the uncertainty interacting at the interface. From the lower frame, as in RRE, it is observed that the pressure field changes regardless of region (inside and outside) of the interface. But it is observed that the region where the expansion fan begins to develop and the region behind the transmitted shock are affected by uncertainty.

As shown in the left frame of Fig. 3.7, it can be observed how the influence of uncertainty

in FPR is transmitted from Transmitted shock to Reflection shock via Side shock. Such a tendency can also be confirmed from the FNR in Fig. 3.8. In the FNR, it can be observed that the influence of uncertainty on another Side shock (r ') is also prominent. Although the Mach stem in the FNR (n) is also affected by the uncertainty, the main uncertainty effects appear in the Side shocks and Reflected shocks linked to the transmitted shock. From the right frame of Fig. 3.7 and Fig. 3.8, the region which is less susceptible to uncertainty around the interface is found behind the Transmitted shock connected to the interface. At the point where the expansion fan begins to develop through the point of contact between the interface and the modified shock (R in the figure), a characteristic phenomenon linked to the region less susceptible to uncertainty was also observed.

In case of the precursor develops (BPR, FPR, and FNR), transfer of the effect of the initial density uncertainty over interface via the precursor position was observed commonly as shown in left frame of Fig. 3.6, 3.7, and 3.8. Because precursor is the point where the transmitted shock propagating contaminated media interacts the other side of the interface, this transfer of the effect of uncertainty is considered reasonable. The precursor is where the transmitted shock which affected by the uncertain contaminant refracted outside interface. The interaction between the affected transmitted shock interface generates interaction structures. Thus, generated interaction structures such as side shock, quadruple point, and refracted shock or fan affected by the change on the transmitted shock. Whereas, in the RRE case in Fig. 3.5, the transmitted shock affected by the density uncertainty only propagate inside the contaminated media. Also, the uncertainty of acoustic impedance resulted from the contaminant only affect the transmitted wave following the fundamental law of refraction. This knowledge about transfer characteristic of the uncertainty implicates whether the reflected shock structures affected by the contaminant or not could be used to classify the regularity of the structure. The irregular reflection structure would be affected by the uncertainty, whereas the regular structure does not.

Fig.3.5: Shock-interface interaction structure with $\alpha = 32\,\mathrm{deg}$. Interval of contour lines is 0.01 kg/m^3. And maximum and minimum values of white-red colormap are 300Pa and 2000Pa (left), 0Pa and 200Pa (right) respectively.

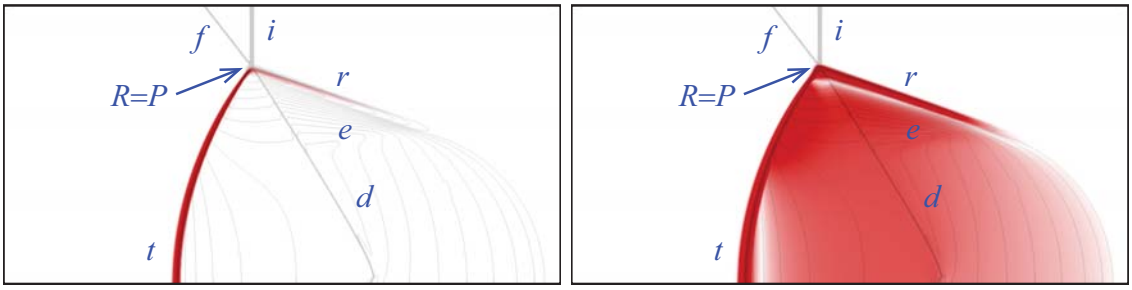

Fig.3.6: Shock-interface interaction structure with $\alpha = 38\,\mathrm{deg}$. Legends are same as Fig. 3.5.

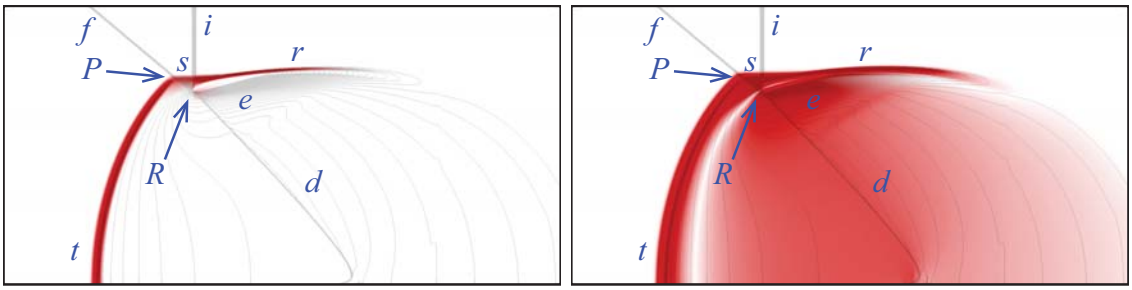

Fig.3.7: Shock-interface interaction structure with $\alpha = 50\,\mathrm{deg}$. Legends are same as Fig. 3.5.

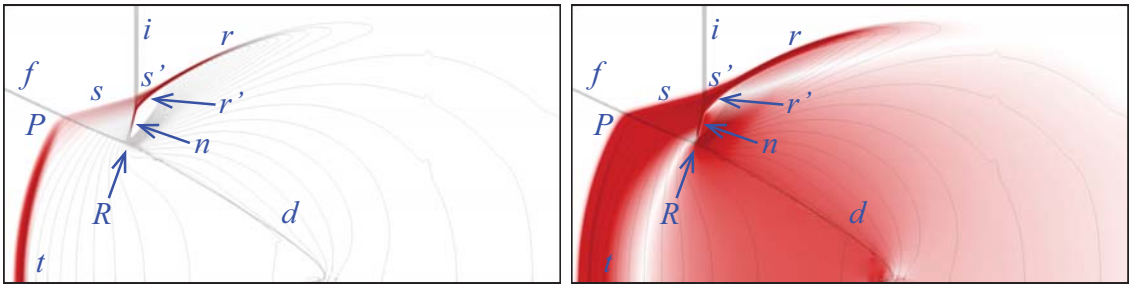

Fig.3.8: Shock-interface interaction structure with $\alpha = 65\,\mathrm{deg}$. Legends are same as Fig. 3.5.

3.4.5 Mention about the low standard deviation region of SFI

Another significant finding is that in every case, there are low-density-variance regions that are localized behind shock structure. As mentioned in the upper part of this section, the uncertainty in methane media resulted from contaminant of CO2 results in LSDA. A series of additive statistical analysis was conducted to study the characteristics of these LSDAs. First, the pressure field of IQR points, the point where correspond with 25%, 50%, and 75% of the cumulative distribution function (CDF), is estimated from the reconstructed probability density function of the pressure field with stochastic collocation method. Moreover, the difference between Q3 point corresponding with 75% of CDF and Q2 point, the median, of pressure field was calculated as shown in Fig. 3.9. The pressure difference is represented with the blue-white-red colormap. The white region is where the difference between Q3 and Q2 is neglectable. These regions are the same as LSDA, which implicate the pressure difference could be assumed as monotone. The blue-colored regions are where the pressure of Q3 point is less than that of Q2 point, and the red-colored regions are where the Q3 point shows more considerable pressure value than Q2 point.

The low-density-variance regions and the regions where the pressure difference between Q3 and Q2 point is almost zero coincided. Moreover, for irregular refraction cases, the low-density-variance regions are connected at the foot of incident shock. In the interface side, the density uncertainty increases the pressure of the media, and the density uncertainty decreases pressure in the shock side of the region. The tendency of effect on pressure of the density uncertainty in the interface side agrees with the fundamental rule of the refraction, although the discussed phenomenon is irregular refraction. The more contaminated media on Q3 point compared with Q2 point has a lower refracted index, and the speed of the transmitted shock is slower than that of Q2 point. Thus, the density of Q3 media after the shock transmitted became higher than Q2. This density difference could make the pressure difference by assuming the shock propagation as an isentropic process. Moreover, the change of effect direction around the LSVA could be understood with the concept of acoustic impedance. The interface side is where the transmitted shock is generated from the refraction of the incident shock of high impedance area and uncertain impedance area.

On the other hand, the transmitted shock refracted outside of interface from uncertain media, where the effect of uncertainty react with the inverse side. The effect of uncertainty and the existence of LSDA has been reasoned from expanding the regular refraction-reflection characteristic to irregular refraction-reflection.

3.4.6 Wave angle of calculated result

The wave angles of the interaction structures attain from numerical solver are represented in Table 3.2. For the comparison data, a data attained from a graph of Henderson[18] is used. In case of there exist multiple experimental data around discussed angle, range is revealed instead of the value. Wave angle of transmitted shock α_t, expansion pan α_e or side shockα_s, and deformed surface δ is represented. Each wave angle was measured from the initial interface. First, the simulated values are satisfactorily agree with the experimental results. Most of values were inside the experimental measurement range, and in case of simulation value does not included range, the mismatches were less than 2 $^\circ$ which is affordable for measurement of experimental result.

For the comparison data, data attained from a graph of Henderson[18] is used. In case there exist multiple experimental data around the discussed angle, the range is revealed instead of the value. Wave angle of transmitted shock α_t, expansion pan α_e or side shockα_s, and deformed surface δ is represented. Each wave angle was measured from the initial interface. First, the simulated values satisfactorily agree with the experimental results. Most of the values were inside the experimental measurement range. Even the simulation values do not include in range, the mismatches were less than 2 $^\circ$, which is affordable for measurement of experimental result.

The distribution tendency of experimental result Henderson measured agree with the effect of uncertainty on the interaction structure discussed the former part of this section. For every four cases, the measured angle of the transmitted shock shows distribution as discussed with the effect of the uncertainty on the transmitted shock. Moreover, the wave angle of expansion fan or side shock attained from experiments distributed in range with the three cases where the precursor appears as predicted with the uncertainty quantification result. These acceptances with experimental results support our quantification

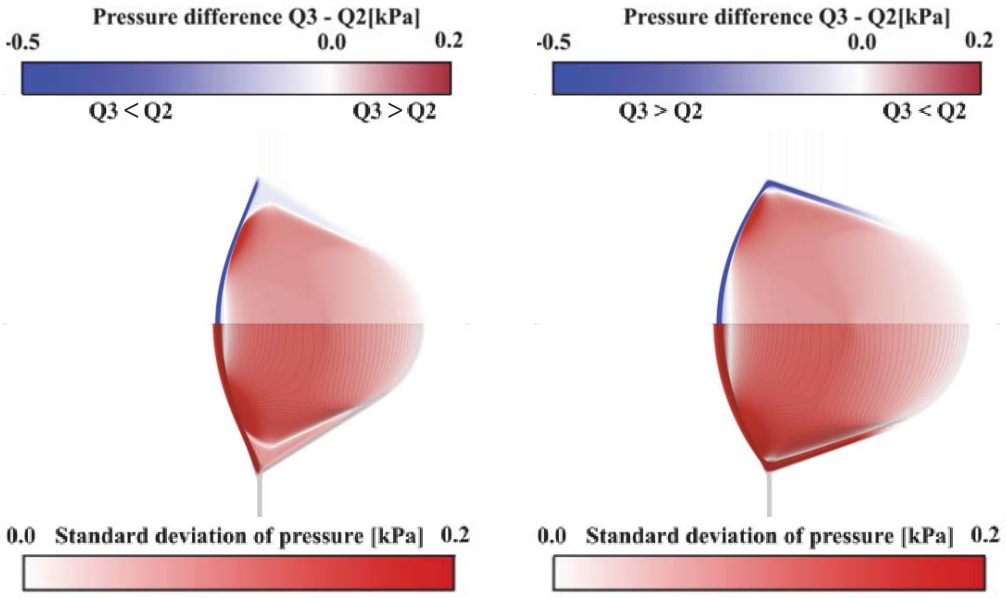

(a) RRE case. $\alpha = 32°$.

(b) BPR case. $\alpha = 38°$.

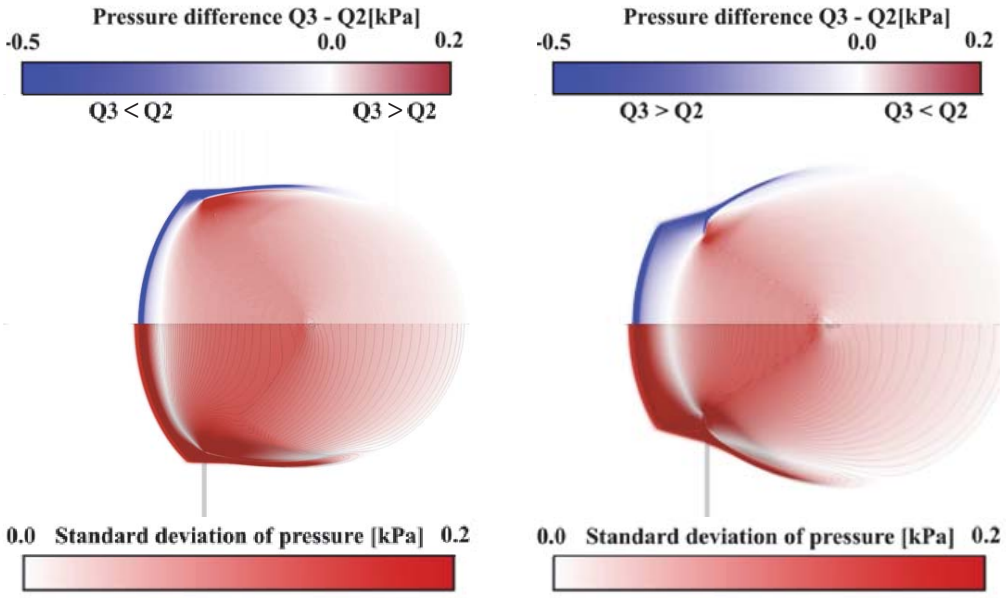

(c) FPR case. $\alpha = 50°$.

(d) FNR case. $\alpha = 65°$.

Fig.3.9: Pressure difference between Q2 point (median) and Q3 point (75% point of CDF) of four SFI cases. Standard deviation of pressure is also plotted for comparison.

results are acceptable.

Table 3.2: Wave angle of interaction structure attained from current simulation and experimental result of reference[18].

	$\alpha[^\circ]$	$\alpha_t[^\circ]$	$\alpha_e[^\circ]$ or $\alpha_s[^\circ]$	$\delta[^\circ]$
Exp.[18]	32	55∼62	27	6
Sim.	32	53	25	6
Exp.[18]	38	72∼91	33∼36	5
Sim.	38	85	38	6
Exp.[18]	50	92∼105	37∼48	4
Sim.	50	97	40	5
Exp.[18]	65	92∼110	37∼40	7∼9
Sim.	65	97	41	7

3.5 Uncertainty quantification of the shock bubble interaction

3.5.1 Numerical simulation setup

The configuration and initial conditions of numerical simulations are shown in Fig. 3.10, where the computational domain is a 200 mm × 89 mm rectangular region. The upper and lower boundaries are reflective walls. The right interface condition is set so as to sustain a left-propagating planar shock of Mach number $M_\mathrm{s} = 1.22$, and the left side boundary allows free outflow. At the initial instant, a two-dimensional cylindrical bubble with a radius of $D = 50$ mm is placed 45 mm from the right boundary. An initial planar shock of $M_\mathrm{s} = 1.22$ is set along the cross-section 10 mm from the right boundary. The dash-dotted line shows the symmetrical axis, and only the upper half-domain is calculated. The computational domain is partitioned by 1600 × 356 mesh cells of a Cartesian grid with uniform spacing $\Delta x = \Delta y = 0.0025D$.

Although many recent works on SBI use other gases for the bubble[28,81], we chose the legacy Helium gas mixed with 28% of air and R22 for the bubble in diverging and converg-

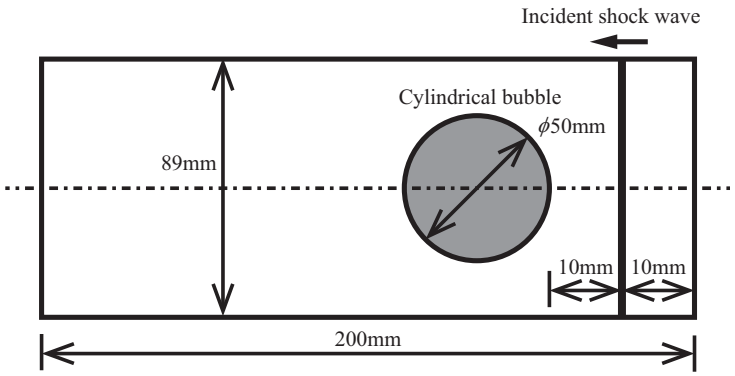

Fig.3.10: Configuration of computational domain and initial condition

Table 3.3: Standard physical property of the gases used in numerical simulations

Gas species	γ	ρ [kg/m^3]
Air	1.4	1.225
Helium	1.648	0.219
R22	1.249	3.863

ing cases, respectively, in this work as those used in the relevant existing works[16,25,45,54]. The ambient fluid is air. The specific heat ratios γ and densities ρ for the gases and air used in the standard base simulations are shown in Table 3.3.

3.5.2 Uncertainty simulation on SBI process

In this thesis, we evaluate the discretized projection of the density and pressure due to the initial uncertainty of bubble density in the numerical simulation of SBI to obtain the statistics for physical quantities. The uncertainty in the initial density of bubble gas is set to 10% of the density with reference to[16]. Assuming that the uncertainty follows a Gaussian distribution, we set the density of bubble gas, which is identified as fluid 2 in our context, with uncertainty as follows

$$\rho_2(\xi) = \rho_2^*(1 + 0.1\xi), \tag{3.19}$$

where ρ_2^* is the density of bubble gas without uncertainty and ξ is a random variable following the standard Gaussian distribution. The number of quadrature points used to calculate the coefficients of the discretized projection is 17. A numerical solution at each quadrature point is obtained by the flow solver outlined in Section 3.2. Then, the coefficients of the discretized projection of 16th order are calculated from (2.24). Finally, the statistics are evaluated using the gPCE as shown in equations (3.15) and (3.16).

We have evaluated the impact of the number of sample calculations on the statistics results by comparing the 17-sample results with the results of 33- and 65-sample runs. As shown in appendix A, the results of the SBI simulations of 17 samples adequately converge regarding the probability quantities of interest in this thesis.

3.5.3 Density and pressure fields of SBI

We have examined the uncertainties in density and pressure in the whole computational domain for both the diverging case (Fig. 3.11 and Fig. 3.12) and converging case (Fig. 3.13 and Fig. 3.14), where the six snapshots are displayed for different instants corresponding to those in the literature [16,45].

In these figures, we plot the numerical results of the deterministic computations with the standard material properties given in Table 3.3 by black contour lines. The color map fields represent the magnitude of the standard deviation values quantified at each mesh cell, which were calculated by the pseudospectral approach described in section 3.3 using 17 sample runs with uncertainty in initial bubble density.

It is observed that significantly high standard deviation appears in the vicinity of the structures where physical fields have large gradients, e.g., the material interface (or front) and shock waves in density field. The simulation results reveal that rather than the strength of the flow structures, the impact of the uncertainty on the position of the structures is much more dominant. Thus, the magnitude of the standard deviation shown in the color map mainly corresponds to the uncertainty in the position of shocks or fronts.

The density fields provide the information of location and standard deviation (uncertainty) for both shocks and bubble fronts, while the structures of shocks can be identified

more clearly from the pressure fields.

Diverging case: with helium bubble

Figures 3.11 and 3.12 show the SBI of diverging case explained in section 3.1.2. In each figure, frame (a) visualizes the generation of the refracted and reflected shocks as a result of the interaction between the upstream bubble surface and the incident shock. As time passes, with the propagation of the refracted shock and the typical structures of the diverging case, such as the side shock, modified incident shock and quadruple point, develop in the frame (b) afterward. The refracted shock propagates in the diverging direction and reaches the opposite side of the bubble as shown in frame (c). In frames (d) and (e), the transmitted shock propagates out of the bubble and a weak shock generated from the refracted shock reflects back inside the bubble. The material front after the interference with the shocks at 245 μs is plotted in frame (f). Its upstream side has been deformed into a concave shape at this stage.

From frame (a) to (d) in both density and pressure fields, no uncertainty effect on the incident shock is observed. In contrast, the uncertainty significantly affects not only the refracted shock but also the flow structure around the quadruple point, particularly on the side of the reflected shock. As time passes, the effects on characteristic structure become clear as shown in frame (c). The transmitted shock, formed from the side shock and refracted shock, has significantly been affected by the initial bubble density, which is shown as the large standard deviation in frames (d) and (e).

The bubble surface is also affected by the uncertainty as shown in Fig. 3.11. At the early stage shown in frame (a) of Fig. 3.11, the upstream bubble surface where the incident shock directly strikes is deformed, but the effect of bubble density on the interface position is not visible immediately. As the interaction continues, the uncertainty effect on the motion of the upstream side bubble interface is becoming increasingly significant, especially the most movable part near the symmetrical axis. On the other hand, the uncertainty does not affect the downstream surface until the refracted shock, which propagates within the bubble under the influence of the uncertainty in bubble density, interacts with the downstream surface, as shown in frames (b) and (c). From frames (d) and (e), it is revealed that the effects of the uncertainty on the bubble surface remain after the shock

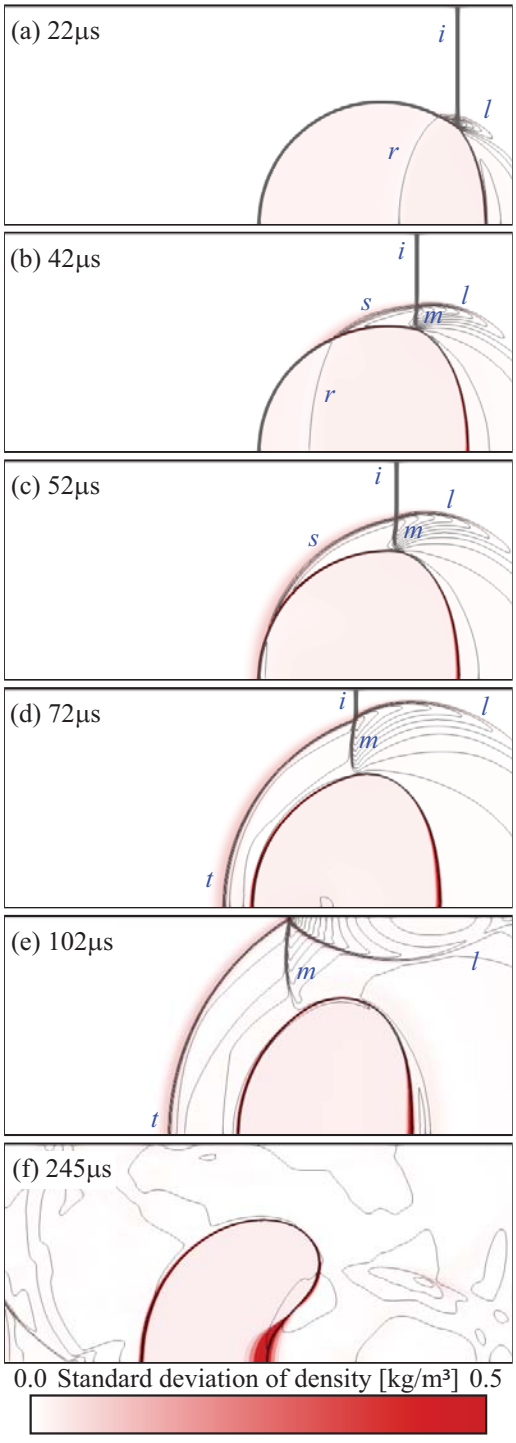

Fig.3.11: Contour lines of the density with the effects of the uncertainty in initial bubble density for SBI of a Mach 1.22 shock with a cylindrical Helium bubble. The black lines are contour lines with interval of 0.05 kg/m^3 and the standard deviation is represented with white-red color map. The incident shock is labeled by i, side shock by s, modified incident shock by m, reflected shock by l, refracted shock by r and transmitted shock by t

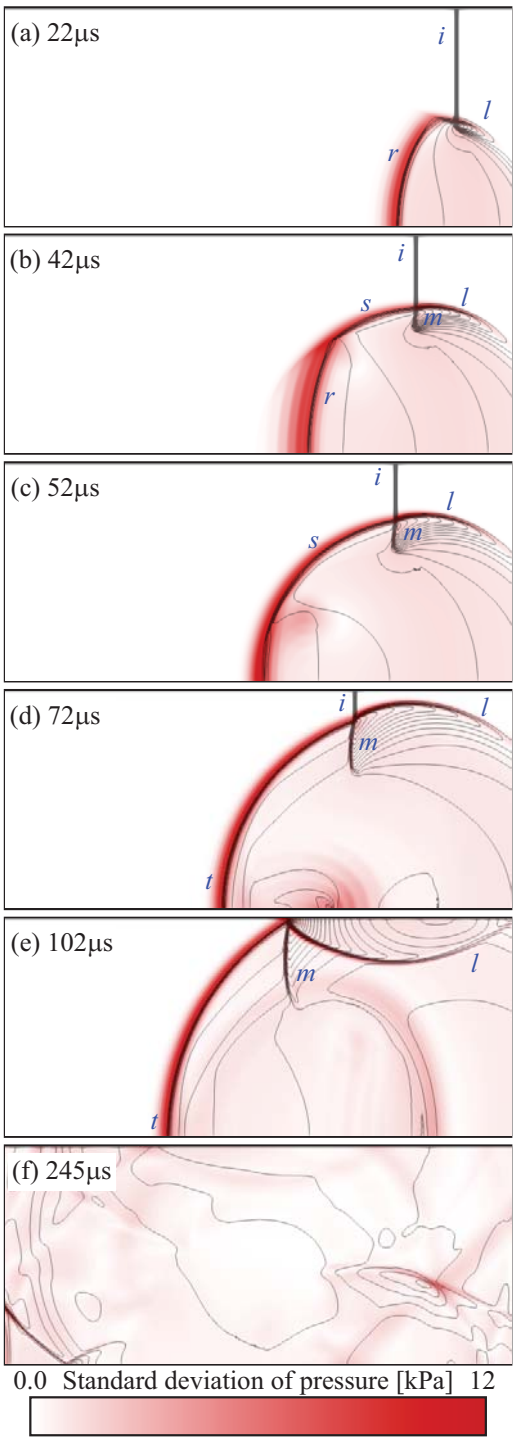

Fig.3.12: Same as Fig. 3.11, but for the pressure fields. The black contour lines have an interval of 5 kPa

moves apart from it. The impact of the uncertainty on the deformation of the bubble surface is amplified in the later stage, as shown in frame (f).

Converging case: R22 bubble

Figures 3.13 and 3.14 visualize the density and pressure fields of the SBI of the converging case explained in section 3.1.2. We can observe the propagation of a refracted shock in the frames from (a) to (c). At the foot of the incident shock on the bubble surface, diffraction occurs and the diffracted shock develops. The refracted shock forms a bent shape as shown in the frames from (b) to (e), which converges toward the symmetrical axis. the speed of the incident shock and the diffracted shock is faster than that of the refracted shock. Consequently, the refracted shock propagates and interferes with its symmetrical counterpart, and the diffracted shocks cross each other as observed in frame (d). The propagation of the refracted shock eventually results in the transmitted shock through the downstream bubble surface as shown in frame (e). The final state of the simulation is plotted in frame (f), where the incident shock goes out from the computational domain and the bubble, though deformed, remains as a single bubble.

Effects of the uncertainty on the SBI structures of the converging case can be examined through the color maps of the standard deviation shown in Figs. 3.13 and 3.14. As plotted in frames (a) to (c), the incident shock and the diffracted shock are nearly not affected by the uncertainty. On the other hand, there is a high standard deviation area around the refracted shock which means that the refracted shock is profoundly affected by the uncertainty in bubble density. The refracted wave in the bubble also has high standard deviation as shown in frame (d), which consequently results in the large uncertainty impact on the transmitted shock in frame (e).

Effects of the uncertainty on bubble surface can be evaluated from the density field (Fig. 3.13). The upstream side surface and the downstream side surface of the bubble are affected by the uncertainty in a different way. The upstream surface directly interacts with the incident shock, as represented in frames from (a) to (f), while the downstream surface is substantially affected by the diffracted shock and the refracted shock in the interference process as observed in the frames after (b). The refracted shock plays a more important role at the later stage as shown in frames (d) and (e). The uncertainty effects

on the bubble surface remain even after the shocks pass away (Fig. 3.13 (f)).

3.5.4 Volume fraction fields of SBI

As discussed above, the deformation of the bubble surface on the upstream side and the downstream side are due to different interference processes. On the upstream side, the incident shock dominates the interactions. By contrast, the refracted shock and other secondary waves, such as the side shock in the diverging case and the diffracted shock in the converging case, are of more importance in the interactions on the downstream side. More profoundly, the material properties of the bubble, such as the density and sound speed, affect more substantially the interactions and thus the motion of the bubble surface.

The effects of the uncertainty on the bubble surface are represented by the color maps of the standard deviation of the volume fraction (or VOF: volume of fluid) field in Fig. 3.15 for the diverging case and Fig. 3.16 for the converging case. In frames (a) of both cases, two separated high standard deviation areas corresponding to the upstream and downstream parts of the bubble surface can be clearly identified. Between these two areas, there is an intermediate area where the standard deviation is low which, referred to as LSDA (low standard deviation area) in our context, implies that the motion of bubble surface in this area is not affected by the uncertainty.

As the bubble surface is transported by the flow in the normal direction, the uncertainty impact on the surface motion can be also used to estimate the flow pattern around the bubble surface. The LSDA corresponds to an area where the ambient fluid moves dominantly in the tangential direction to the bubble surface, which forms a strong shear flow across the bubble surface. So, the LSDA at the early stage has a great potential to develop a vortical structure later in the SBI process.

The effects of the uncertainty on the bubble surface motion become more complicated as the deformation of the surface and the flow structure develop. For the diverging case, the standard deviation of the upstream side of the bubble surface becomes more significant, particularly the most deformed part near the symmetrical point, as shown in Fig. 3.15(b). However, for the converging case, the standard deviation of the downstream side

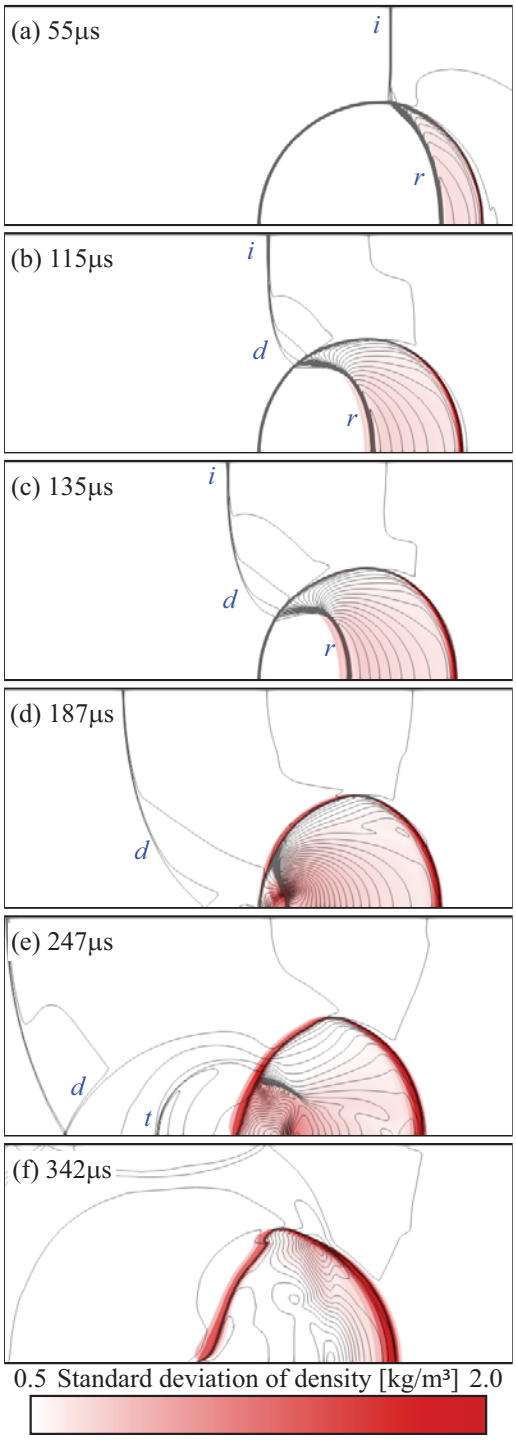

Fig.3.13: Same as Fig.3.11, but for the converging case (SBI of R22 bubble). The black contour lines are plotted with an interval of 0.1kg/m^3 and the standard deviation is represented with white-red color map. In addition to wave structures in Fig.3.11, the diffracted shock is labeled by "*d*".

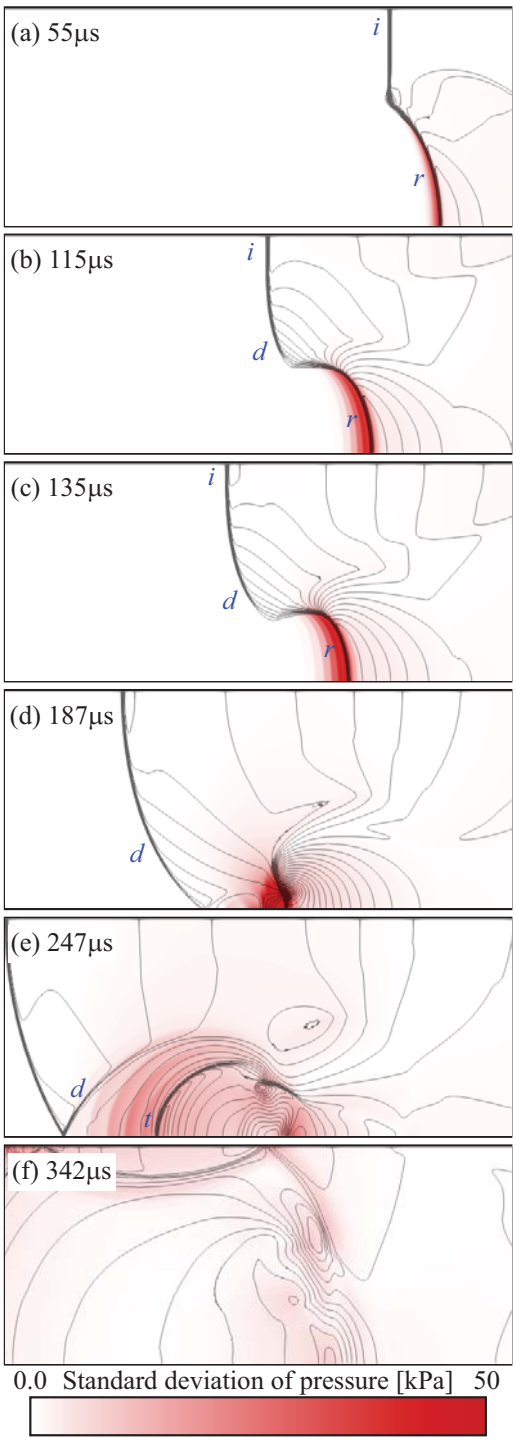

Fig.3.14: Same as Fig. 3.13, but for the pressure fields. The black contour lines has an interval of 5 kPa

is comparable to the upstream side. It indicates that a light bubble is more likely to be deformed on the upstream side. The LSDA spreads along the surface of the separated bubbles corresponding to an extended vortical region covering the bubble and its vicinity (Fig. 3.15(c)). In the converging case, vortical structure develops around the LSDA appearing at the earlier stage and part of the LSDA of VOF persists through the entire process (Fig. 3.16(c)).

As mentioned above, LSDA in the VOF field might implicate a tangential dominating shear flow across the bubble surface, which can be connected to the vortical structure developed later on. It indicates the necessity of further research to clarify the relationship between the LSDA and the development of vortical structures.

3.5.5 Uncertainty impacts on propagation of different waves and bubble surface

In this section, we quantitatively evaluate the effect of the initial uncertainty in bubble density on the propagation speeds of the waves and bubble surface in the SBI simulations discussed before.

The speeds of the refracted shock (v_{r}), transmitted shock (v_{t}), initial (or early stage) upstream bubble wall (v_{ui}), final (or later stage) upstream bubble wall (v_{uf}), initial downstream bubble wall (v_{di}) and final downstream bubble wall (v_{df}) have been examined for diverging and converging cases. For the diverging case, we also estimate the speed of the jet (v_{j}) that occurs at the center of upstream bubble surface and penetrates through the bubble along the symmetrical axis.

The $x-t$ diagrams of both diverging case (helium bubble) and converging case (R22 bubble), such as those shown in Fig. 3.17 and Fig. 3.18, are generated to estimate the velocities of different flow structures. In Fig. 3.17 and Fig. 3.18, we plot the positions of the bubble surface and different waves computed from the deterministic simulation with the material properties in Table 3.3. Positions of the upstream bubble surface in the early stage (denoted by "ui") and later stage (denoted by "uf") are represented by blue cross marks, and blue diamonds represent the locations of the downstream bubble surface (denoted by "di" in the early stage), which coincides with the upstream surface when the central jet (denoted by "j") penetrates the bubble in the diverging case. In the

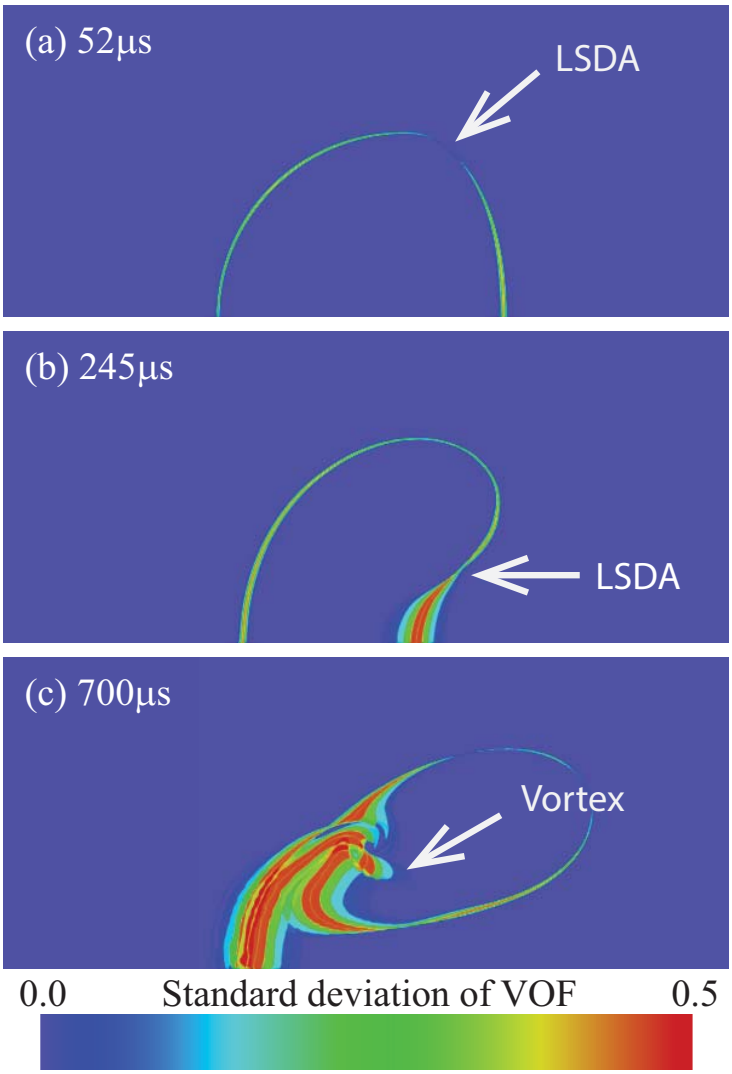

Fig.3.15: Color map of standard deviation of VOF value of diverging case

converging case, the downstream bubble surface in the later stage (denoted by "df") does not coincide with the upstream bubble surface, and the bubble remains as a whole during the process. The blue triangles correspond to the position of the refracted shock (denoted by "r") which becomes the transmitted shock (denoted by "t") in the later stage.

The location of a shock is identified by the density peak along the symmetric line at different instants over the distance the corresponding wave travels, and the position of the bubble surface is measured by detecting the $\alpha_1 = 0.5$ contour of the VOF field.As all the flow structures evolve in time, and propagation speed for each structure may change during different time period, the speed of each structure is measured within a certain

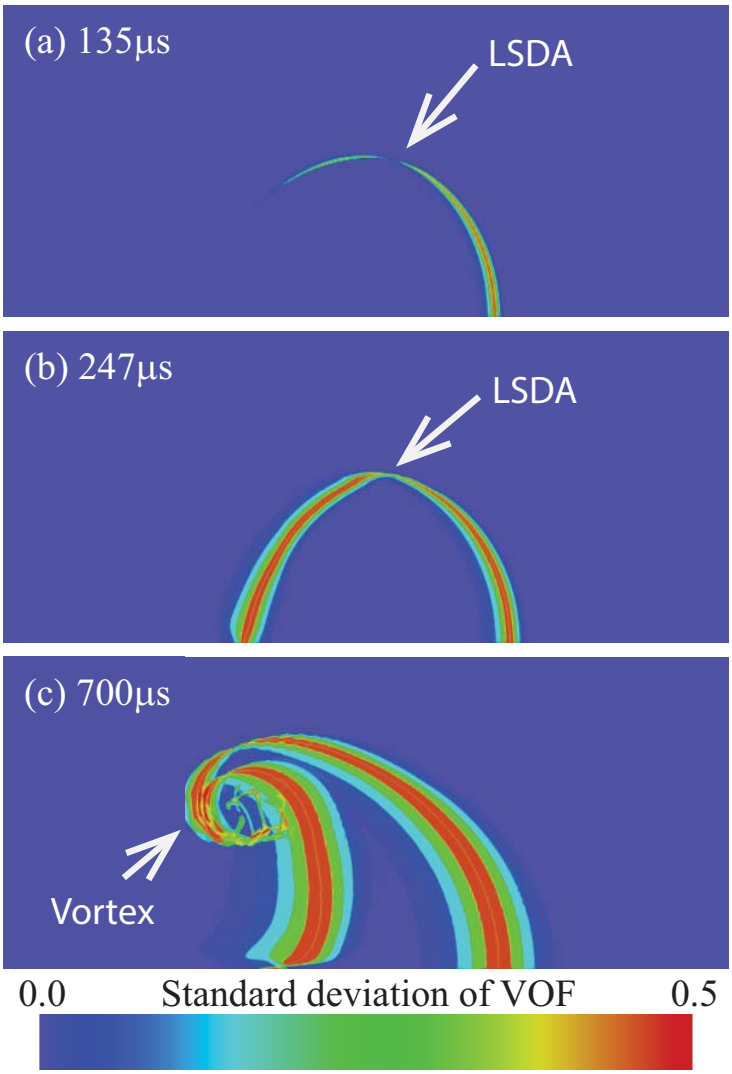

Fig.3.16: Same as Fig. 3.15, but for converging case

time slot as shown in Table 3.4 for diverging case and Table 3.5 for converging case. We measured the position of each flow structures in every microsecond and obtained the velocity of each flow structures using the least squares method inside the time slot.

To reduce the measuring uncertainty, we determined these time slots in where the changes in positions of flow structures are almost linear for every 17 cases. For the bubble surfacs where the speed change is significant than the shocks, we set plenty of measuring points (101 points for the diverging case, more than 601 points for the converging case). The $x-t$ diagram is created for each sample simulation with different initial bubble density to extract the velocities of different flow structures. The statistics of these velocities are

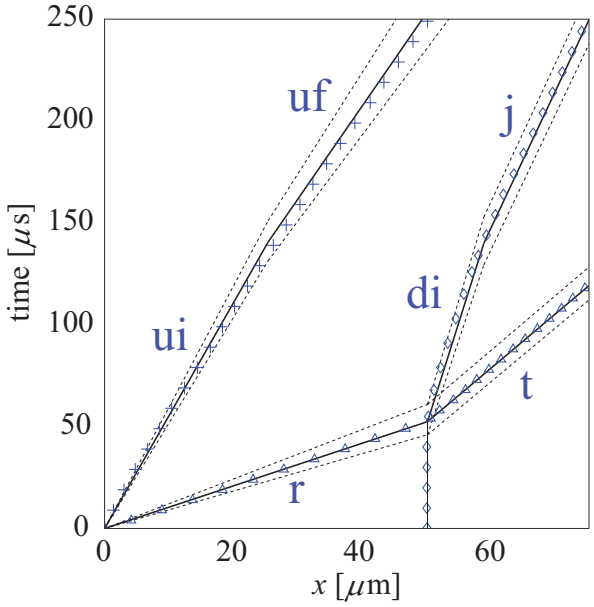

Fig.3.17: $x-t$ diagram of characteristic velocities in diverging case (heliumbubble). "+" indicate the locations of the upstream bubble surface in early stage "ui" and later stage "uf" from the deterministic simulation, "◊" the downstream bubble surface in early stage "di" and later stage "j" where the jet penetrates through the bubble, "△" the refracted and transmitted shocks. Solid lines show the mean values of various velocities obtained from the simulations with uncertainties, while dashed lines indicate the three-time standard deviations

obtained using the gPCE with the spectral collocation method described above.

Diverging case (Helium bubble)

We give the averaged (mean) propagation speeds ($\bar{v}$) of different structures and their standard deviations ($\sigma(v)$) in Table 3.6 for the diverging case. The results from the deterministic computation (v) with the standard material properties (Table 3.3), as well as the simulation results of other existing works are also included for comparison[16,31,45].

It is found that the statistical mean velocities of all flow structures are different from but very close to those of the results of the deterministic simulation with the standard material properties (with a discrepancy less than 0.3 %). However, the standard deviation ($\sigma(v)$ or $\sigma(v)/\bar{v}$) varies significantly for different flow structures. The uncertainty in initial bubble

Table 3.4: Time slots used for velocity measurement in the diverging case (helium bubble). t_t is the instant when the refracted wave passed through the downstream wall of the bubble

Velocity	start time [μs]	end time [μs]
v_r	0	25
v_t	t_t	t_t+188
v_ui	10	52
v_uf	140	240
v_di	t_t	140
v_j	140	240

density has a large impact on the velocity of the refracted shock (4.6%). The uncertainty also significantly affects the upstream bubble surface (2.3% for the early stage and 2.7% for jet in the later stage) and the downstream bubble surface in early period (3.0%). Nevertheless, the uncertainty has less effect on the final bubble surface (0.4%) and the transmitted shock (0.3%).

These observations agree well with the conclusions drawn from the existing literature that the structures with relatively high standard deviation in propagation velocities, such as the refracted shock, the initial upstream bubble surface and the jet, show a greater difference among the experimental and numerical results.

In order to illustrate the effects of the uncertainty in initial bubble density on the locations of different flow structures in the entire SBI process, we plot the results of the statistics in the $x - t$ diagram (Fig.3.17). The solid lines show the mean locations of different flow structures, computed by

$$x = \bar{v}t + c, \tag{3.20}$$

where $\bar{v}$ stands for mean propagation velocities of different structures obtained from the calculation of statistical quantities, and c the start points for the structures. It should be noted that the start point c is reset when a structure transits to another. E.g., the retracted wave transits to the transmitted wave when it passes through the downstream bubble wall. The dash lines in Fig. 3.17 indicate the deviation respect to the mean

Table 3.5: Same as Table 3.4, but for the converging case (R22 bubble)

Velocity	start time [μs]	end time [μs]
v_{r}	0	120
v_{t}	t_{t}	t_{t}+48
$v_{\mathrm{u}i}$	0	400
$v_{\mathrm{u}f}$	400	1000
$v_{\mathrm{d}i}$	t_{t}	t_{t}+200
$v_{\mathrm{d}f}$	t_{t}+200	1000

location, which is computed by

$$x = (\bar{v} \pm 3\sigma(v))\, t + c. \tag{3.21}$$

It is observed that the large deviation in the refracted wave velocity causes a large uncertainty in its location. However, when it moves through the downstream bubble wall and becomes a transmitted wave, the magnitude of uncertainty remains almost unchanged due to the small deviation in the velocity of the transmitted wave (0.3%).

Converging case (R22 bubble)

The velocity of each structure and its statistics are given in Table 3.7. The numerical results of the deterministic simulation are quite similar to other existing simulations[25,45,55] and experimental results[16].

The mean velocities from the statistics are very close to the deterministic results (with a discrepancy less than 0.6%). The uncertainty affects the refracted shock more significantly (4.6%) than the transmitted shock (1.7%). With less deformation in shape compared to the diverging case, the uncertainty effects on the bubble surface motion for the both the upstream and downstream sides during the early stage of the interference are large, i.e. 4.0% for the upstream wall and 5.6% for the downstream wall. However, these effects become weaker in the second half of the process, where the corresponding standard deviations in velocities are 2.1% for the upstream wall and 1.6% for the downstream wall. Consistently, the structures with high standard deviations, such as the refracted shock,

Table 3.6: Velocities in diverging case. v stands for the velocities of deterministic simulation, $\bar{v}$ the mean velocities, and $\sigma(v)$ the standard deviations of velocities from the simulation statistics. The subscripts represent different flow structures, see the text for details

	v_{r}	v_{t}	v_{ui}	v_{uf}	v_{di}	v_{j}
Ref.[16]	900	393	170	230	-	146
Ref.[45]	943	377	178	227	-	145
Ref.[31]	943	373	176	229	-	153
v	951	374	180	218	102	149
$\bar{v}$	953	374	180	218	98.4	149
$\sigma(v)$	44	1.2	4.2	5.9	3.0	0.53
$\sigma(v)/\bar{v}$ (%)	4.6	0.3	2.3	2.7	3.0	0.4

upstream and downstream bubble surfaces during the early stage exhibit more diverse results among the existing literature. In comparison with the Helium bubble case, the overall effect of the uncertainty looks more significant with a broader deviation region. It should be noted that because the uncertainty is imposed in terms of the ratio of density, the magnitude of the uncertainty in the R22-bubble case is much larger than that of the Helium-bubble case.

Analogous to the previous case, we compute the mean and deviation of the location for each flow structure by (3.20) and (3.21) and plot them in an $x-t$ diagram for the R22-bubble case (Fig. 3.18), which quantifies the uncertainties in the position of different flow structures in the entire SBI process.

3.6 Summary

In this research, we evaluated uncertainty of a density uncertainty for the SFI[16] and SBI[16]. For SFI and SBI, four characteristic SFI structure and both diverging and converging cases (i.e., light and heavy bubbles) were investigated.

Every case in SFI and SBI is assumed to have 10% uncertainty in the density of the

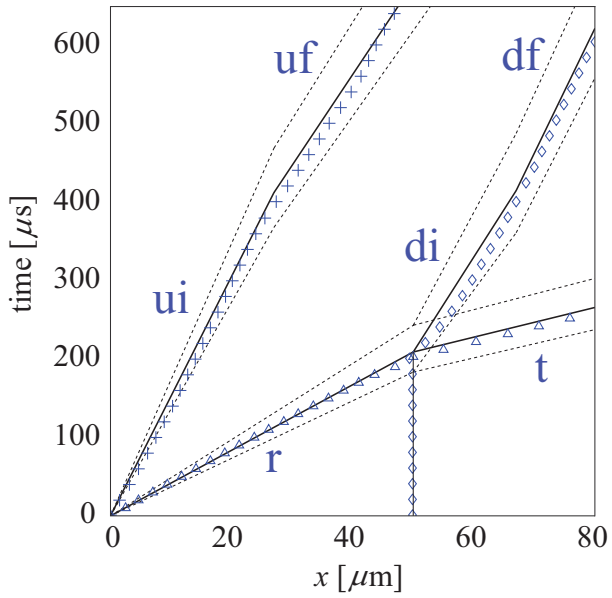

Fig.3.18: Same as Fig. 3.17, but for the converging case (R22 bubble) where the downstream bubble surface in the later stage (denoted by "df") does not coincide with the upstream bubble surface

Table 3.7: Same as Table 3.6, but for the converging case (R22 bubble) where the downstream bubble surface in the later stage (denoted by "df") does not coincide with the upstream bubble surface.

	v_{r}	v_{t}	v_{ui}	v_{uf}	v_{di}	v_{df}
Ref.[16]	240	540	73	90	78	78
Ref.[45]	254	560	74	90	116	82
Ref.[25]	243	525	65	86	85	64
Ref.[55]	244	538	65	86	87	64
v	238	528	65.2	86.2	78.6	62.9
$\bar{v}$	239	528	65.4	86.3	77.3	62.8
$\sigma(v)$	11	8.7	2.6	1.8	4.3	1.0
$\sigma(v)/\bar{v}$ (%)	4.6	1.7	4.0	2.1	5.6	1.6

contaminated media, of which effects on the interaction structure are evaluated using the pseudospectral collocation method[74]. For each SFI or SBI simulation, we used a numerical solver for multi-phase flow with a moving interface based on MUSCL[67] and THINC reconstructions[55], which solves the five-equation model developed by Allaire[2]. The number of SFI and SBI simulations used for each pseudospectral collocation evaluation is 17, which is well validated through the convergence study for SBI case shown in Appendix A.

First, we discussed the effects of the initial density uncertainty on the propagation of discontinuities and deformation of the interface based on the time developments of density and pressure fields.

For SFI, we identified two characteristic effects that are common between cases as follows: 1)The incident shock that is identified as a density or pressure discontinuity propagating outside the bubble is not significantly affected. 2) By contrast, the refracted shock that propagates inside the bubble exhibits a thick, high standard deviation area in both pressure and density fields, and thus it is strongly affected by the bubble-density uncertainty.

On the other hand, we also identified the differences between the SFI cases as follows: 1) The effect of the initial density uncertainty on the interaction structure changed with the existence of the precursor. 2)In case of the precursor develops, the effect of the initial density uncertainty transferred over interface via the precursor position. Because precursor is the point where the transmitted shock propagating contaminated media interacts the other side of the interface, this transfer of the effect of uncertainty is considered reasonable. The notable point is that whether the reflected shock is affected by the uncertainty or not could be used for classifying irregular structures with the regular refraction - reflection structures.

Another significant finding is that in every case, there are low-density-variance regions that are localized behind shock structure. For irregular refraction cases, the low-density-variance regions are connected at the foot of incident shock. In the shock side of the region, the density uncertainty decreases pressure, and in the interface side, the density uncertainty increases the pressure of the media. This change of effect direction could be understood with the concept of refracted index and acoustic impedance. The interface side is where the transmitted shock is generated from the refraction of the incident shock of

high impedance area and uncertain impedance area. On the other hand, the transmitted shock refracted outside of interface from uncertain media, where the effect of uncertainty react with the inverse side.

In the last part of SFI, the validity of the uncertainty quantification result was discussed using the experimental results of reference. Simulation results and tendency predicted with uncertainty quantification were compared with the experimental results. The simulation result agreed with the experimental result which support validity of the analyzed results. Moreover, the distribution tendency of the experimental result were in agreement with the uncertainty quantification results.

For SBI, we identified three characteristic effects that are common between the diverging and converging cases as follows: 1) The incident shock that is identified as a density or pressure discontinuity propagating outside the bubble is not significantly affected. 2) By contrast, the refracted shock that propagates inside the bubble exhibits a thick, high standard deviation area in both pressure and density fields, and thus it is strongly affected by the bubble-density uncertainty. 3) The shape of the deformed surface is strongly dependent on the bubble-density uncertainty, especially for the diverging case, where the standard deviation of the VOF function becomes high and localized along the bubble surface.

On the other hand, we also identified the differences between the diverging and converging cases as follows: 1) In the propagation of the transmitted shock, the standard deviation of both density and pressure distributions becomes high in the converging case, while that in the diverging case does not. 2) In the propagation of the side and modified shocks that emerge only in the diverging case, the side shock is strongly affected by the bubble-density uncertainty, while the modified shock is not. 3) The diffracted shock that appears in the converging case is not largely dependent on the bubble-density uncertainty.

Another significant finding is that in both diverging and converging cases, there are low-density-variance regions that are localized on the bubble surface and symmetrically distributed with respect to the symmetric plane. These regions also correspond to the location where the standard deviation of the VOF function becomes locally small, which indicates that the location of the bubble surface is stable, irrespective of the initial uncertainty inside the bubble. Furthermore, these areas would correspond to the vortex

generation area, from which the vortex is released in the later stage of the simulation. More detailed analysis of the relation between the low-density variation and the vortex generation is left to future study.

Finally, we also successfully evaluated the effects of the uncertainty on the velocities of shocks and bubble surface by identifying the mean and standard variation of the shock velocity. In both cases, the velocities of different waves/fronts exhibit a large difference in response to the bubble density uncertainty, which is in accordance with the existing experimental and numerical studies. The mean velocities are little different from the deterministic solutions, and thus, the effects of the uncertainty on each velocity are discussed mainly from their standard deviations. It is commonly observed in both converging and diverging cases that the refracted shock shows a high standard deviation, whereas the transmitted shock does not. This implicates that even if the bubble-density uncertainty directly affects the shock inside the bubble and has little effects outside the bubble, the entire structure of the SBI can be drastically changed.

Chapter 4

Uncertianty quantification of the multiscale wind forecast model

4.1 Multi-scale wind speed analysis model for wind forecast

4.1.1 introduction of wind forecast

The growing demand for renewable energy together with social, economical and environmental constraints leads to the currently continuous development of wind power. For the sake of integrating the wind power into an existing electrical network system, active control of the output wind power is of particular importance, which relies on the prediction of the hub-height wind for the target wind farm. To this end, numerical weather prediction (NWP) models (e.g., Weather Research and Forecasting (WRF) model), which integrate fluid dynamic cores and other parameterization packages of different physical processes, such as atmospheric boundary layer turbulent closures, radiation, moist convection physics, and other physics, have been extensively used to provide reliable predictions of low-level wind[6,58]. However, these NWP models cannot take the fine terrain features into account due to the relatively lower spatial resolution. It is addressed in Zajaczkowski et al.[80] that a typical mesoscale NWP model is not able to adequately capture the wind flow features finer than 1 km, which usually associate with complex topography. So, it is necessary to couple the NWP models with other high-resolution models to revolve the

local fine structures of the wind field over complex terrain regions.

Computational fluid dynamics (CFD) models, which enable to capture flow structures of small scale, are increasingly employed in simulating and predicting wind flow under complex conditions. Existing works[5,35,42] reveal that CFD models can directly simulate the dynamic effect of complex terrain on the low-level wind field, and thus provide more reliable numerical results. However, most of these studies are based on idealized and controlled boundary conditions, which are not able to provide the in situ configurations for real-case applications, especially for short-term wind forecasting where the weather condition varies significantly.

Some reports in the literature have adopted CFD models with real boundary conditions given by mesoscale models to study the flow and pollutant dispersion in built-up areas[33,34,69,71]. More recently, Temel et al.[62] proposed a new planetary boundary layer (PBL) parameterization scheme for the purpose of coupling models with different scales to simulate the complex wind flows. Though those results suggest that combining mesoscale WRF with microscale CFD model is an effective way that can be used for studying and predicting urban flow and dispersions in densely built-up areas as well as wind forecasting over complex terrains, several challenges arise meanwhile due to the relatively large differences between two kinds of models which may lead to difficulties in setting the initial/boundary condition and choosing turbulence model for CFD model[12,13]. In other words, there are many uncertainties involved in the coupled model which largely affect simulation results. García-Sánchez and Gorlé[12] have used an uncertainty quantification (UQ) method to quantify such uncertainties in simulating wind flow over Askervein hill region and Oklahoma city with a prescribed dominant wind direction, and show the necessity to assess quantitatively the temporal and spatial sensitivity of the model output to an uncertainty in initial/boundary condition or model parameters.

The first purpose of this paper is to develop a coupled model which consists of a mesoscale NWP model and a microscale CFD model, to improve the short-term forecasts of hub-height wind for a wind farm of interest in Japan. The CFD model adopted is the open-source package, OpenFOAM (Open Source Field Operation and Manipulation), while the WRF model is used as the mesoscale NWP model. We have evaluated the capability of the coupled forecasting system for short-term wind power forecasting, which

shows its great potential as a practical forecasting system for Japan area, where the geographic features are very complex compared to other places in the world. It is recognized that uncertainties as aforementioned exist in the coupled forecasting system. Thus, our second objective is to use the polynomial chaos expansion approach to quantify the uncertainties in both initial/boundary condition and the Reynolds-averaged Navier-Stokes (RANS) turbulence model in OpenFOAM, so as to clarify the most influential factors that affect the prediction of the low-level wind.

The remainder of this study is arranged as follows. In section 2, the data set, WRF model configuration, a brief introduction of OpenFOAM and the coupling procedure in this work are presented. The polynomial chaos expansion method used for uncertainty quantification and its implementation to the present coupled system are described in section 3. We present and discuss the capability of the coupled model and the UQ results on some representative uncertainties in the forecasting system in section 4, and end the paper with concluding remarks in section 5. The contents of this chapter are reported as reviewed paper[21].

4.1.2 WRF-OpenFoam coupled model

4.2 Data and Models

4.2.1 GFS Data and Observations

The National Centers for Environmental Prediction (NCEP) Global Forecast System (GFS) real-time forecasts which are gridded to a horizontal resolution of 0.25×0.25 degree are adopted as the initial/boundary conditions to drive the high-resolution mesoscale WRF model. The observed wind data are taken from 15-site (as shown in Figure 4.1(c)) at a wind farm located in south Awaji Island, Japan. These data have been processed through a quality-controlled procedure.

4.2.2 Mesoscale Model

The Advanced Research WRF (ARW) model version 3.6, a limited-area mesoscale model based on a fully compressible and non-hydrostatic dynamic core, is used in this study. The domain configuration of the WRF model is the same as in our previous study[8], including a parent domain and three nested domains with horizontal resolutions of 24.0 km, 6.0 km, 1.5 km, and 0.5 km, respectively. There are 35 vertically stretched eta levels, 10 of which are within the lowest 1 km used for all domains and the top level is located at 50 hPa. The topographic data are obtained from the U.S. Geological Survey (USGS) global 30 arc-s elevation (GTOPO30) data set for all domains. The 30-hour ahead hourly predictions are carried out, starting at 18:00 UTC of each day. The first 6 hours are considered as the spin-up time, and only the latter 24-hour forecasts are of interest.

4.2.3 CFD Model

The local microscale air motion is considered as incompressible turbulent flow. We use the reduced Reynolds-averaged Navier-Stokes (RANS) equations which are time-averaged equations of flow motion, to formulate the air flow,

$$\frac{\partial \overline{u_k}}{\partial x_k} = 0 \tag{4.1}$$

$$\rho \overline{u_j} \frac{\partial \overline{u_i}}{\partial x_j} = -\frac{\partial \overline{p}}{\partial x_i} + \frac{\partial}{\partial x_j}\left[\mu\left(\frac{\partial \overline{u_i}}{\partial x_j} + \frac{\partial \overline{u_j}}{\partial x_i}\right)\right] - \frac{\partial}{\partial x_j}\rho\overline{u_i' u_j'} \tag{4.2}$$

where ($^-$) denote the Reynolds-averaged quantity, μ is the dynamic viscosity, ρ is the density of dry air and $\overline{p}$ represents the pressure. The left hand side of (4.2) represents the change in mean momentum of fluid element owing to the unsteadiness and convection in the mean flow. The last term in (4.2) denotes the effect of sub-grid turbulent eddies owing to the fluctuating velocity field, which need an extra model for closure.

As a kind of turbulent viscous model, a RANS model adds the turbulent viscosity μ_t to the dynamic viscosity in (4.2). We in present work employ the widely used $k-\epsilon$ model

presented in[27], where the turbulent viscosity is computed by

$$\mu_t = C_\mu \frac{k^2}{\epsilon} \tag{4.3}$$

where C_μ is a model constant, $k = \frac{1}{2}(\overline{u'^2} + \overline{v'^2} + \overline{w'^2})$ stands for the turbulent kinetic energy and ϵ is the dispassion rate. The value of k and ϵ can be obtained using the following two equations,

$$\rho \frac{\partial(u_j k)}{\partial x_j} = \mu_t \frac{\partial u_i}{\partial x_j}(\frac{\partial u_i}{\partial x_j} + \frac{\partial u_j}{\partial x_i}) + \frac{\partial}{\partial x_j}\left[(\frac{\mu_t}{\sigma_k})\frac{\partial k}{\partial x_j}\right] - \rho\epsilon \tag{4.4}$$

$$\rho \frac{\partial(u_j \epsilon)}{\partial x_j} = C_{\epsilon 1}\frac{\epsilon}{k}\mu_t \frac{\partial u_i}{\partial x_j}(\frac{\partial u_i}{\partial x_j} + \frac{\partial u_j}{\partial x_i}) + \frac{\partial}{\partial x_j}\left[(\frac{\mu_t}{\sigma_k})\frac{\partial \epsilon}{\partial x_j}\right] - \rho C_{\epsilon 2}\frac{\epsilon^2}{k} \tag{4.5}$$

where $C_{\epsilon 1}$ and $C_{\epsilon 2}$ are two additional model constants, computed by

$$C_{\epsilon 1} = C_{\epsilon 2} - \frac{\kappa^2}{\sqrt{C_\mu}\sigma_\epsilon} \tag{4.6}$$

where $C_\mu = (\frac{u_*^2}{k})^2$ and u_* is the friction velocity. σ_ϵ and σ_k are other two model constants. The values of these model constants are usually obtained empirically and subject to tuning to fit specific applications. Standard set values of the model constants are given in Table 4.1. We in this paper assess the impact of the uncertainties in these empirical constants on the low-level wind structures over the target region.

Table 4.1: A set of typical coefficients of the $k-\epsilon$ model.[32]

Coefficient	κ	C_μ	σ_k	σ_ϵ	$C_{\epsilon 1}$	$C_{\epsilon 2}$
Standard	0.4	0.09	1.00	1.30	1.44	1.92

In this work, we use the SimpleFoam module in OpenFOAM model (ver.5) with the above RANS model to simulate the microscale low-level wind field in the wind farm site.

4.2.4 Coupling WRF and OpenFOAM

The two models mentioned above have been extensively verified and validated separately as mesoscale NWP model and microscale CFD model. However, it is hard to solely use

either of them to reproduce adequate numerical results for the wind flow over complex terrain for an in-situ operation in a target wind farm site. It is the main reason why we intend to couple these two component models together.

In practice, the coupling is implemented by using the mesoscale WRF forecasts as the boundary conditions and the initial guess to iterate the microscale OpenFOAM model at each time step. Given the output of WRF model, SimpleFOAM was driven to reach the steady solution under the instantaneous boundary forcing of the WRF model.

Figure 4.1 displays the configuration of WRF and OpenFOAM domains, where the grid spacing and domain size of the WRF and OpenFOAM models are quite different. The WRF domain shown here (Figure 4.1(a)) is the inner most one among the four-nested domains as described in section 4.2.2, of which the horizontal resolution is 500×500 m. Whilst, the horizontal resolution of the OpenFOAM domain (Figure 4.1(b)) is chosen as 50 m in this study, which is much finer than WRF model. The size of the OpenFOAM domain is 12 $km \times 12$ km which overlaps a region of 24×24 cells of the WRF model. This configuration is beneficial to extract information from WRF model as initial/boundary conditions to drive the OpenFOAM model. We illustrate part of the terrain and mesh for the wind farm site of interest in Figure 4.1(c), where the finest structured mesh cells are generated with the terrain data extracted from the Shuttle Radar Topography Mission (SRTM) data set that has a resolution of approximately 90 m (3 arc-seconds). Since OpenFOAM uses the Cartesian coordinate system, the coordinates are changed from Geographic to the UTM (Universal Transverse Mercator) coordinate based on the datum and zone of WGS 84 and 53 N respectively.

A structured mesh with hexahedral elements is generated. The lowest surfaces of the mesh elements are fitted to the terrain surface, so as to represent the topographic features accurately. Horizontally, the total number of the mesh is 240 × 240, while 30 levels are partitioned in the vertical with an expansion ratio of 1.94. The boundary condition types used in the numerical experiment are summarized in Table 4.2.

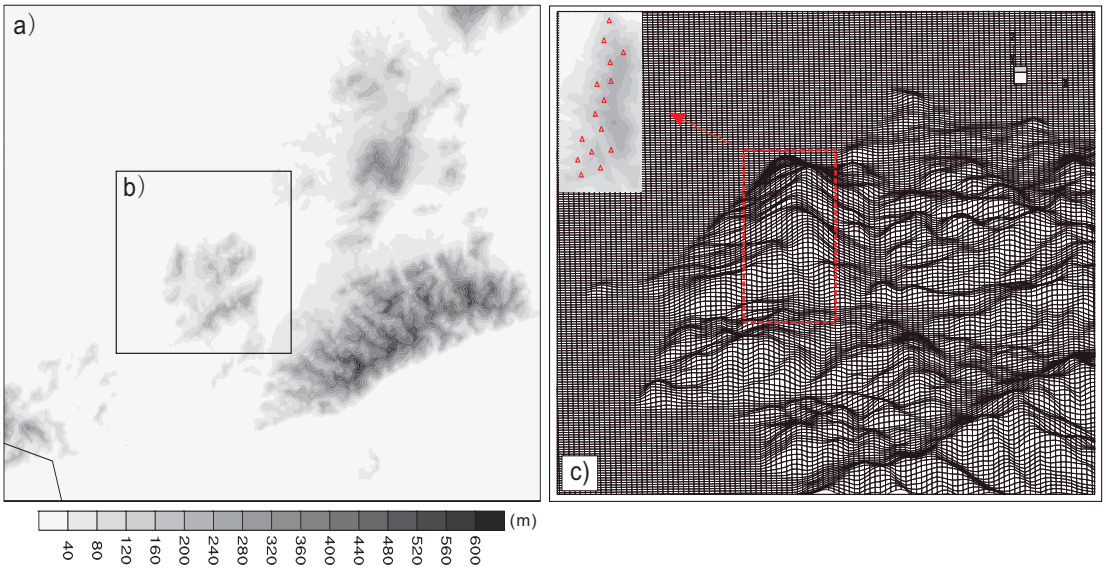

Fig.4.1: The configuration of inner most WRF domain (a) and the OpenFOAM domain (b). The gray shaded indicates the terrain height. An enlarged part of the mesh structure of OpenFOAM domain is displayed in (c), where the wind farm of interest is included. The red triangles stand for the specific position of 15 turbine sites.

Table 4.2: The boundary condition types used for OpenFOAM model in the study.

Boundary	U	p	k	epsilon
inlet_patch	fixedValue	zeroGradient	fixedValue	fixedValue
outlet_patch	inletOutlet	fixedValue	zeroGradient	zeroGradient
ground_patch	fixedValue	zeroGradient	kqRWallFunction	epsilonWallFunction

4.2.5 Running mean correction

The running mean correction method has the ability of improving the raw predictions by reducing the systematic error[17,57]. In practice, running mean errors are calculated with averaging windows varying from 1 to 30 days, and those error estimates are used to forecast and correct the subsequent predictions[17]. We choose the running mean method

with the averaging window of one-day as a reference to compare the performance of the coupled model proposed in this work.

4.3 Uncertainty in the coupled model

Although coupling mesoscale WRF and microscale CFD model can improve wind forecasts over a complex region, the performance of this coupled model includes several uncertainty sources which significantly affect the forecasting results, such as the uncertainties in the lateral coupling boundary condition, the turbulent model, and the land surface parameterization, among others.

In this study, we focus on the uncertainties in inlet boundary conditions and the RANS turbulence model ($k-\epsilon$) in the CFD module.

- *Uncertainty in the inlet boundary condition*

  The wind flow inlet boundary condition, which usually has the form of standard neutral surface layer profile[48], can significantly influence the output of a CFD model. Such a profile can be specified using the wind shear exponent α with the wind velocity at a reference level[58],

$$U(z) = U_{ref}\Big(\frac{z}{z_{ref}}\Big)^{\alpha} \tag{4.7}$$

  where $U(z)$ and U_{ref} are the wind velocities at height z and reference level z_{ref}, respectively. The empirically estimated value of α is approximately 0.14 over smooth terrains[58], which however needs further tuning when applied to complex terrain conditions. Thus, we choose the shear exponent α as an uncertain parameter to quantify the impact of the uncertainty in the inlet boundary condition on the numerical results of the low-level flow field. We analyzed the statistics from a set of deterministic CFD simulations with different values of α. For the sake of investigating the sensitivity of α, a broad range varying according to a uniform distribution in the range from 0.02 (very smooth surface) to 0.26 (suburban)[47] is employed in this study.

- *Uncertainties in turbulence model parameters*

  We also quantified the impact of the uncertainty of the empirical parameters in the turbulence model as described in Table 4.1 on the wind flow forecasting at the target wind farm over complex terrain conditions.

  We set the uncertainty of each parameter as a uniform distribution with bounded values shown in Table 4.3. The variation range of each parameter is determined by the physical and computational admissible bounds with respect to the standard values as discussed in[10].

Table 4.3: Admissible range of the parameters in $k-\epsilon$ turbulence model.

Parameter	Low bound	Upper bound
$C_{\epsilon 2}$	1.248	2.88
C_{μ}	0.054	0.135
σ_k	0.6	1.5
σ_{ϵ}	0.78	1.95

4.4 Uncertainty quantification of the WRF-OpenFoam integration model

In this section, we first evaluate the capability of the coupled system by simulating an in-situ case. The numerical results of the prediction of the coupled model are validated with the nacelle wind observations at each wind turbine site over an 8-day period. We then quantify the impact of the uncertainties in both the parameters in the turbulence model and the inlet boundary conditions which are extracted from the mesoscale WRF model and serves the key in the coupled model.

4.4.1 The flow field under dynamic forcing of topography

An in-situ case starting from 00:00 UTC 01 October, 2013, has been used to validate the performance of the coupled forecasting system for simulating low-level wind flow over

complex terrain. As the prevailing wind is northwest, the inlet and outlet boundary conditions are set as in Figure 4.2. The inlet boundary condition is the output from mesoscale WRF model. The SimpleFoam module in the OpenFOAM package with the $k-\epsilon$ turbulence model is used to generate a steady flow field. Throughout all this study, we assume that the wind flow reaches a steady state when all the residuals of U_x, U_y, U_z and k are smaller than 10^{-3}, while the residual of p should be smaller than 10^{-2}.

Figure 4.2(a) and Figure 4.2(b) show the simulation results of pressure and wind speed respectively. The distribution of the pressure is reasonably reproduced, where the dynamic forcing of the topography results in low pressure near the top of the hills and high pressure in the upwind side of the hills. The pressure fields sliced on the two vertical cross sections in $x-z$ plane in Figure 4.2(a) demonstrate that the coupled model is able to simulate the fine 3D flow structures over complex terrain. From Figure 4.2(b), it is observed that the wind velocity over the hills is significantly accelerated and reaches the maximum around the top of the hills, while decreased on the lee side of the hills. In addition, we have also examined the turbulence kinetic energy (TKE) and found that TKE is greatly enhanced over the hills and decays out gradually in the downstream direction, which is in agreement with the theoretical observational results.

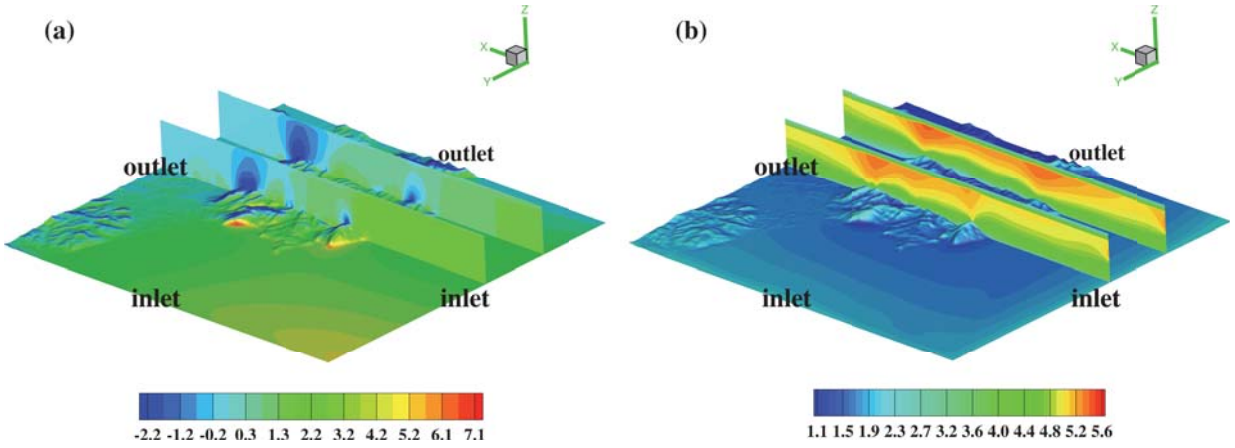

Fig.4.2: The distributions of the pressure (a) and the wind velocity (b) at 00:00 UTC 01 October, 2013, over the target area where the x and y represent the east and north directions, respectively. Two vertical cross sections are also included to provide 3D images. Dominant wind direction is northwestern.

4.4.2 Validation of the coupled model for wind prediction

It has been demonstrated in the above section that the coupled system with the direct CFD simulation of topographic forcing the wind flow over the complex terrain can be well resolved. We extensively carried out 192 cases using the coupled model to predict the wind fields of a one-hour interval from 00:00 UTC 02 October to 23:00 UTC 09 October, 2013. It is worthwhile to note that the wind directions from WRF-alone model for these cases are different. The inlet and outlet patches are determined by the prevail wind direction at level of 400-m. The forecasting results for 15 turbine sites are compared with the corresponding nacelle wind observations separately. In order to evaluate the effectiveness of the coupled forecasting system, we also include the numerical results from the forecasting system solely based on the mesoscale WRF model for comparison at some specific turbine sites of the target wind farm.

The comparisons of the wind speed predictions for all 15 wind turbine sites during the period of 00:00 UTC 02 October to 23:00 UTC 09 October, 2013 are shown in Figure 4.3 and Figure 4.4, where forecasts of both the WRF model (denoted by "WRF_fore") and the coupled model (denoted by "WRF+OpenFOAM") are plotted against the nacelle observations (denoted by "OBS"). It is found that although the accuracy of forecasts varies among the turbines and over different periods of time, both the WRF-alone forecasts and the WRF/OpenFOAM coupled forecasts can reproduce the overall wind speed variations reasonably well for all 15 turbines. It is also observed that the coupled WRF/OpenFOAM model can significantly improve the forecasting skill, particularly for the period from 120 to 150. In spite of different extents for different turbines and different periods of time, the coupled model shows appealing prediction capability in comparison with the raw WRF forecasts for all tested cases.

In order to quantitatively evaluate the improvement in the forecasting skill of the coupled WRF/OpenFOAM model compared to the WRF-alone forecasts, we calculated the mean errors (ME), root mean square errors (RMSE) and correlation coefficients (CC) of the raw WRF forecasts and the coupled WRF/OpenFOAM forecasts for all 15 turbines over the period of time tested. We plot all ME, RMSE and CC measurements, as well as

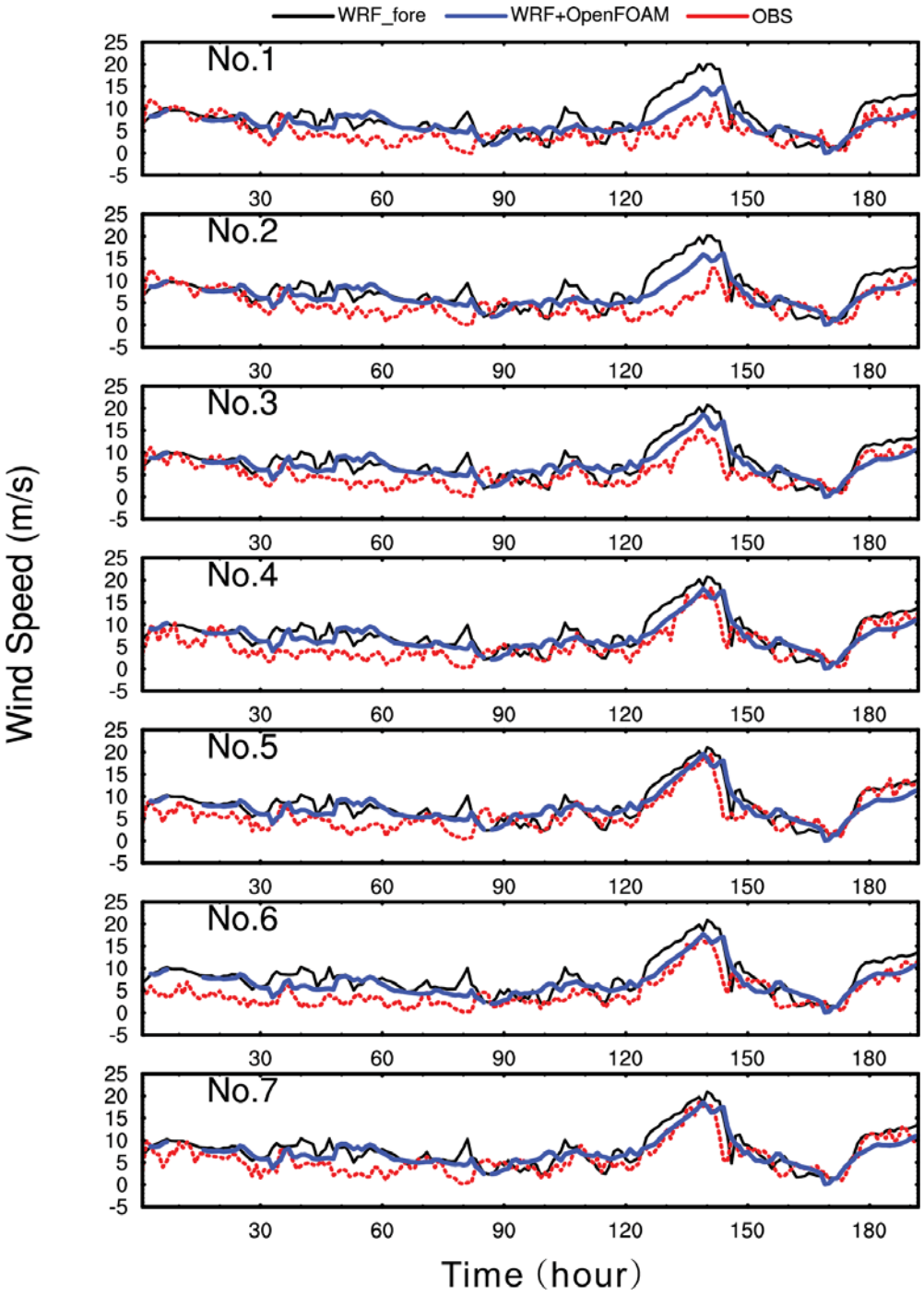

Fig.4.3: The WRF forecasts ("WRF_fore"), the predictions of the coupled system ("WRF+OpenFOAM") and the corresponding observations ("OBS") of 7 turbines for 192 cases, from 00:00 UTC 02 October to 23:00 UTC 09 October, 2013.

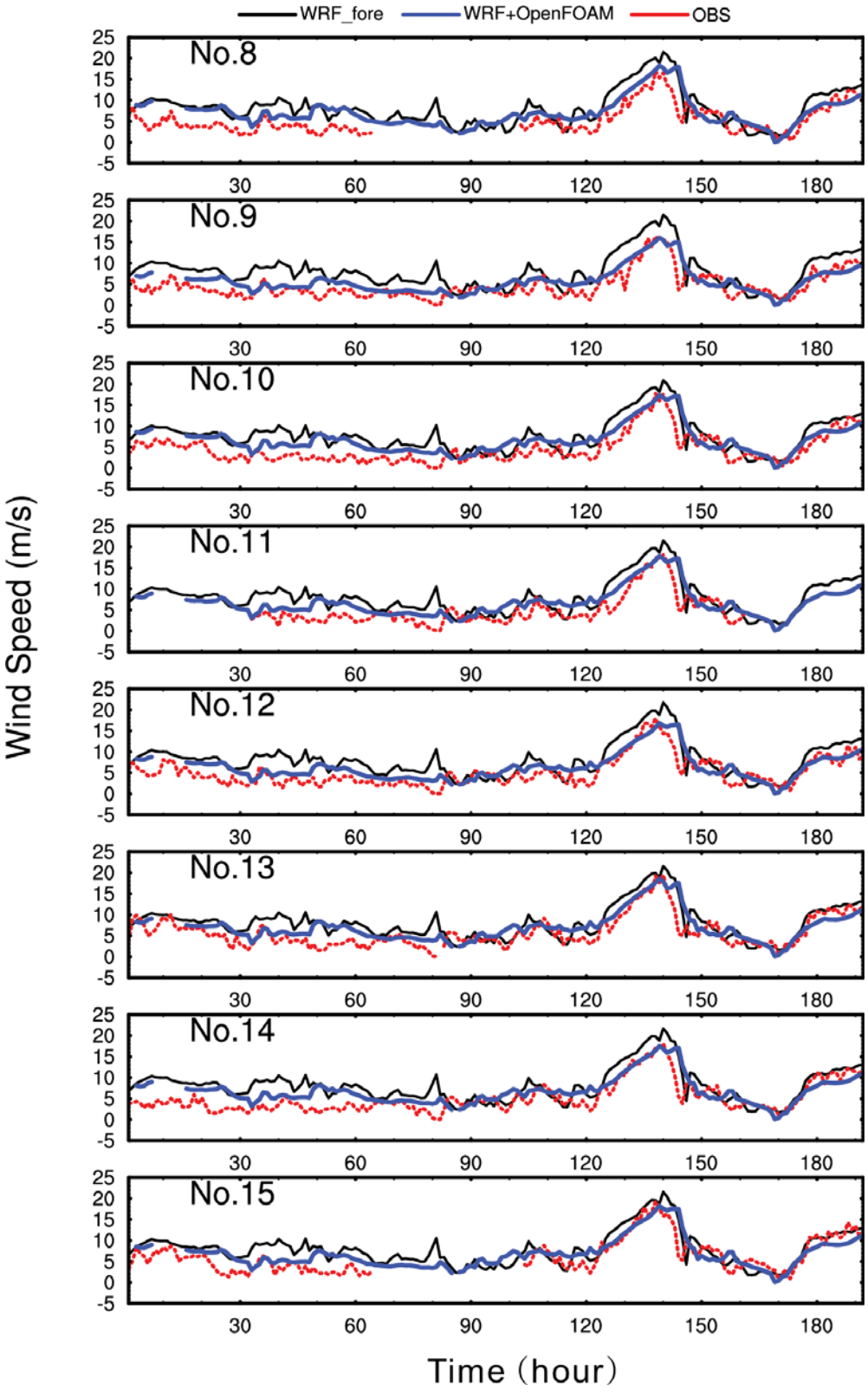

Fig.4.4: Same as the Figure 4.3, but for the turbines from No.8 to No.15.

the relative improvements due to the implementation of the coupled model in Figure 4.5. Additionally, the results of the running mean (RM hereafter) method are also included for comparison. As indicated by the red lines in Figure 4.5, the forecasts of the coupled model for all turbines are more accurate than the WRF model. For example, the coupled model improves the ME, RMSE, and CC of the WRF raw forecast for turbine No.9 by 59%, 43%, and 8%, respectively. From Figure 4.5, it also can be observed that RM method is able to improve the raw prediction of the WRF-alone model; particularly, the systematic bias has been largely reduced. When comparing the correction results of RM method and the coupled model, we see the apparent advantage of the WRF/OpenFOAM in reducing the forecasting errors. Moreover, the WRF/OpenFOAM shows much smaller RMSE and larger CC with respect to RM method. This may be due in part to the fact that the proposed WRF/OpenFOAM can not only improve the systematical errors in WRF-alone forecasts but also part of stochastic uncertainties, while the RM method has an effect barely on the systematic errors. Thus, it is concluded that coupling the mesoscale WRF model with the OpenFOAM CFD model is very effective to resolve the low-level wind field over complex topographic conditions, and thus significantly improve the prediction capability.

4.4.3 Results of uncertainty quantification

Impact of the uncertainties in the parameters of turbulence model and inlet wind profile parameter

As discussed in section 3.4, we quantify the uncertainties in the turbulence model and inlet wind profile of the CFD computation for microscope wind field, which are thought to be important for the numerical results of the coupled model.

We choose three cases with the WRF outputs at 00:00 UTC, 12:00 UTC and 23:00 UTC, 9 October, 2013 to drive the OpenFOAM CFD model for the numerical experiments on uncertainty quantification. We investigated the impact of uncertainties in five parameters, i.e. $C_{\epsilon 2}$, C_μ, σ_k and σ_ϵ in the turbulence model, and α in the inlet wind profile defined by (4.7).

The STD of the wind speed for the tested parameters at each wind turbine site are

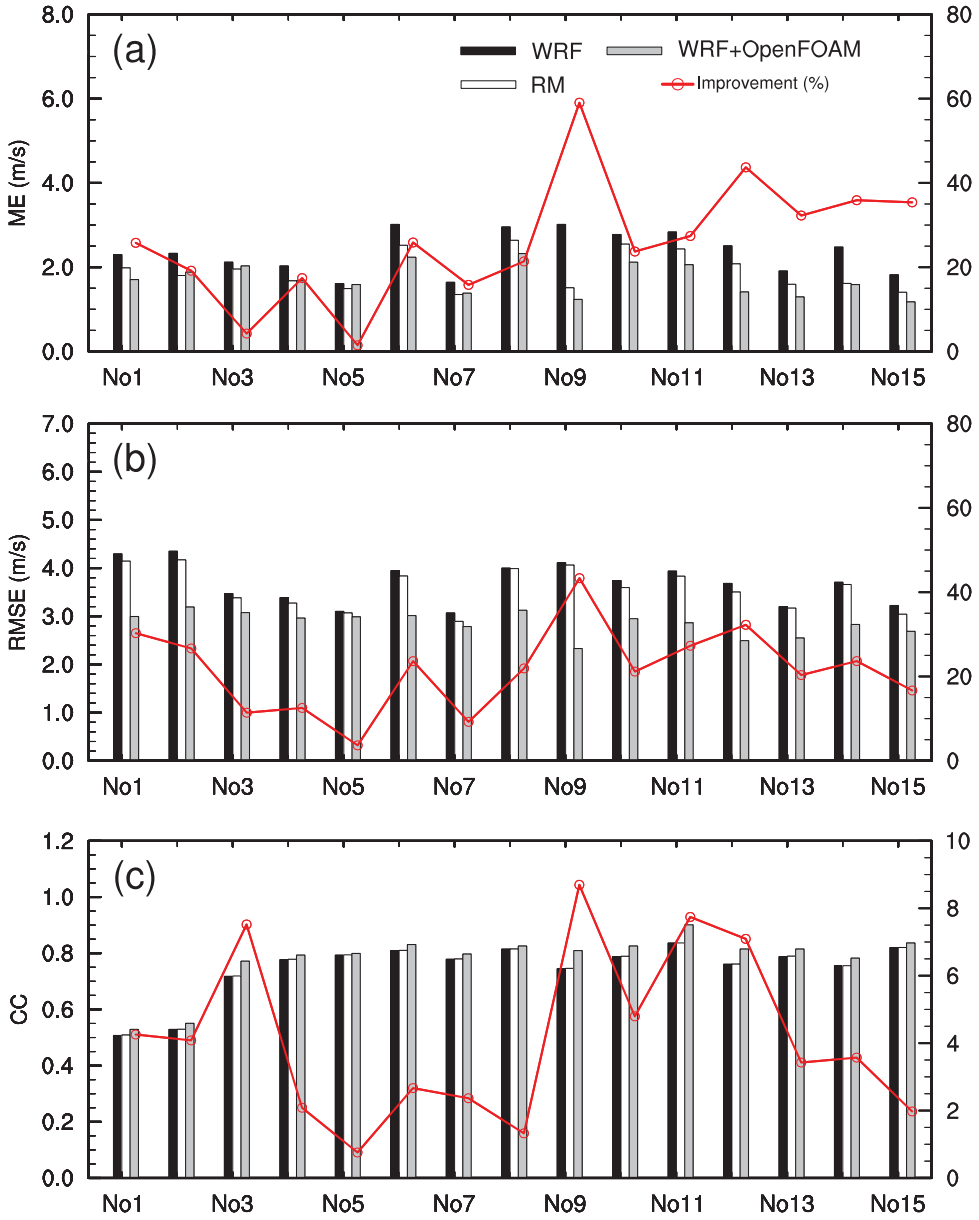

Fig.4.5: A comparison of ME (a), RMSE (b) and CC (c) of the WRF model (solid black bar), the running mean method (solid white bar) and the coupled model (solid gray bar) forecasts of wind speed for the 15 turbines of the Awaji-island wind farm in Japan. The red line stands for the relative improvement by WRF/OpenFOAM coupled model in comparison with the WRF-alone forecasts and the forecasts using running mean approach.

computed by the stochastic collocation method and summarized in Table 4.4. In addition, the deterministic forecasts of the hub height wind using the coupled model with standard values for all parameters are also displayed in Table 4.4, which are used to assess the relative sensitivity against the STD values.

Table 4.4: The STD values of the wind speed (m/s) for three cases at 15 turbine sites. The relative sensitivity (%) against the deterministic forecasts of the hub height wind is shown in parentheses.

	parameter	No.1	No.2	No.3	No.4	No.5	No.6	No.7	No.8	No.9	No.10	No.11	No.12	No.13	No.14	No.15
	α	1.211	1.277	1.323	1.368	1.338	1.222	1.289	1.282	1.021	1.171	1.140	1.076	1.162	1.114	1.093
		(7.94)	(7.96)	(8.52)	(8.33)	(8.32)	(7.85)	(8.18)	(7.97)	(8.31)	(7.67)	(7.61)	(7.30)	(7.71)	(7.39)	(7.18)
	$C_{\epsilon 2}$	0.125	0.130	0.206	0.153	0.114	0.157	0.119	0.087	0.117	0.069	0.060	0.113	0.117	0.139	0.043
		(0.82)	(0.81)	(1.33)	(0.93)	(0.71)	(1.01)	(0.76)	(0.54)	(0.95)	(0.45)	(0.40)	(0.77)	(0.78)	(0.92)	(0.28)
Case1	C_μ	0.178	0.189	0.181	0.175	0.156	0.191	0.154	0.144	0.168	0.127	0.168	0.127	0.173	0.178	0.147
		(1.17)	(1.18)	(1.17)	(1.07)	(0.97)	(1.23)	(0.98)	(0.90)	(1.37)	(0.83)	(1.12)	(0.86)	(1.15)	(1.18)	(0.97)
	σ_k	0.060	0.057	0.065	0.055	0.044	0.056	0.037	0.029	0.037	0.022	0.033	0.017	0.039	0.034	0.021
		(0.39)	(0.36)	(0.42)	(0.33)	(0.27)	(0.36)	(0.23)	(0.18)	(0.30)	(0.14)	(0.22)	(0.12)	(0.26)	(0.23)	(0.14)
	σ_ϵ	0.051	0.082	0.090	0.096	0.095	0.107	0.091	0.086	0.010	0.081	0.075	0.088	0.097	0.104	0.073
		(0.33)	(0.51)	(0.58)	(0.58)	(0.59)	(0.69)	(0.58)	(0.53)	**(0.08)**	(0.53)	(0.50)	(0.60)	(0.64)	(0.69)	(0.48)
	fore	15.26	16.04	15.52	16.42	16.08	15.56	15.76	16.08	12.29	15.27	14.99	14.74	15.07	15.08	15.22
	α	0.708	0.761	0.780	0.807	0.816	0.805	0.802	0.830	0.670	0.804	0.810	0.802	0.788	0.793	0.847
		(9.80)	(9.97)	(9.63)	(9.97)	(9.74)	(10.05)	(9.97)	(10.20)	(10.21)	(10.17)	(10.23)	**(10.31)**	(10.19)	(10.27)	(10.23)
	$C_{\epsilon 2}$	0.135	0.139	0.126	0.142	0.132	0.160	0.158	0.171	0.239	0.148	0.188	0.180	0.190	0.208	0.160
		(1.87)	(1.82)	(1.56)	(1.75)	(1.58)	(2.00)	(1.96)	(2.10)	(3.64)	(1.87)	(2.37)	(2.31)	(2.46)	(2.69)	(1.93)
Case2	C_μ	0.113	0.111	0.102	0.107	0.101	0.114	0.111	0.113	0.125	0.098	0.114	0.112	0.114	0.114	0.109
		(1.56)	(1.45)	(1.26)	(1.32)	(1.21)	(1.42)	(1.38)	(1.39)	(1.90)	(1.24)	(1.44)	(1.44)	(1.47)	(1.48)	(1.32)
	σ_k	0.052	0.053	0.058	0.059	0.064	0.055	0.060	0.054	0.028	0.049	0.050	0.041	0.045	0.048	0.039
		(0.72)	(0.69)	(0.72)	(0.73)	(0.76)	(0.69)	(0.75)	(0.66)	(0.43)	(0.62)	(0.63)	(0.53)	(0.58)	(0.62)	(0.47)
	σ_ϵ	0.072	0.073	0.067	0.075	0.071	0.078	0.078	0.081	0.090	0.069	0.081	0.080	0.078	0.083	0.080
		(1.00)	(0.96)	(0.83)	(0.93)	(0.85)	(0.97)	(0.97)	(0.99)	(1.37)	(0.87)	(1.02)	(1.03)	(1.01)	(1.08)	(0.97)
	fore	7.222	7.634	8.099	8.093	8.378	8.008	8.044	8.141	6.565	7.905	7.921	7.777	7.735	7.719	8.278
	α	0.203	0.217	0.226	0.228	0.233	0.224	0.219	0.220	0.154	0.209	0.189	0.184	0.200	0.178	0.187
		(8.26)	(8.48)	(8.68)	(8.59)	(8.85)	(8.92)	(8.80)	(8.84)	(8.48)	(8.96)	(8.77)	(8.96)	(8.88)	(8.52)	(8.90)
	$C_{\epsilon 2}$	0.136	0.125	0.112	0.112	0.103	0.104	0.108	0.104	0.065	0.099	0.094	0.095	0.084	0.045	0.104
		(5.53)	(4.89)	(4.30)	(4.22)	(3.91)	(4.14)	(4.34)	(4.18)	(3.58)	(4.25)	(4.36)	(4.63)	(3.73)	(2.15)	(4.95)
Case3	C_μ	0.032	0.028	0.026	0.024	0.021	0.027	0.025	0.031	0.039	0.029	0.032	0.033	0.041	0.038	0.030
		(1.30)	(1.09)	(1.00)	(0.90)	(0.80)	(1.08)	(1.00)	(1.25)	(2.15)	(1.24)	(1.49)	(1.61)	(1.82)	(1.82)	(1.43)
	σ_k	0.019	0.015	0.012	0.010	0.006	0.004	0.007	0.006	0.021	0.008	0.006	0.008	0.022	0.010	0.011
		(0.77)	(0.59)	(0.46)	(0.38)	(0.23)	(0.16)	(0.28)	(0.24)	(1.16)	(0.34)	(0.28)	(0.39)	(0.98)	(0.48)	(0.52)
	σ_ϵ	0.014	0.015	0.018	0.020	0.023	0.028	0.030	0.031	0.039	0.024	0.021	0.019	0.052	0.032	0.013
		(0.57)	(0.59)	(0.69)	(0.75)	(0.87)	(1.12)	(1.21)	(1.25)	(2.15)	(1.03)	(0.97)	(0.93)	(2.31)	(1.53)	(0.62)
	fore	2.458	2.558	2.604	2.655	2.634	2.510	2.488	2.489	1.815	2.332	2.154	2.054	2.251	2.090	2.102

Table 4.5: The STD values of the wind direction (°) for three cases at 15 turbine sites. The deterministic forecasts of hub height wind direction are also included.

	parameter	No.1	No.2	No.3	No.4	No.5	No.6	No.7	No.8	No.9	No.10	No.11	No.12	No.13	No.14	No.15
	α	1.033	0.963	1.099	0.963	1.104	0.942	1.098	0.960	1.381	0.914	1.089	1.026	1.160	1.086	0.973
	$C_{\epsilon 2}$	0.472	0.342	0.451	0.351	0.446	0.412	0.390	0.368	0.372	0.451	0.487	0.490	0.542	0.511	0.621
Case1	C_μ	1.024	0.950	1.013	0.876	0.941	0.856	0.995	0.884	1.411	0.841	0.954	0.998	0.976	0.978	0.886
	σ_k	0.497	0.384	0.426	0.327	0.319	0.283	0.328	0.268	0.510	0.234	0.250	0.252	0.256	0.247	0.206
	σ_ϵ	0.380	0.389	0.394	0.361	0.370	0.317	0.373	0.318	0.503	0.283	0.344	0.328	0.329	0.323	0.270
	fore	61.6	64.4	64.5	65.7	66.4	69.9	67.4	70.5	73.6	71.6	72.5	74.7	71.2	71.6	76.2
	α	1.280	1.132	1.186	1.094	1.112	0.931	1.082	0.938	0.964	0.906	0.922	0.864	0.990	0.972	0.842
	$C_{\epsilon 2}$	0.424	0.352	0.467	0.353	0.369	0.320	0.401	0.355	0.845	0.376	0.528	0.540	0.537	0.501	0.510
Case2	C_μ	0.230	0.174	0.091	0.097	0.071	0.069	0.106	0.108	0.424	0.148	0.272	0.299	0.244	0.297	0.295
	σ_k	0.482	0.429	0.339	0.374	0.330	0.297	0.283	0.244	0.123	0.218	0.119	0.112	0.122	0.117	0.109
	σ_ϵ	0.115	0.120	0.173	0.136	0.157	0.158	0.194	0.196	0.408	0.238	0.301	0.312	0.260	0.289	0.312
	fore	276.6	276.0	281.7	277.5	281.6	278.7	280.8	278.8	284.6	279.9	282.4	282.4	283.1	282.7	284.5
	α	1.090	1.007	1.206	1.029	1.165	0.820	0.994	0.757	0.431	0.701	0.635	0.511	0.725	0.572	0.544
	$C_{\epsilon 2}$	0.731	0.705	0.960	0.831	1.024	1.134	1.423	1.413	2.769	1.403	2.054	1.975	1.999	2.727	2.117
Case3	C_μ	0.443	0.400	0.542	0.435	0.516	0.563	0.696	0.677	1.301	0.605	0.925	0.842	0.907	1.191	0.988
	σ_k	0.881	0.830	0.759	0.715	0.702	0.404	0.418	0.178	0.440	0.177	0.345	0.440	0.170	0.414	0.509
	σ_ϵ	1.107	1.004	1.151	0.993	1.108	0.916	1.129	0.920	1.081	0.706	0.892	0.773	1.050	1.109	0.873
	fore	255.1	257.2	262.0	259.8	263.4	262.8	262.8	262.9	267.3	263.6	265.7	265.6	266.6	265.7	268.2

Table 4.4 reveals that the sensitivity of the predicted wind speed to different model parameters, reflected by the STD values, varies significantly among the different turbine sites. For example, case 2 and case 3 are more sensitive to the uncertainty in $C_{\epsilon 2}$ than that in C_μ, whereas the impact of the variation in C_μ is averagely more significant for all 15 turbine sites in case1. By examining the ratio of the STD value and the wind speed from the deterministic simulation, we can estimate the sensitivity of the corresponding parameter to the wind field forecasts as shown in the parentheses in Table 4.4. It is observed that different parameters have quite different impacts on wind speed forecast results. For example, parameter σ_ϵ caused the smallest impact of 0.08% on the wind speed in case1 at No.9 turbine site, whereas parameter α caused the most significant impact of 10.31% on the wind speed in case2 at No.12 turbine site. The impacts of five model parameters on wind direction are shown in Table 4.5. Compared to the case of

wind speed, relatively small differences of STD values among 15-turbine can be observed, which might indicate that the predicted wind direction is not sensitive to the uncertainties in the presented five uncertain parameters.

The most striking observation is that the variation in the inlet wind profile characterized by the parameter α (Table 4.4) which generates the STD values much more significant than any parameters in the turbulence model. It concludes that α in the inlet wind profile of the CFD OpenFOAM model in the coupled system affects dominantly on predicting low-level wind fields.

Statistic characteristics of the uncertainty in the inflow profile parameter α

As discussed above, the inlet wind profile plays a prominent role in predicting the wind field. We in this section discuss further the statistics of the wind speed prediction with the uncertainty in parameter α. Figure 4.6 shows the wind speed change with the wind profile parameter α for three cases at the sites of turbine No.1, No.3, No.9, and No.15, respectively. The markers indicate the 17 quadrature points in the stochastic collocation method adopted in this study, and the black lines stand for the reconstructed profiles using the results of the stochastic collocation method. It is found that the reconstructed wind variation with respect to parameter α can be accurately fitted by the basis functions with the coefficients determined from the stochastic collocation method. From the reconstructed profiles, the relationship between α and the wind speed of each turbine can be obtained. Using this reconstructed profile and the predetermined probability function of the uncertainty element $p(\xi)$ (a uniform distribution within $[-1, 1]$ in the present work), we can get the statistic properties of the predicted wind speed under the influence of uncertainty in α.

The CDF functions of the corresponding wind speed of the three cases at turbine No.1 site are depicted in Figure 4.7 as an example, where we also indicate the mean value location and the points Q1, Q2, and Q3 standing for the locations where the CDF value equals to 25%, 50%, and 75%, respectively. It is observed that in all cases the CDF functions are slightly curved, and the mean value point locates close to but does not coincide exactly with the 50% CDF point, which indicates a weak nonlinearity in the CFD prediction results with respect to the uncertainty in α.

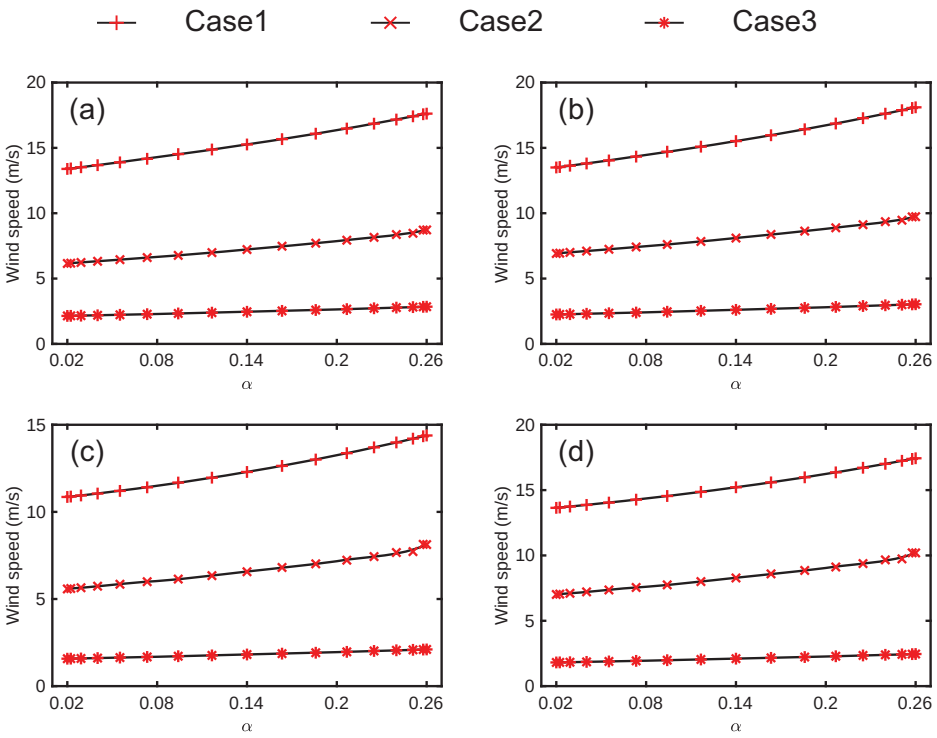

Fig.4.6: The quadrature points and reconstructed profiles on the stochastic domain for turbine No.1 (a), No.3 (b), No.9 (c), and No.15 (d). The black lines are the reconstructed profiles via the stochastic collocation method using the values at the quadrature points.

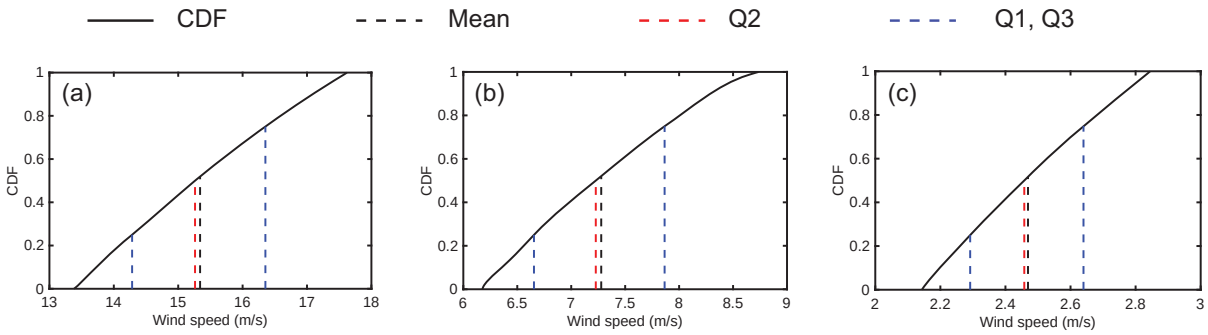

Fig.4.7: The CDFs of the wind speed at turbine No.1 site for case1 (a), case2 (b) and case3 (c). Mean value location is indicated by the black dotted line, and Q2 location (CDF value equals to 50%) by red dotted line. The left-most dotted blue line indicates the Q1 location (CDF value equals to 25%), while the right-most dotted blue line indicates the Q3 location (CDF value equals to 75%) respectively.

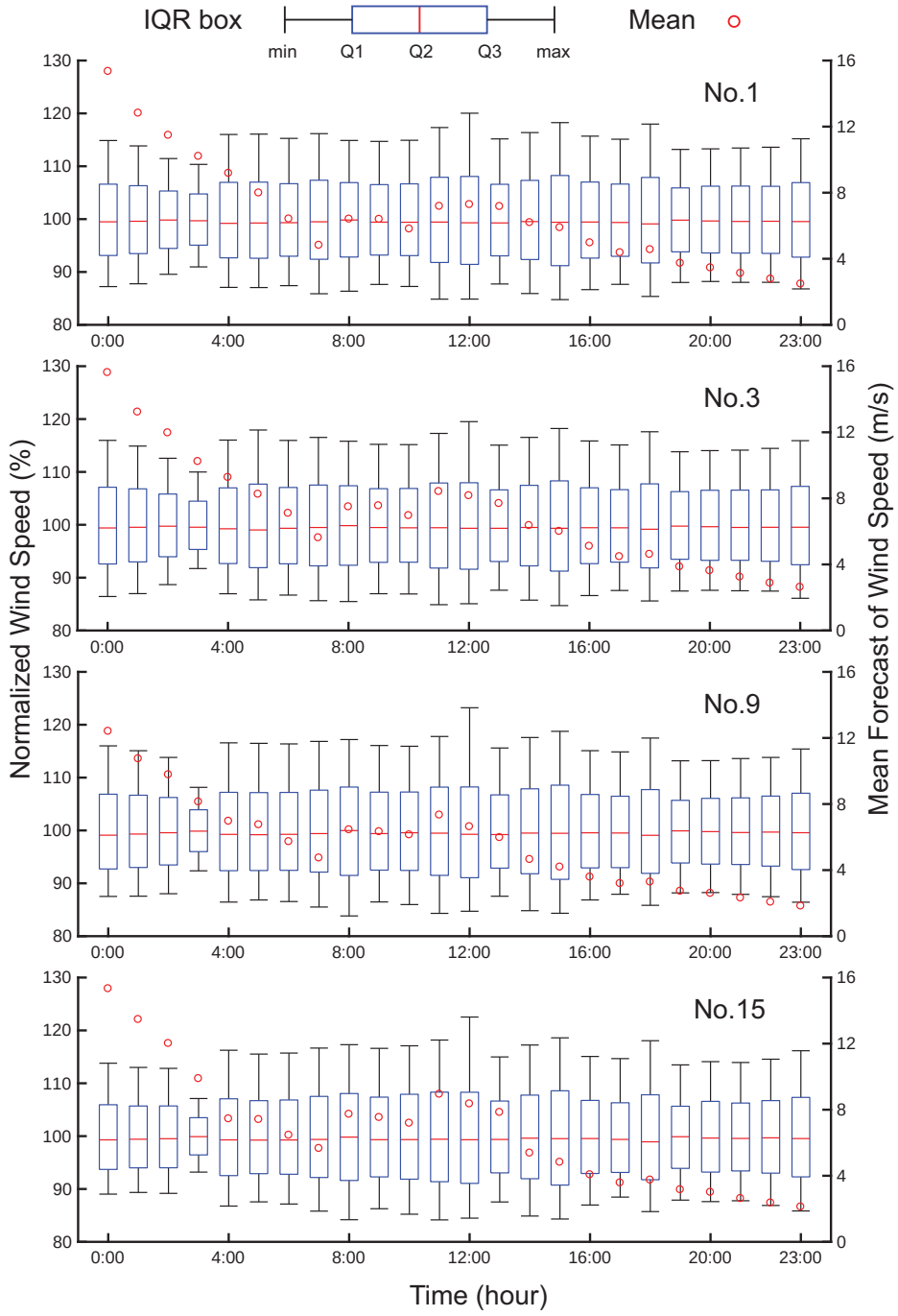

Fig.4.8: The IQR boxes of the wind speed normalized by the mean values (left axis) in regard to the uncertainty in α for four turbines at 24 instants from 00:00 UTC 9 October to 23:00 UTC 9 October, 2013. In each box, minimum, Q1, Q2, Q3, and maximum value stand for the CDF 0%, 25%, 50%, 75%, and 100% respectively. The red circles indicate mean values of the wind speed forecasts (right axis) for each time instant.

The effects of the uncertain parameter α for four wind turbines at 24 instants, hourly from 00:00 UTC 9 October to 23:00 UTC 9 October, 2013, are represented as the interquartile range IQR box and mean forecast of wind speed in Figure 4.8. The IQR values are based on the wind speed normalized with the mean values. It is notified that larger discrepancy between the wind forecasts of coupled model and observations is found during this period of time as shown in Figure 4.3.

Consistent with Figure 4.7, the difference between median and the mean wind speed is very small ($\leq$1.13%). Although the IQR box varies among the turbines at different instants, the effect of the change of α is overall significant. For example, at instant 15:00 the significant variation in the normalized wind speed of turbine No.15 site for Q1 point reaches 9.26%, while that for Q3 point is 8.58%. Note that this kind of effect is prominent no matter how small or large the mean of wind speed forecast is. This significance of parameter α in affecting the wind speed forecast implies a potential to use it as the parameter for data assimilation to improve the numerical results of the coupled model.

4.5 Summary

In this study, a coupled model consisting of mesoscale WRF model and microscale OpenFOAM CFD model has been proposed to predict the hub-height wind at a wind farm in Japan, where the terrain condition is very complex and generates large fluctuations in surface wind field. The predicted hub-height wind of the coupled model has been compared with the raw prediction of WRF model as well as the observation, for a real-case test from 00:00 UTC 1 October to 23:00 UTC 9 October, 2013. It is found that the coupled model is able to resolve more accurately the fine flow structures over the complex terrain. The numerical results show that the coupled model significantly ameliorates the hub-height wind forecasts in comparison with WRF-alone forecasts, with 26%, 22% and 4% improvements in the quantified metrics of ME, RMSE and CC, respectively.

In order to explore the possibility for further improvement, we have carried out the uncertainty quantification to analyze the sensitivity in the forecast wind speed to some important model parameters. A stochastic collocation method based on polynomial chaos expansion (PCE) has been used to obtain the statistics of the numerical results with

uncertainties in constants of the turbulence model ($k - \epsilon$ model) and the wind profile parameter α in the inflow conditions of the coupled model. It is found that the surface wind speed prediction from the coupled model is much more sensitive to parameter α than other parameters in the turbulence model. The uncertainties in the five parameters lead to weak impact on wind direction forecasts. The present work sheds a light on the importance of the inflow conditions for the CFD model, and suggests the next step to further improve the wind speed forecasting skill of the coupled model. A system to assimilate parameter α using the observation data of the target wind farm is under development.

Chapter 5

Estimation of computation condition based on PCE data assimilation for pneumatic throttle equipment

5.1 PCE based data assimilation framework

In the previous two chapters, the effect of uncertainties was quantitatively evaluated and useful knowledge was attained based on PCE methodology. In this chapter, as an advanced usage of PCE methodology, an estimation method based on PCE to assimilate the calculation condition to experimental data is presented and implemented for a pneumatic throttle problem. In the method, a PCE surrogate model of numerical simulation is constructed from stochastic collocation method, and simulation input and simulation result is also represented as PCE coefficients. Then, the numerical simulation procedure represented as a projection via response surface from simulation input to simulation result. From the characteristics of polynomial, the derivatives between PCE coefficients of simulation input and simulation result is attained. Moreover, from these derivations, PCE coefficients of simulation input could be assimilated with the PCE coefficients of outlet derived from the experimental measurement. This methodology enables a fluid flow phenomenon where the simulation input is unknown, but the outlet condition can

be measured. Estimation of the calculation condition of pneumatic throttle problem with outlet measurement is conducted using this method.

5.1.1 General framework of PCE based estimation of computation condition

A simulation system f could be represented as a function of computation condition u to simulation result d,

$$f : u \mapsto d. \tag{5.1}$$

With this representation, consider a simulation input u is unknown and a probability density function of system output $\check{d}$ has measured by experiment. To conduct numerical simulation, the computation condition should be attained from the probability distribution of system output.

First, from the stochastic collocation method, a PCE surrogated model of the simulation system should be attained as

$$\tilde{f}(u) = \sum_{i=0}^{P} \hat{f}_i \phi_i(\zeta), \tag{5.2}$$

with

$$\hat{f}_i = \frac{1}{\gamma_i} \sum_{n=1}^{N} f(\zeta_n)\phi_i(\zeta_n)p(\zeta_n)w_n, \tag{5.3}$$

$$\gamma_i = \int \phi_i(\xi)^2 p(\xi) d\xi. \tag{5.4}$$

In here, with the upper bound of computation condition estimation u_{max} and the lower bound u_{min}

$$\zeta := \frac{u - (u_{max} + u_{min})/2}{\Delta u} \tag{5.5}$$

with

$$\Delta u := (u_{max} - u_{min})/2 \tag{5.6}$$

denotes weighted velocity $[u_{min} : u_{max}] \mapsto [-1 : 1]$ and ζ_n denotes quadrature points. The upper bound and the lower bound of computation condition estimation should be determined priorly. PCE of computation condition is represented as

$$\tilde{u}(\xi) = \sum_{j=0}^{P} \hat{u}_j \phi_j(\xi), \tag{5.7}$$

and PCE of system output is

$$\tilde{d}(\xi) = \sum_{k=0}^{P} \hat{d}_k \phi_k(\xi). \tag{5.8}$$

The PCE coefficients of system output are attained from the least square approximation to the measured probability density of system output, but the PCE coefficients of computation condition remain unknown with this formulation.

5.1.2 Estimation of computation condition using the derivative of PCE coefficients

The PCE coefficients of system output, equation (5.8), also can be represented by the formulation of stochastic collocation,

$$\begin{aligned} \hat{d}_k =& \frac{\int f(u)\phi_k(\xi)p(\xi)d\xi}{\int \phi_k(\xi)^2 p(\xi)d\xi} \\ =& \frac{1}{\gamma_k} \sum_{\ell=1}^{N} \phi_k(\xi_\ell) p(\xi_\ell) w_\ell \sum_{i=0}^{P} \hat{f}_i \phi_i(\zeta). \end{aligned} \tag{5.9}$$

Differentiating the equation (5.9) with the PCE coefficients of the computation condition $\hat{u}_j$, the derivative

$$\begin{aligned} \frac{\partial \hat{d}_k}{\partial \hat{u}_j} =& \frac{1}{\gamma_k} \sum_{\ell=1}^{N} \sum_{i=0}^{P} \hat{f}_i \left. \frac{\partial \phi_i(\zeta)}{\partial \hat{u}_j} \right|_{u=u_n} \phi_k(\xi_\ell) p(\xi_\ell) w_\ell \\ =& \frac{1}{\gamma_k \Delta u} \sum_{\ell=1}^{N} \sum_{i=0}^{P} \hat{f}_i \left. \frac{\partial \phi_i(\zeta)}{\partial \zeta} \right|_{u=u_n} \phi_j(\xi_\ell) \phi_k(\xi_\ell) p(\xi_\ell) w_\ell \end{aligned} \tag{5.10}$$

is attained. In here, the derivative term on the right side is attained from direct differentiation or derivative characteristic of the basis polynomial. For example, the derivative characteristic of the Jacobi polynomials is

$$\frac{d^k}{dz^k} P_n^{(\alpha,\beta)}(z) = \frac{\Gamma(\alpha+\beta+n+1+k)}{2^k \Gamma(\alpha+\beta+n+1)} P_{n-k}^{(\alpha+k,\beta+k)}(z), \tag{5.11}$$

and the derivative of the Legendre polynomials is attained from the special case of Jacobi polynomials with $\alpha = \beta = 0$.

With these derivatives, the Jacobian matrix between the PCE coefficients of computation condition and system output is attained as

$$J = \left\{ \frac{\partial \hat{d}_i}{\partial \hat{u}_j} \right\}. \tag{5.12}$$

And the PCE coefficients of computation condition can be estimated from the Newton-Raphson method. With the vector form of the PCE coefficients

$$\hat{\boldsymbol{u}} = \begin{bmatrix} \hat{u}_0 \\ \hat{u}_1 \\ \hat{u}_2 \\ \vdots \\ \hat{u}_P \end{bmatrix}, \tag{5.13}$$

$$\hat{\boldsymbol{d}} = \begin{bmatrix} \hat{d}_0 \\ \hat{d}_1 \\ \hat{d}_2 \\ \vdots \\ \hat{d}_P \end{bmatrix}, \tag{5.14}$$

the Newton-Raphson method is represented as

$$\hat{\boldsymbol{u}}^{\text{new}} = \hat{\boldsymbol{u}}^{\text{old}} + J^{-1} \left(\hat{\boldsymbol{d}}^{\text{real}} - \hat{\boldsymbol{d}}^{\text{old}} \right). \tag{5.15}$$

In here, $\hat{\boldsymbol{u}}^{\text{new}}$ denotes updated PCE coefficient of computation condition and $\hat{\boldsymbol{u}}^{\text{old}}$ denotes the PCE coefficients before update. $\hat{\boldsymbol{d}}^{\text{real}}$ is the PCE coefficients attained from experimental measurement with least square algorithm and $\hat{\boldsymbol{d}}^{\text{old}}$ is the PCE coefficient calculated from $\hat{\boldsymbol{u}}^{\text{old}}$ using stochastic collocation formulation in equation (5.9). This Newton-Raphson update iterates until the difference between the PCE coefficients converge. When the Newton-Raphson iteration converged, the estimated PCE coefficients of computation condition is attained.

5.2 Pneumatic throttle problem

Pneumatics is a branch of engineering that uses pressurized air or gas as a working medium and converts or transfers energy using the change of state or fluid flow. In pneumatics, characteristics of air as a compressible fluid are actively used to solve engineering problems. For instance, the pneumatic cylinder uses pressurized air or gas as a working medium of pressure and air blow uses pressurized air as a flow to elude dust without contact. When we want to use pneumatic machines, a pneumatic system transfer pneumatic energy to the pneumatic machine should be constructed. Inside almost every pneumatic system, to control fluid flow or the state change of working medium, pneumatic valves are necessarily used.

From this reason, measuring and representing steady or nonsteady characteristics of pneumatic valves has been studied by many engineers and researchers. A recognizable movement in the study of the pneumatic valve is a standardization[19] addressed by[50]. In this approach, the pressure–flow rate characteristic is represented as two parameters: sonic impedance and critical back-pressure. With this representation, complex flow phenomenon of pneumatic valves with different inner shapes could be modeled as the fluid flow of a simple pneumatic throttle.

5.2.1 Experiment design

In this section, the fluid flow of a pneumatic throttle is analyzed with experiment and simulation, respectively, and the calculation condition for numerical simulation to reproduce experiment numerically is attained from the aforementioned data assimilation method. In the experiment, physical quantities of upstream and downstream of the pneumatic throttle are measured with measuring instruments with measuring error. Using the measurement result of the downstream, boundary condition of the upstream is estimated with surrogate PCE model.

The pneumatic circuit used for experiment and a picture of experimental setup are shown in figure 5.1 and 5.2. At the most upstream, pressure comes from air source is

stably supplied through a pressure control valve. Between the pressure control valve and the pneumatic throttle, there is a variable throttle. By changing the opening degree of the variable throttle, the upstream pressure of the measured throttle changes. During the change of pressure, upstream pressure and downstream mass flow rate of the pneumatic throttle are measured from measuring instruments installed on upstream and downstream, respectively. The most downstream is freely released.

As the measuring instruments, two laminar flowmeters with built-in pressure gage (QFS-50; Tokyo meter co.) was used. For the downstream, the measurement result of the mass flow rate is only used, and for the upstream, the pressure, measured by built-in pressure gage of flowmeter, was used. The prescisson on specifications of laminar flow meter is $\pm 3\%$ of the full scale, about 3.0×10^{-5}kg/m^3. For accurate measuring, the flow meter has been calibrated by sonic nozzle type gas flow calibrators (MRS102, MRS103, and MRS104; Hirai). These calibrators have uncertainty, 0.3% of measured value on specifications, but the uncertainty of calibrators was neglectable; less than 3.0×10^{-6}kg/m^3 with a maximum flow rate.

Measurement with measuring error is conducted by two step. The upstream pressure and downstream mass flow rated was measured with fluttering pressure condition, and a series of data length of 0.8 second of measured data starting around 140kPa was extracted from the pressure fluttering. The response of measuring instrument was attained with 1000Hz, and in 0.8 second 800 measured data exists. The measured data is divide was 15 dataset with 100 data overlapping 50 data with adjacent datasets. Each dataset was used as distributed measurement data of 15 measured points interval with 0.05 second. Respectively, measurement error without fluid flow was measured. The response of the measuring instruments was recored without fluid flow condition for 15 minutes. With convolution of the probability distribution of attained dataset and response without fluid flow, a expected probability distribution of the true value was generated.

The throttle is a 1mm circle shaped hole with 6mm length, and 8mm pipe is connected at forward and afterward of the throttle as shown in figure 5.3. A compound mesh of the throttle used for CFD analysis is represented in figure 5.4. The size of mesh became small in the center side of the throttle, and the squeezed hole has more than 20 mesh elements in the diameter direction. The downstream boundary condition has assigned as free flow

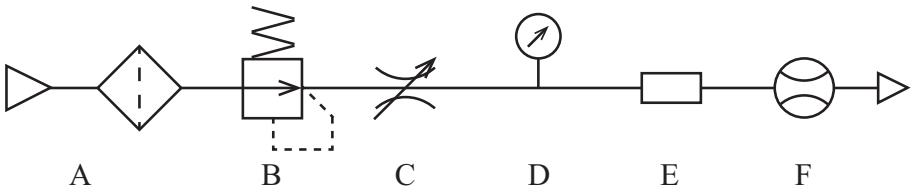

A: air source and filter, B: pressure control valve, C: variable throttle,
D: pressure gage, E: pneumatic throttle, F: flowmeter

Fig.5.1: Pneumatic circuit of experiment

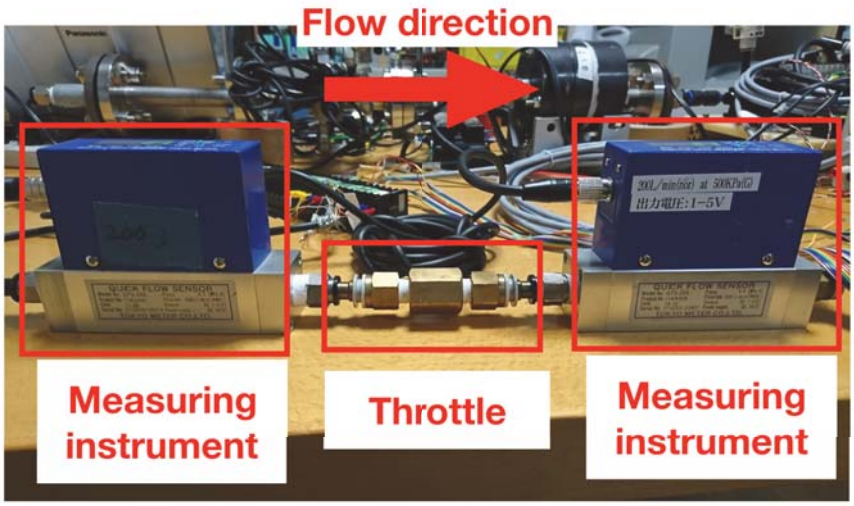

Fig.5.2: Pneumatic throttle and measuring instruments

out with 100kPa, and inlet boundary has assigned as constant pressure. The value of the inlet pressure will be attained from quadrature points ζ_n with the upper boundary of 150kPa and lower boundary of 120 kPa, equation (5.5), to attain surrogate PCE model of the simulation system. As a quadrature rule, Clenshaw Curtis quadrature discussed in Section 2 was used. The initial condition was attained as a stable state flow field with Inlet pressure of 135 kPa with the replacement of upstream pressure over 120kPa as the quadrature point values for faster convergence of flow field. The numerical simulation was conducted using OpenFoam. The "rhoCentralFoam" [15], which is able to solve compressible fluid of subsonic region, was chosen. As a turbulence model, LES(Large eddy simulation) model was adopted.

With simulation results of the quadrature points, a surrogate PCE model of the simulation system is attained. Attained surrogate model is used to estimate the upstream pressure using the expected probability distribution of downstream mass flow rate. The probability distribution of upstream pressure is estimated by the method presented in section 5.1.2. With a comparison between the estimated upstream pressure and measurements on upstream pressure, the validity of this estimation method is confirmed

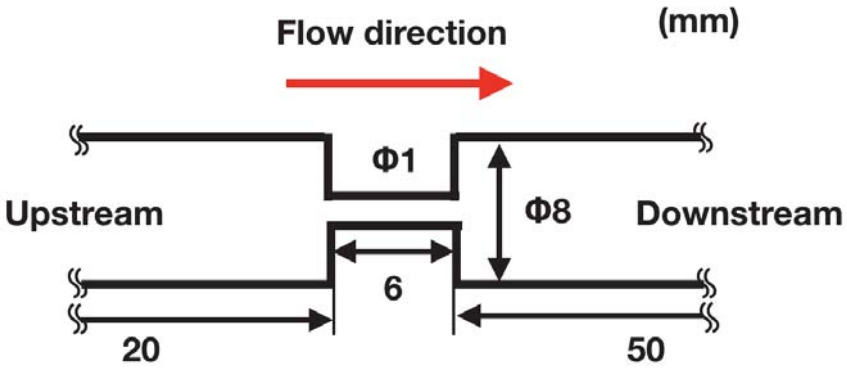

Fig.5.3: Inner shape of the pneumatic throttle

5.2.2 Calibration of measuring equipment

The calibration result of flowmeter is figured on figure 5.5. The mass flow rates measured by the calibrators with the voltage responses of the flowmeter are represented as the black crosses. With these calibration points the characteristic line of the measuring instrument attained with the least square method. Because laminar flowmeter response linearly with pressure change[11], a simple linear line

$$G = a_1 + a_2 V \tag{5.16}$$

was chosen as characteristic line. The least square error between characteristic line and measurements at calibration points was 1.3445×10^{-5}.

5.2.3 Measured values and generated expected probability distributions

The measured values with measuring instruments on the upstream and downstream are shown in figure 5.6 and 5.7. Measurement data within 0.8 sec, starting around 140kPa

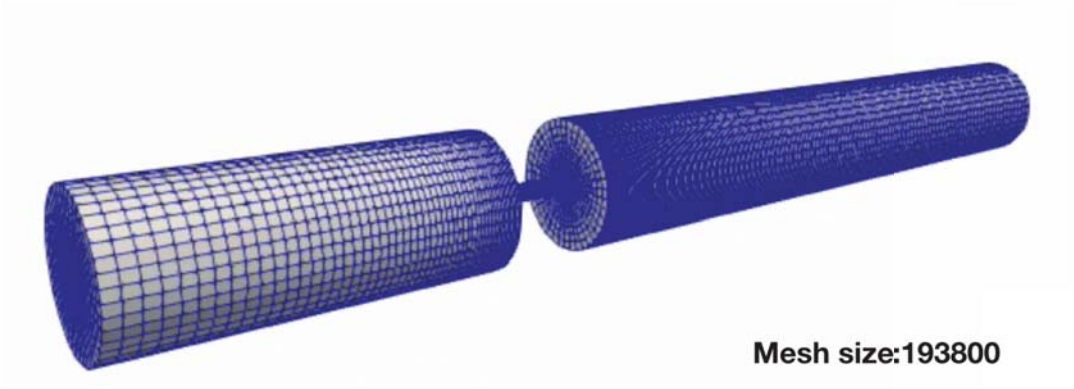

(a) oblique view

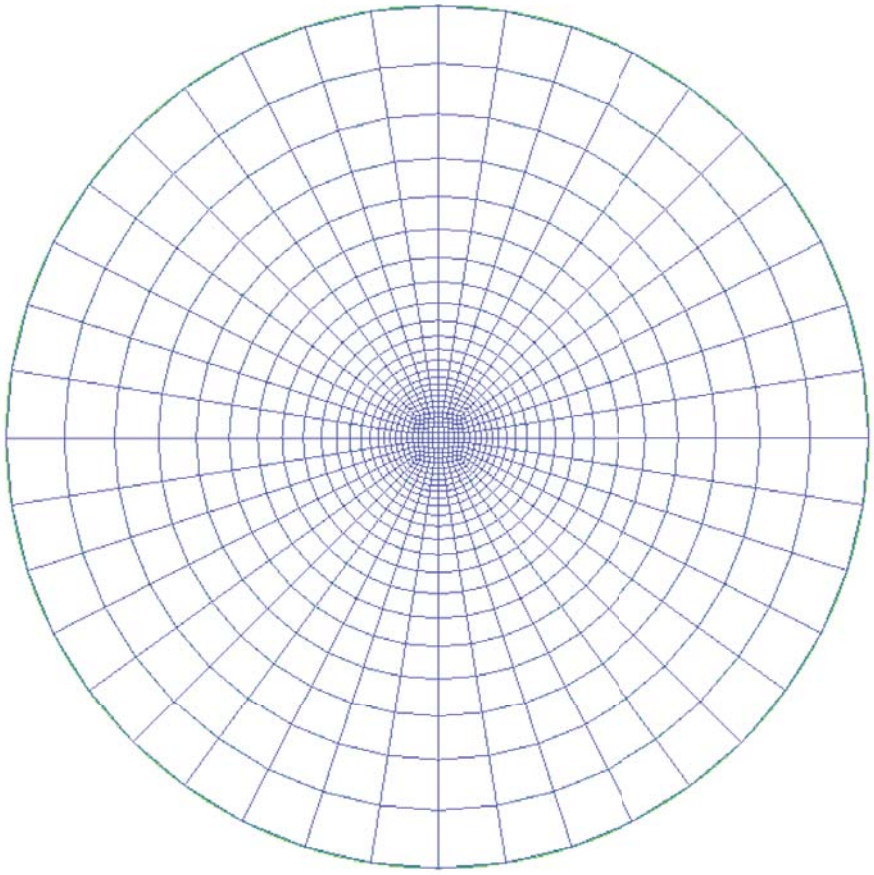

(b) sectional view on the inlet boundary

Fig.5.4: Caculation mesh of the pneumatic throttle

was selected from a series of measurement with pressure fluctuation generated from the change of the opening in the variable throttle in the pneumatic circuit 5.1. The measured

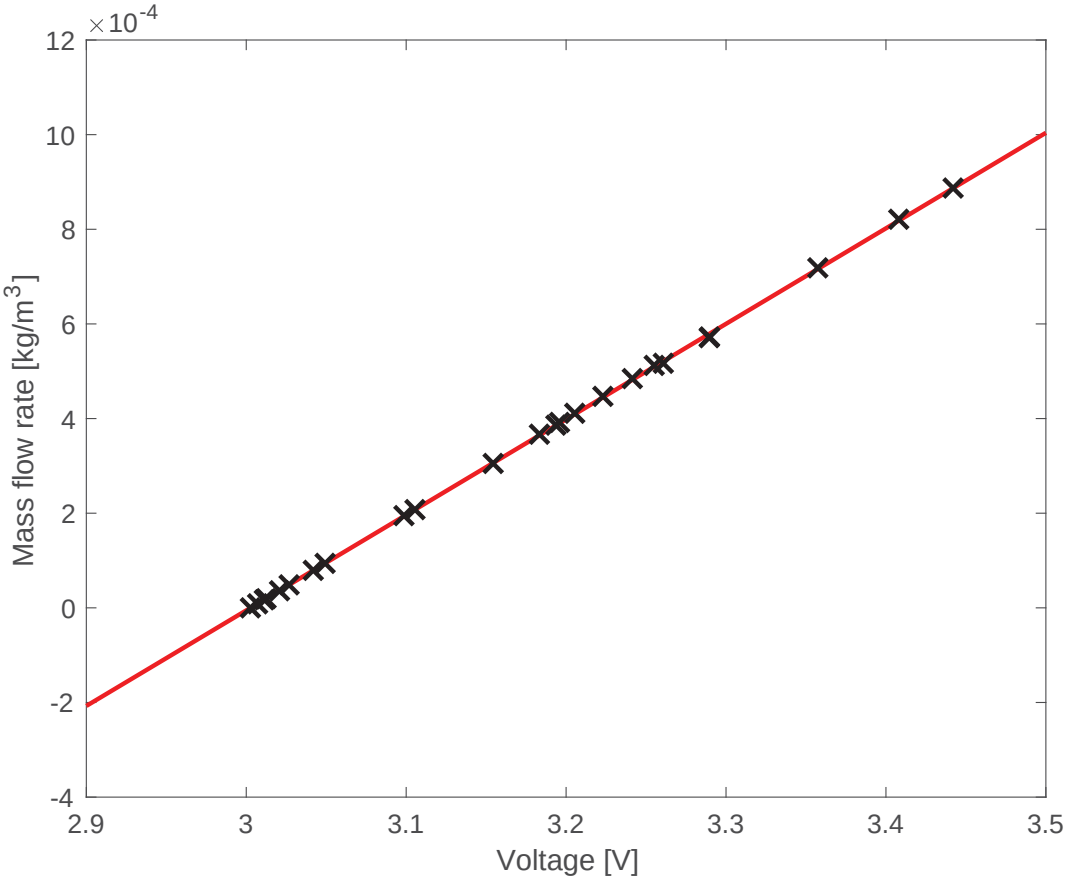

Fig.5.5: Calibration result of the flowmeter. Black crosses are measured values using calibrators, and the red line is the characteristic line of the measuring instrument attained with the least square method.

pressure decrease by about 126 kPa at around 0.45 second and return to around 137 kPa in the time range. The mass flow rate, measured by the calibrated flowmeter at the downstream, responses to the change of the upstream pressure change, and shows similar decreasing - increasing profile change. Distributes of measured values resulted from measuring error are shown in both figures. The measured mass flow rate is used to estimate upstream pressure, and the measured pressure is compared with the estimated pressure values. Fifteen datasets with 100 data, corresponding 0.1 seconds as shown in figure 5.8, are generated from the measured mass flow rate with overlapping of 50 data between adjacent datasets.

The mass probability density of measurement error without fluid flow for 15 minutes is

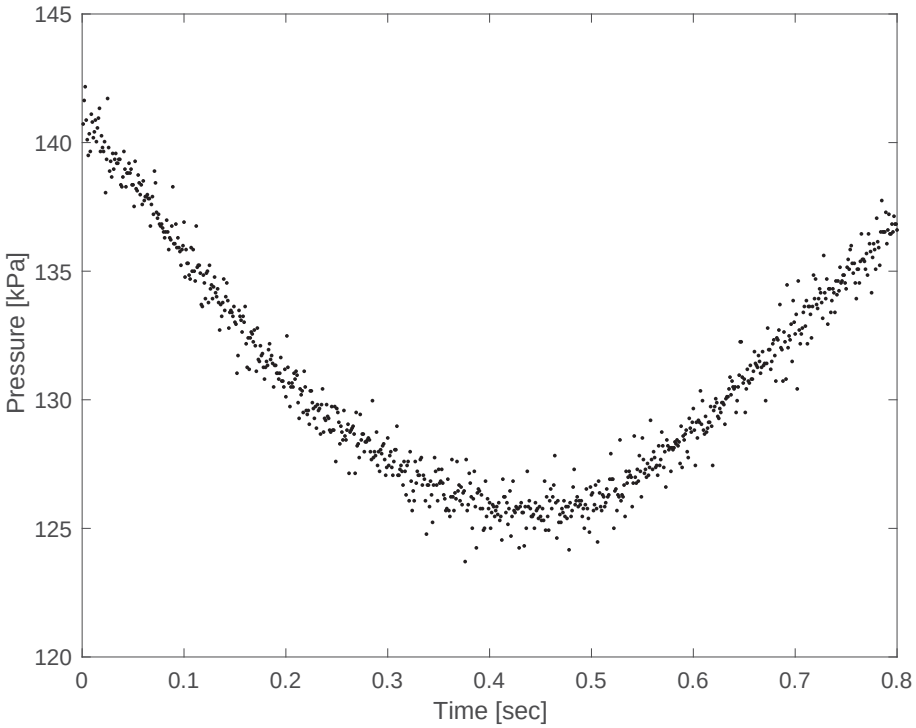

Fig.5.6: Pressure change at the upstream

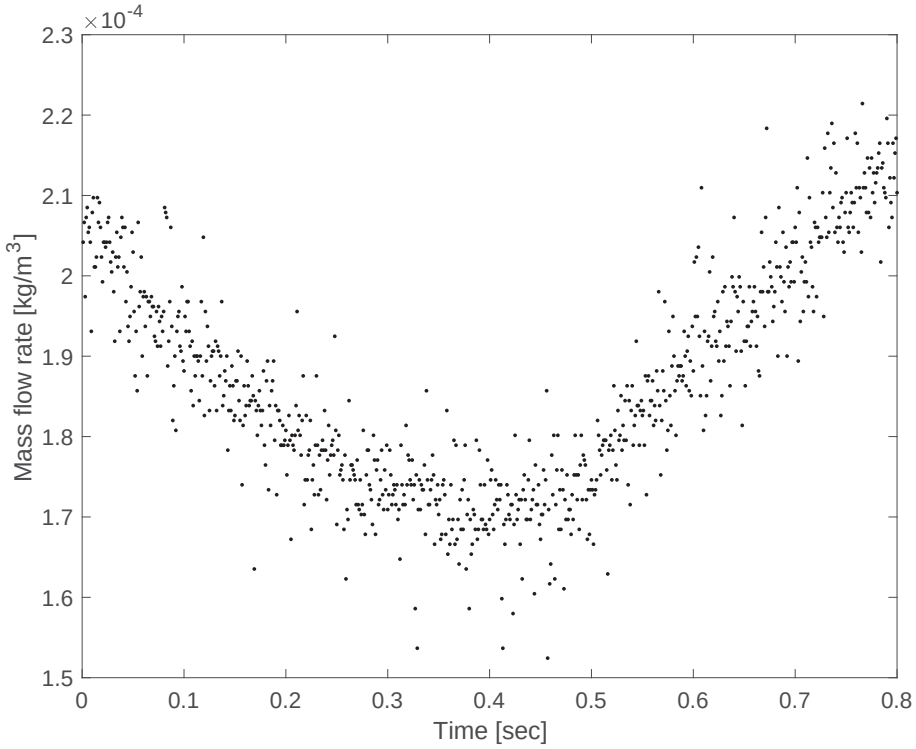

Fig.5.7: Mass flow rate change at the downstream

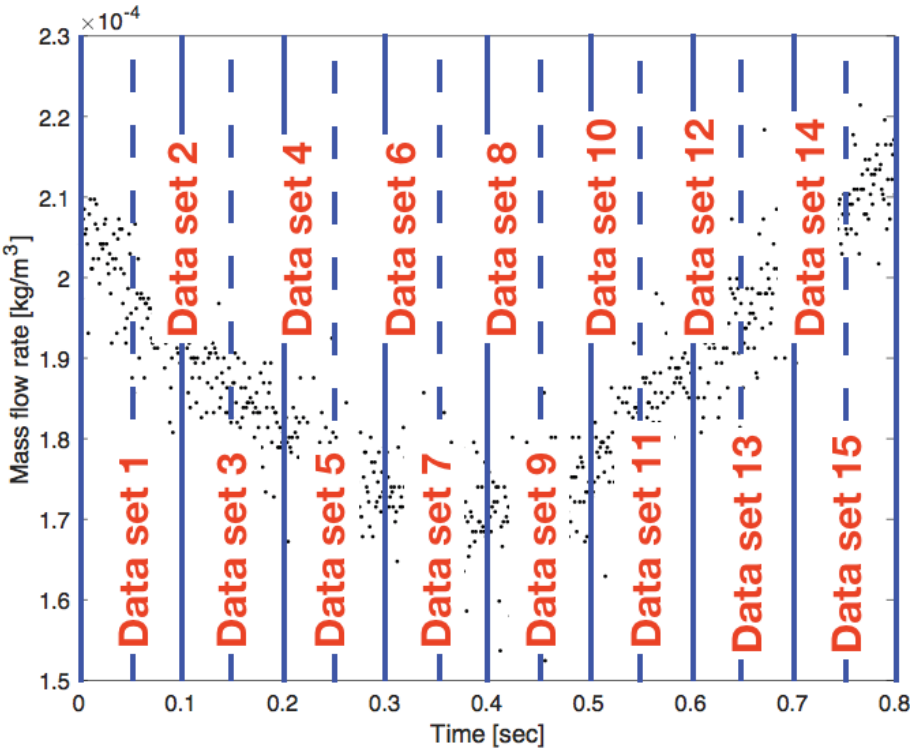

Fig.5.8: Fifteen datasets with 100 data with overlapping of 50 data between adjacent datasets.

figured on figure 5.9. This measurement error is considered as the electrical error generated from the measurement circuit because the errors are randomly generated despite fluid does not flow. Bias in the positive side and distribution left, and right side of peak point is represented. With this distribution, expected probability distributions of each dataset are generated.

Generated expected probability distributions of 1st, 6th and 12th dataset with the mass probability densities are represented on figure 5.10. Figures on the left frames, frame (a), (c) and (e), are the mass probability densities and the right frames shows the expected probability distributions. Expected probability distributions are generated from convoluting the mass probability densities and the distribution of measurement error with opposite value. These expected probability distributions denote probability of possible true value with the datasets.

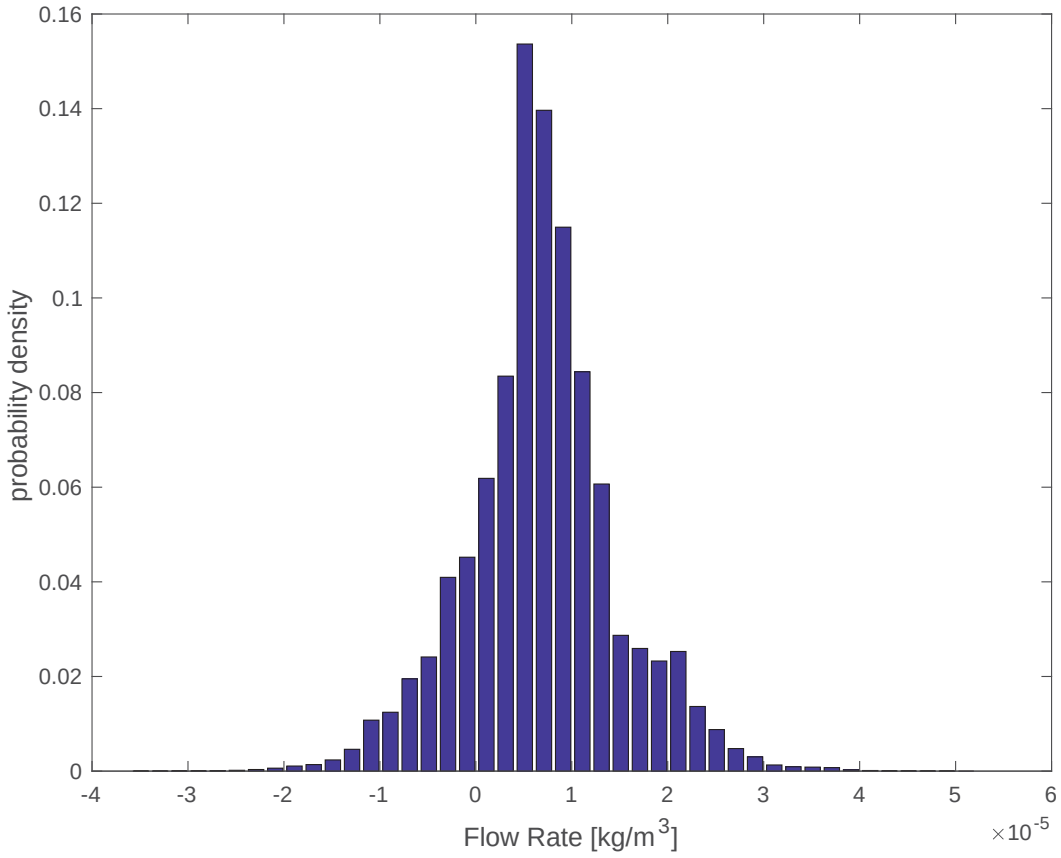

Fig.5.9: Mass probability density of mass flow rate

5.2.4 Construction of surrogate PCE model

The response of pneumatic valves, including throttle, generally evaluated from the pressure-flow rate characteristics[11,19]. Pressure - mass flow rate characteristics measured from the experiment is figured with the response of numerical simulation on the quadrature point in figure 5.11. Despite the values of experimental measurement distributes which could not be found in deterministic numerical simulation, the numerical simulation results accept with the experimental results. From this deterministic numerical results on quadrature points with high acceptance with experimental results, a surrogated PCE model, as shown in figure 5.12, is generated. In this surrogate model, the response of the model has been determined from a series of Legendre polynomial with PCE coefficients,

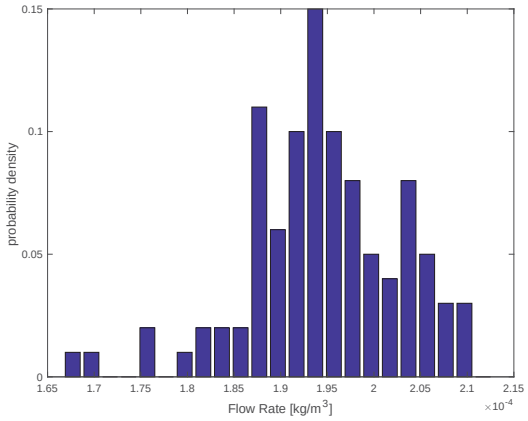

(a) Mass probability density distribution of 1st dataset

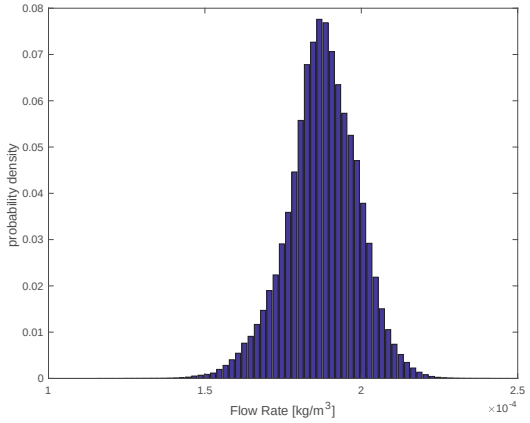

(b) Expected probability distribution of true value with 1st dataset

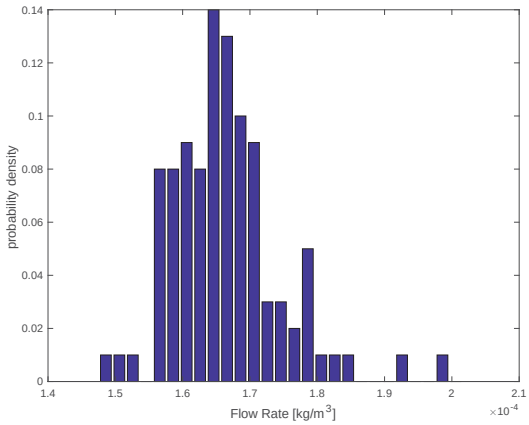

(c) Mass probability density distribution of 6th dataset

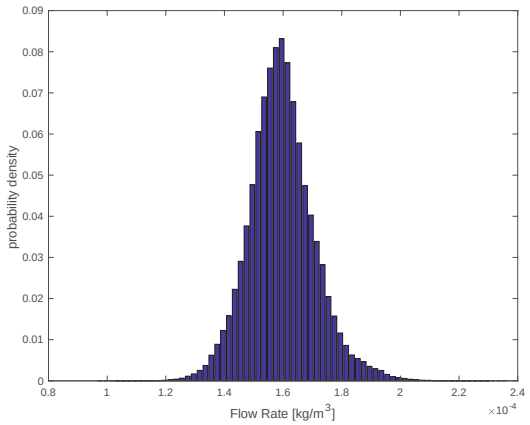

(d) Expected probability distribution of true value with 6th dataset

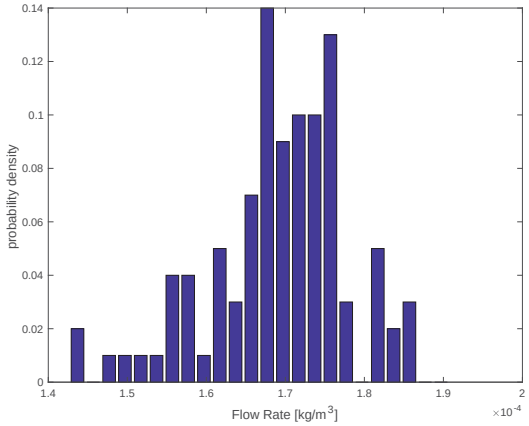

(e) Mass probability density distribution of 12th dataset

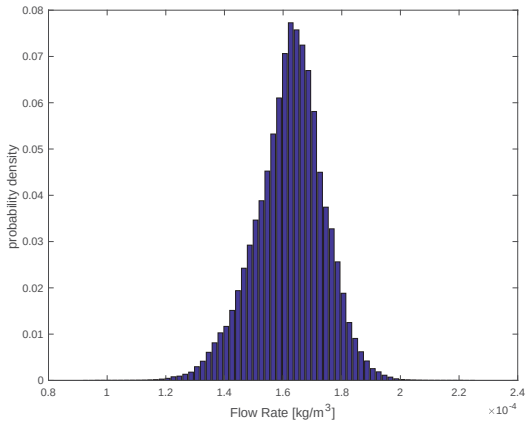

(f) Expected probability distribution of true value with 12th dataset

Fig.5.10: Mass probability density distribution and expected probability distribution of datasets

as shown at 5.3, attained from stochastic collocation method. With this model, a numerical simulation is approximated a simple polynomial system with weighted inlet pressure *zeta*, and the approximated result of the simulation is attained from the value of the polynomial at that inlet condition. Using this surrogate PCE model, assimilation of upstream calculation condition from the experimental measurement of downstream with the method presented in section 5.1.2 was conducted. The assimilation result is reported in the next subsection.

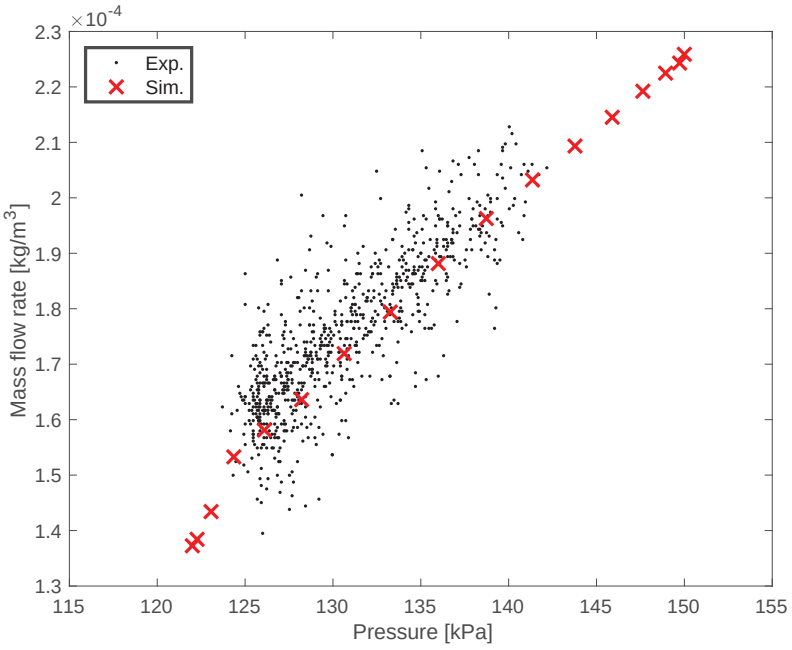

Fig.5.11: Pressure - mass flow rate characteristic of pneumatic throttle.

5.2.5 Assimilation result and discussion

Assimilated pressure of inlet of calculation domain and mass flow rate of outlet to the measurement of downstream has been represented in figure 5.13 with PCE representation. From the right side frames; frame (b), (d), and (f), the converged PCE of estimation to PCE of experimental measurement. For the PCE of experimental measurement, the expected probability density distribution, attained from a numerical convolution of the measured value and measured error for 15 minutes without flow fluid. The convergence of the Newton Raphson iteration explained in equation (5.15), has evaluated from the sum-

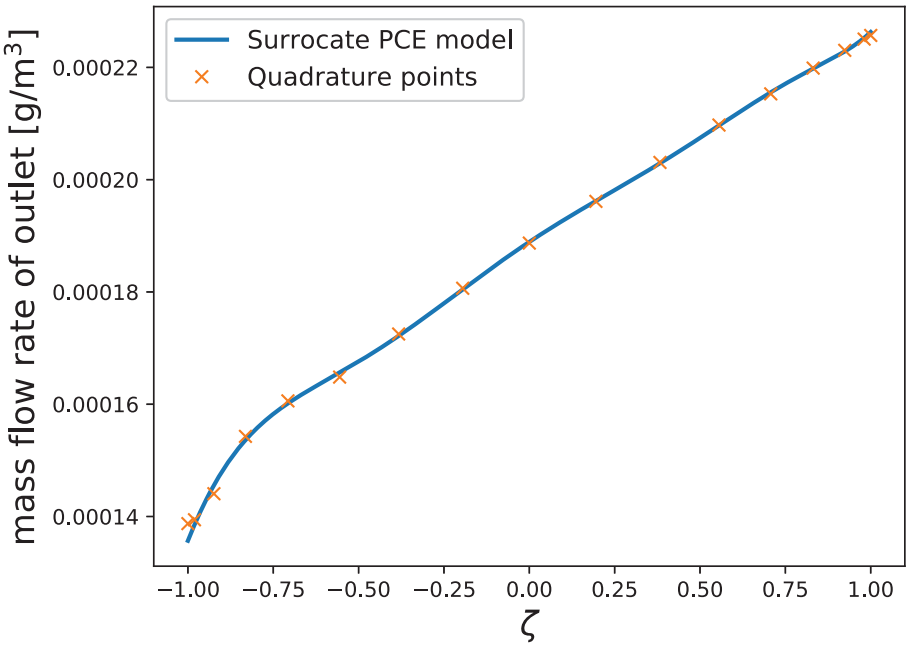

Fig.5.12: Surrogate PCE model of the numerical simulation system

mation of the absolute difference between PCE coefficients. If the convergence indicator became less than 10^{-10}, the Newton-Raphson iteration is deemed to converge.

The assimilated calculation conditions are represented in left frames of figure 5.13; frame (a), (c), and (e) with the PCE of experimental measurement. For every dataset, the estimated values agree well with the measured inlet pressure regarding the distribution of probability density function. The IQR boxes calculated from the estimated inlet pressure of each data set is shown in figure 5.14. The estimated IQR box are well agreed with the experimental data, and experimental observations are included in IQR box ranges.

The assimilated calculation conditions are represented in left frames of figure 5.13; frame (a), (c), and (e) with the PCE of experimental measurement. For every dataset, the estimated values agree well with the measured inlet pressure regarding the distribution of probability density function. The IQR boxes calculated from the estimated inlet pressure of each data set is shown in figure 5.14. The estimated IQR boxes are well agreed with the experimental data, and experimental observations are included in IQR box ranges.

For quantitative comparison between estimated result with the experimental observations, the IQR boxes of experimental observations were attained and represented in 5.15. The statistic characteristics of each data set represented as IQR box form. Not only the

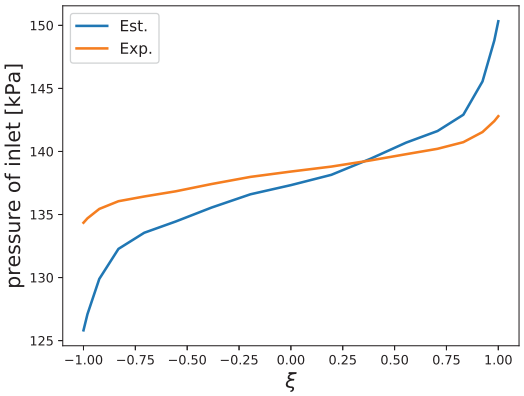

(a) PCE of estimated inlet pressure and measurement in 1st dataset

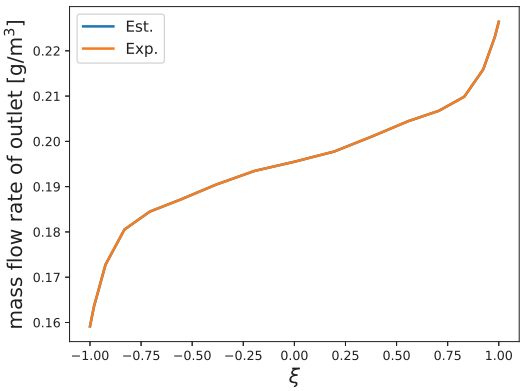

(b) Assimilated mass flow rate of outlet in 1st dataset

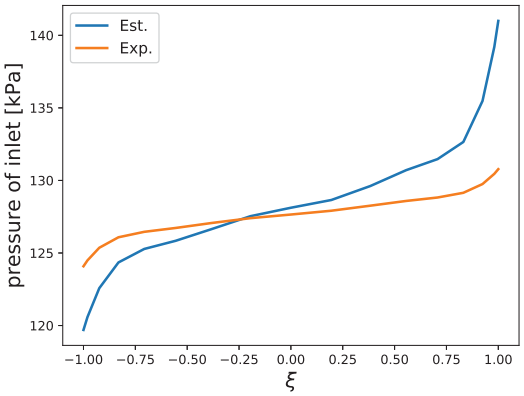

(c) PCE of estimated inlet pressure and measurement in 6th dataset

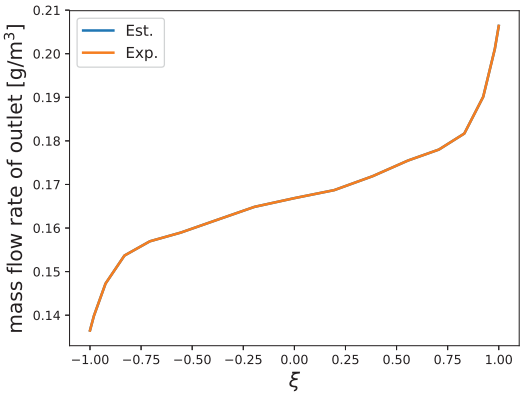

(d) Assimilated mass flow rate of outlet in 6th dataset

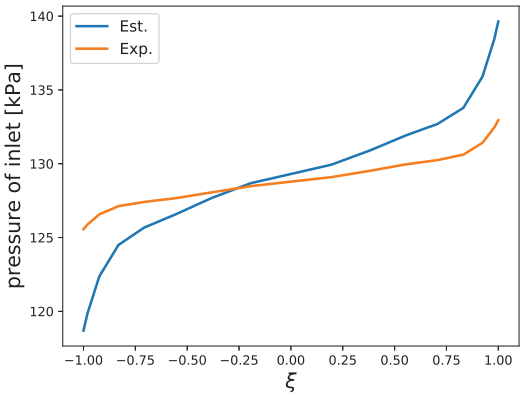

(e) PCE of estimated inlet pressure and measurement in 6th dataset

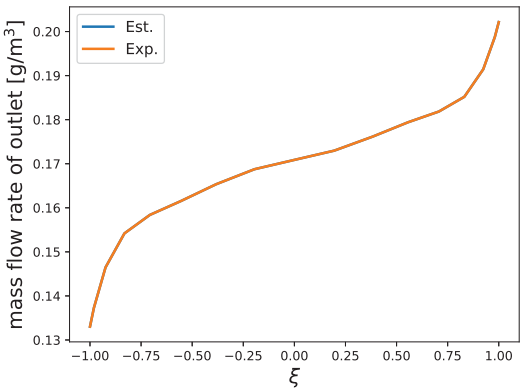

(f) Assimilated mass flow rate of outlet in 12th dataset

Fig.5.13: PCE representation of data assimilation results

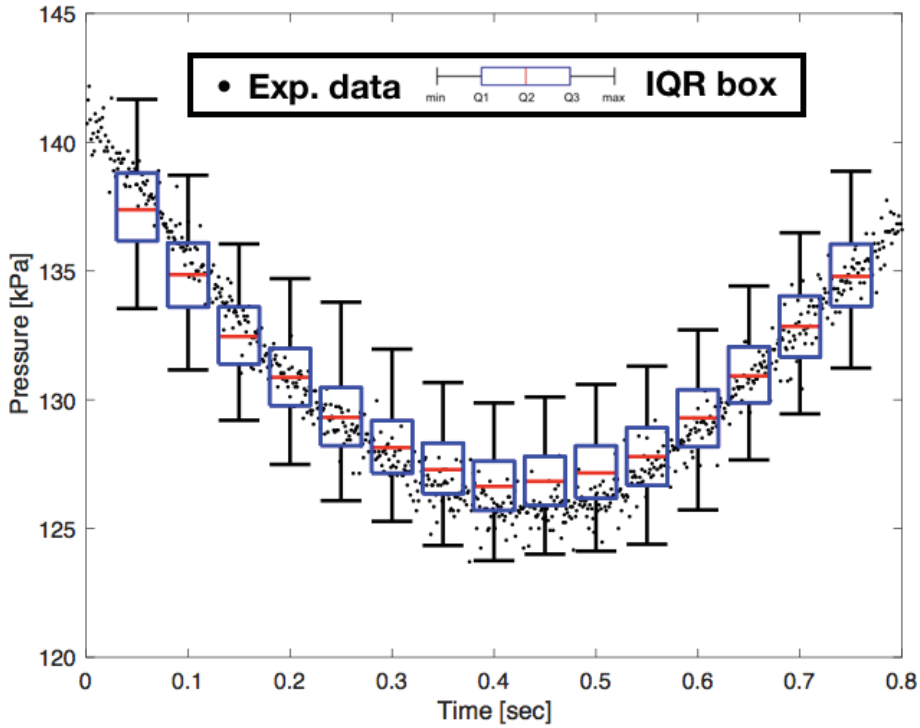

Fig.5.14: Estimated IQR boxes of each dataset

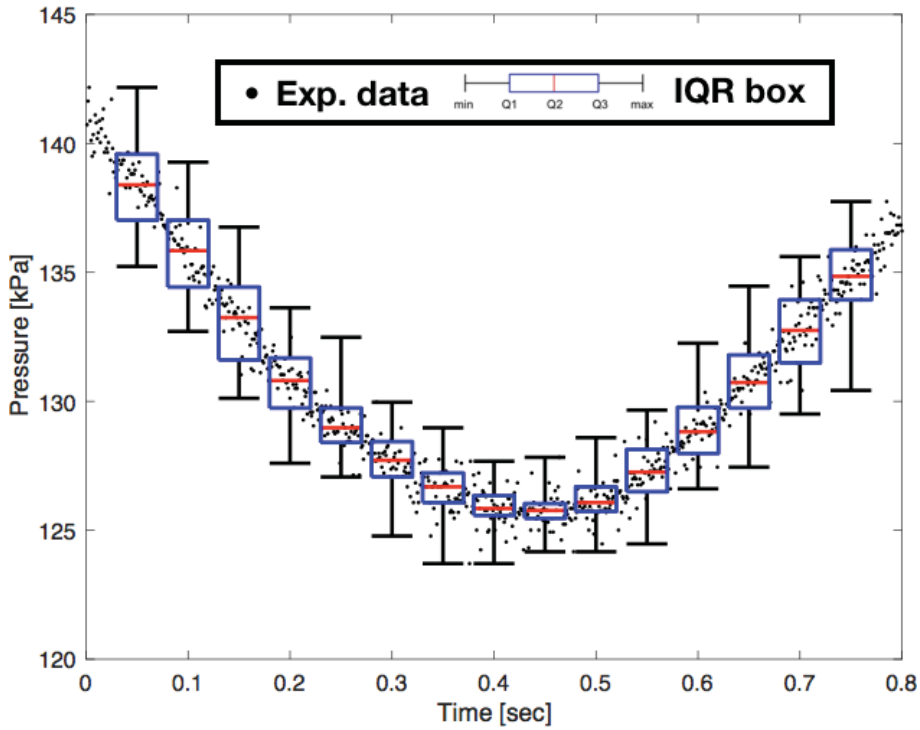

Fig.5.15: IQR boxes of each dataset calculated from PCE of experimental data

Table 5.1: Difference of IQR points value between estimated inlet pressure and observation [kPa]

data set numbering	Min.	Q2	median	Q3	Max.
1	-1.69	-0.86	-1.02	-0.78	-0.51
2	-1.55	-0.83	-0.98	-0.93	-0.56
3	-0.91	-0.22	-0.79	-0.83	-0.71
4	-0.11	0.04	0.07	0.31	1.08
5	-0.98	-0.19	0.34	0.74	1.31
6	0.50	0.08	0.43	0.75	2.00
7	0.63	0.27	0.60	1.10	1.70
8	0.05	0.13	0.79	1.27	2.20
9	-0.16	0.44	1.06	1.76	2.28
10	-0.04	0.44	1.08	1.53	2.00
11	-0.08	0.18	0.54	0.78	1.64
12	-0.89	0.19	0.47	0.62	0.46
13	0.22	0.15	0.20	0.26	-0.05
14	-0.06	0.16	0.10	0.10	0.87
15	0.81	-0.3 0	-0.057	0.17	1.13

median value represented as a short red horizontal line inside the IQR box, but also the maximum and minimum value are represented as upper and lower whiskers, and Q1 and Q3 point shown as with blue box range.

The difference between IQR boxes of estimation with those of experimental observation is shown in table 5.1. The difference in median value with estimation and observation was less than 1.1 kPa. The differences of Q1 and Q3 values were lass than 0.9 kPa and 1.8 kPa, respectively. The minimum and maximum values showed comparatively significant differences (less than 1.7 kPa and 2.3 respectively), but these difference still in less than the measurement uncertainty of the measuring device (10kPa in the catalog of Tokyo meter co.). From these points, we can conclude that the presented assimilation method is validated in this pneumatic throttle problem.

5.3 Summary

A PCE based data assimilation method using surrogate PCE model constructed from stochastic collocation method was developed. In the developed method, the simulation input and the response of the simulation system also represented as PCE representation, and the derivative relationship between PCE coefficient of the input and the response in attained using the derivative characteristics of the orthogonal polynomial. A original assimilation framework use this derivative relationship where the simulation input is assimilated to the experimental measurement of system response has presented.

An application of the presented assimilation method on the pneumatic squeeze phenomenon was implemented. A surrogate PCE model of the problem situation was constructed using the CFD simulation on the quadrature points in the discussed range. And, the outlet response of system with measurement uncertainty was measured using a flowmeter. Uncertainty resulted from the electrical noise of measurement device, which is one of the significant uncertainty resource, was also measured, separately. From the convolution of the measured response and the measured noise, estimated probability density function of the system response was generated. Using the presented assimilation methodology, the inlet condition of the system was estimated by adapting the inlet condition to the estimated probability density of the response. The estimated result was validated from quantitative comparison with the measurement at the inlet point.

Chapter 6

Summary and future works

6.1 Summary and archievement

The present thesis develops a framework to quantify the effect of uncertainty inherent in simulation input and makes use of the quantified characteristics of the simulation system to enhance the utility of simulation system for real fluid phenomena.

We constructed a system to quantitatively evaluate the uncertainty inherent in simulation inputs of fluid dynamics simulation. In the constructed system, the uncertainty quantification method based on polynomial chaos expansion (PCE) methodology was used from calculation efficiency. The PCE based approaches are explained precisely, and the characteristics of PCE based uncertainty quantification methods were discussed using the Burgers' equation. Based on the foregoing discussion, the stochastic collocation method, which analysis stochastic characteristics of a random response of simulation system with numerical quadrature of system response at quadrature point, was adopted from the calculation and implement efficiency. Furthermore, selection of the numerical quadrature for the stochastic collocation method was discussed based on simple numerical tests.

With this constructed system, effect of uncertainty on representative fluid flow phenomenon; shock and interfacial multiphase fluid interaction which is sensitive to uncertainty inevitable in experimental condition, multi-scale wind forecast model where study to find the most critical parameter to refine the multi-scale model is demanded, and fluid flow inside a pneumatic throttle where fluid flow with determined direction and the mea-

surement of outlet condition is assumed only possible, was quantified and usage of the statistic characteristics attained by the quantification results is exhibited.

First, the effect of initial density uncertainty, significant effects on the interaction had mentioned from experimental research, of representative six shock-interfacial multiphase flow interaction structure was quantitatively evaluated. For every six cases, the uncertainty in the density of contaminated media was modeled as the Hermite chaos where the probability distribution of the uncertainty is assumed as the Gaussian and analyzed with stochastic collocation method using the Gauss-Hermite quadrature of the simulation response. The effect of uncertainty on interaction structure was respectively evaluated, and common phenomenon between cases was discussed based on theoretical background.

The shock waves propagate the contaminated media affected strongly and the interaction structures generated from the interaction of the affected shock wave and the interface, such as precursor, expansion fan, and side shock, also affected by the density uncertainty. This effect of the uncertainty attained in this study well agreed with the distribution tendency of the experimental and simulation results reported from other researchers. The existence of the low standard deviation areas (LSDA) where the effect of uncertainty is very few were firstly explicitly confirmed with this study. Generation of the LSDA was qualitatively discussed of the shock-flat interface interactions (SFI) and the shock-bubble interactions (SBI), respectively. In the case of SFI, the generation of the LSDA on pressure field is assumed from the uncertainty works different direction on the interface side and shock side. The uncertainty mainly affects the acoustic impedance of the refracted side at the interface, and it works on the downstream side of the interaction, whereas it works upstream side of ambient the shock. Thus, the fluid field affected by different side by uncertainty and the LSDA is assumed to generate where these affect of uncertainty on different side balances. In case of SBI, the ambient fluid flow with the tangential shear flow could result in LSDA and vortex, which is consistent with the analyzed result.

In chapter 4, usage of the statistic information attained from uncertainty quantification results was applicated with the multiscale wind forecast model. The multiscale wind forecast model consists of mesoscale wind prediction with the WRF model and local wind prediction with CFD. Refinement of the wind prediction on hub height of evaluation points where the wind farm positioned had attained from this multiscale model compared with

the wind prediction conducted only from the mesoscale model. However, there are more rooms to improve the prediction accuracy by a refinement of the model parameters. We focused on turbulence parameters and wind profile parameter on the boundary of the local model and quantified the effect of the uncertainty of each parameter, respectively, to figure out the most significant parameter which could be used for the improvement of the multiscale model. Uniform uncertainty with admissibly large boundary was implemented each case, separately, and the effect of the uncertainty on wind power and wind direction on the wind farm at three typical times was evaluated.

From the quantification results, the wind profile parameter showed the most significant effect on the wind speed on wind farm position, which implicates refining the wind profile parameter could improve the wind prediction accuracy of the multiscale model. The statistic characteristic of the wind profile parameter was further discussed with the uncertainty quantification result. The wind speed - wind profile relationship was reconstructed from the PCE methodology, and the cumulative distribution function (CDF) was attained from that relationship. From the attained CDF, interquartile range (IQR range) was also calculated. The IQR range of 24-time range, where rapid wind speed change coincidently exists, was represented, and the significant effect for every 24 times, independent with the change of wind speed, was found out.

At the last part of the thesis, a PCE based data assimilation method using surrogate PCE model constructed from stochastic collocation method was developed. In the developed method, the simulation input and the response of the simulation system also represented as PCE representation, and the derivative relationship between PCE coefficient of the input and the response in attained using the derivative characteristics of the orthogonal polynomial. A original assimilation framework use this derivative relationship where the simulation input is assimilated to the experimental measurement of system response has presented.

An application of the presented assimilation method on the pneumatic squeeze phenomenon was implemented. A surrogate PCE model of the problem situation was constructed using the CFD simulation on the quadrature points in the discussed range. And, the outlet response of system with measurement uncertainty was measured using a flowmeter. Uncertainty resulted from the electrical noise of measurement device, which is one of

the significant uncertainty resource, was also measured, separately. From the convolution of the measured response and the measured noise, estimated probability density function of the system response was generated. Using the presented assimilation methodology, the inlet condition of the system was estimated by adapting the inlet condition to the estimated probability density of the response. The estimated result was validated from quantitative comparison with the measurement at the inlet point.

In the presented thesis, as summarized above, the development of a simulation system of fluid dynamics with uncertain simulation inputs and make use of uncertainty transfer characteristic based on polynomial chaos expansion has conducted. With a series of research, the effects of the uncertainties in calculation condition and model parameter on discussed fluid phenomenon were clarified. Especially for the shock and interface interaction, explicit presentation and discussion based on physical characteristic were firstly conducted. The usefulness of the statistic information attained from the uncertainty quantification was exhibited with the parameter study of the multiscale wind prediction model. Moreover, a novel data assimilation method based on PCE was presented and validated from application to a simple compressible fluid flow phenomenon.

6.2 Future works

The achievements attained in the present research proposes more broad usage of the uncertainty quantification methodology in fluid dynamics field.

First, we could found out the stable structure of the effect of uncertainty, which could induce the knowledge of physical phenomenon for shock interface interaction. Implementing the uncertainty quantification method with other complex fluid dynamic problems, an interpretation of the physical phenomenon with the stochastic aspect could be discussed. Moreover, discussion of the stability of the physical phenomenon also could quantitatively be discussed from the uncertainty quantification results.

Moreover, in this study, we introduced the usage of uncertainty quantification methodology to classify the dominant parameter of the numerical system. Additive works refining the numerical system by finding the appropriated value of the dominant parameter is proposed as a future direction of research. To the improvement of the numerical system, not

only the classification of the dominant parameter, reliable information of the phenomenon should be attained. For instance, measurement of the experimental condition could be used to adapt the dominant parameter with more reasonable value.

We also showed how the statistic information attained from the PCE approach could be used for data assimilation and estimation. The merit of the PCE usage on the data assimilation and estimation could be mainly discussed with two points.

The first one is that enhancement of calculation efficiency from the use of the PCE surrogate model. Using the PCE surrogate model, the response of the numerical simulation could be approximated as a summation of the orthogonal polynomials, which shows high convergency ratio. Once the PCE surrogate model is constructed, numerical simulation step in data assimilation and estimation could be substitute with the surrogate model, and the response could be calculated from the simplified calculation instead of the numerical simulation. Thus simplification could lessen the calculation cost when many times of numerical simulation should be performed inside the bounded calculation condition range. For instance, with the ensemble Karman filter, the numerical simulation should be performed with each ensemble, and the size of the ensemble is important for the assimilation ability. Effective calculation cost down using the PCE surrogate model was reported by Li[30]. In their works, the numerical simulation at each ensemble is successfully substituted with the response of the PCE surrogated model. Instead, when the PCE surrogate model is used, careful choice of the calculation region to construct adequate surrogate model and reliability of the constructed surrogate model should be checked carefully.

The other merit comes with the direct approximation of probability density function as the orthogonal polynomials in the PCE methodology. With practical data assimilation such as non-linear Karman filters, the distribution of uncertainty is basically assumed as the Gaussian distribution. Whereas, with the PCE approach, the discussion of random variable generated from non-Gaussian probability density function could be performed. This PCE representation more accurately represents the probability density function and statistic characteristics. However, the effect of the truncation error with the statistical probability reasoning, which frequently used for assimilation and estimation, remains unclear. Thus, works to clarify the effect of the truncation error on probabilistic reasoning should be studied for more useful usage of the PCE methodology.

Bibliography

[1] Milton Abramowitz and Irene A Stegun. *Handbook of mathematical functions: with formulas, graphs, and mathematical tables*, volume 55. Courier Corporation, 1965.

[2] Grégoire Allaire, Sébastien Clerc, and Samuel Kokh. A five-equation model for the simulation of interfaces between compressible fluids. *Journal of Computational Physics*, 181(2):577–616, 2002. doi: 10.1006/jcph.2002.7143.

[3] Richard Askey and James Arthur Wilson. *Some basic hypergeometric orthogonal polynomials that generalize Jacobi polynomials*, volume 319. American Mathematical Soc., 1985.

[4] Gabi Ben-Dor and Gabi Ben-Dor. *Shock wave reflection phenomena*, volume 2. Springer, 2007.

[5] Bert Blocken, Arne van der Hout, Johan Dekker, and Otto Weiler. CFD simulation of wind flow over natural complex terrain: case study with validation by field measurements for Ria de Ferrol, Galicia, Spain. *Journal of Wind Engineering and Industrial Aerodynamics*, 147: 43–57, 2015.

[6] Xsitaaz T Chadee, Naresh R Seegobin, and Ricardo M Clarke. Optimizing the weather research and forecasting (wrf) model for mapping the near-surface wind resources over the southernmost caribbean islands of trinidad and tobago. *Energies*, 10(7):931, 2017.

[7] CH Chang and MS Liou. A robust and accurate approach to computing compressible multiphase flow: Stratified flow model and AUSM+-up scheme. *Journal of Computational Physics*, 225:840–873, 2007. doi: 10.1016/j.jcp.2007.01.007.

[8] Yuzhang Che, Xindong Peng, Luca Delle Monache, Takayuki Kawaguchi, and Feng Xiao. A wind power forecasting system based on the weather research and forecasting model and Kalman filtering over a wind-farm in Japan. *Journal of Renewable and Sustainable Energy*, 8(1):013302, 2016.

[9] X Deng, S Inaba, B Xie, KM Shyue, and F Xiao. High fidelity discontinuity-resolving reconstruction for compressible multiphase flows with moving interfaces. *Journal of Computational Physics*, 371:945–966, 2018. doi: 10.1016/j.jcp.2018.03.036.

[10] WN Edeling, Pasquale Cinnella, Richard P Dwight, and Hester Bijl. Bayesian estimates of parameter variability in the k–ε turbulence model. *Journal of Computational Physics*, 258: 73–94, 2014.

[11] Tatsuya Funaki, Kenji Kawashima, and Toshiharu Kagawa. Characteristic analysis of laminar flow meter for gases with high speed response. *Transactions of the Society of Instrument and Control Engineers*, 40(10):1008–1013, 2004.

[12] C García-Sánchez and C Gorlé. Uncertainty quantification for microscale cfd simulations based on input from mesoscale codes. *Journal of Wind Engineering and Industrial Aerodynamics*, 176:87–97, 2018.

[13] C García-Sánchez, DA Philips, and C Gorlé. Quantifying inflow uncertainties for cfd simulations of the flow in downtown oklahoma city. *Building and Environment*, 78:118–129, 2014.

[14] Roger G Ghanem and Pol D Spanos. *Stochastic finite elements: a spectral approach*. Courier Corporation, 2003.

[15] Christopher J Greenshields, Henry G Weller, Luca Gasparini, and Jason M Reese. Implementation of semi-discrete, non-staggered central schemes in a colocated, polyhedral, finite volume framework, for high-speed viscous flows. *International journal for numerical methods in fluids*, 63(1):1–21, 2010.

[16] J-F Haas and Bradford Sturtevant. Interaction of weak shock waves with cylindrical and spherical gas inhomogeneities. *Journal of Fluid Mechanics*, 181:41–76, 1987. doi: 10.1017/S0022112087002003.

[17] Joshua P Hacker and Daran L Rife. A practical approach to sequential estimation of systematic error on near-surface mesoscale grids. *Weather and Forecasting*, 22(6):1257–1273, 2007.

[18] Leroy F Henderson, Phillip Colella, and Elbridge Gerry Puckett. On the refraction of shock waves at a slow–fast gas interface. *Journal of Fluid Mechanics*, 224:1–27, 1991. doi: 10.1017/S0022112078002475.

[19] ISO Central Secretary. Pneumatic fluid power – determination of flow-rate characteristics of components using compressible fluids – part 1: General rules and test methods for steady-state flow. Standard ISO 6358-1:2013, International Organization for Standardization, Geneva, CH, 2013.

[20] J. Jin, X. Deng, Y. Abe, and F. Xiao. Uncertainty quantification of shock–bubble interaction simulations. *Shock Waves*, Feb 2019. ISSN 1432-2153. doi: 10.1007/s00193-019-00893-4.

URL https://doi.org/10.1007/s00193-019-00893-4.

[21] Jonghoon Jin, Yuzhang Che, Jiafeng Zheng, and Feng Xiao. Uncertainty quantification of a coupled model for wind prediction at a wind farm in japan. *Energies*, 12(8), 2019. ISSN 1996-1073. doi: 10.3390/en12081505. URL http://www.mdpi.com/1996-1073/12/8/1505.

[22] Tadashi Miyakawa Jonghoon Jin and Feng Xiao. Uncertainty quantification of shock reflection transitions at multiphase interfaces. *32th the Symposium on Computational Fluid Dynamics*, (A12-4), 2018.

[23] Yoshiaki Abe Jonghoon Jin, Xi Deng and Feng Xiao. Effects of uncertainty in bubble density on flow structures in shock-bubble interaction. *9th International Conference on Computational Methods*, 2018.

[24] DI Ketcheson, M Parsani, and RJ LeVeque. High-order wave propagation algorithms for hyperbolic systems. *SIAM Journal on Scientific Computing*, 35:A351–A377, 2013. doi: 10.1137/110830320.

[25] Samuel Kokh and Frédéric Lagoutiere. An anti-diffusive numerical scheme for the simulation of interfaces between compressible fluids by means of a five-equation model. *Journal of Computational Physics*, 229(8):2773–2809, 2010. doi: 10.1016/j.jcp.2009.12.003.

[26] AN Kudryavtsev, DV Khotyanovsky, MS Ivanov, A Hadjadj, and D Vandromme. Numerical investigations of transition between regular and mach reflections caused by free-stream disturbances. *Shock Waves*, 12(2):157–165, 2002.

[27] Brian Edward Launder and Dudley Brian Spalding. The numerical computation of turbulent flows. *Computer methods in applied mechanics and engineering*, 3(2):269–289, 1974.

[28] Guillaume Layes, Georges Jourdan, and Lazhar Houas. Experimental study on a plane shock wave accelerating a gas bubble. *Physics of Fluids*, 21(7):074102, 2009. doi: https://doi.org/10.1063/1.3176474.

[29] Olivier Le Maître and Omar M Knio. *Spectral methods for uncertainty quantification: with applications to computational fluid dynamics*. Springer Science & Business Media, 2010.

[30] Jia Li and Dongbin Xiu. A generalized polynomial chaos based ensemble kalman filter with high accuracy. *Journal of computational physics*, 228(15):5454–5469, 2009.

[31] Antonio Marquina and Pep Mulet. A flux-split algorithm applied to conservative models for multicomponent compressible flows. *Journal of Computational Physics*, 185(1):120–138, 2003. doi: 10.1016/S0021-9991(02)00050-5.

[32] Benjamin Martinez. Wind resource in complex terrain with OpenFOAM. *Risø DTU, National Laboratory for Sustainable Energy*, 2011.

[33] Yucong Miao, Shuhua Liu, Bicheng Chen, Bihui Zhang, Shu Wang, and Shuyan Li. Simulating urban flow and dispersion in beijing by coupling a CFD model with the WRF model. *Advances in atmospheric sciences*, 30(6):1663, 2013.

[34] Yucong Miao, Shuhua Liu, Yijia Zheng, Shu Wang, and Bicheng Chen. Numerical study of the effects of topography and urbanization on the local atmospheric circulations over the Beijing-Tianjin-Hebei, China. *Advances in Meteorology*, 2015, 2015.

[35] Pep Moreno, Arne R Gravdahl, and Manel Romero. Wind flow over complex terrain: application of linear and CFD models. In *European wind energy conference and exhibition*, pages 16–19, 2003.

[36] YY Niu. Computations of two-fluid models based on a simple and robust hybrid primitive variable Riemann solver with AUSMD. *Journal of Computational Physics*, 308:389–410, 2016. doi: 10.1016/j.jcp.2015.12.045.

[37] William L Oberkampf and Timothy G Trucano. Verification and validation in computational fluid dynamics. *Progress in aerospace sciences*, 38(3):209–272, 2002.

[38] William L Oberkampf, M Sindir, and A Terrence Conlisk. Guide for the verification and validation of computational fluid dynamics simulations. *American Institute of Aeronautics and Astronautics, Reston, VA*, 1998.

[39] William L Oberkampf, Timothy G Trucano, and Charles Hirsch. Verification, validation, and predictive capability in computational engineering and physics. *Applied Mechanics Reviews*, 57(5):345–384, 2004.

[40] American Society of Mechanical Engineers. *Standard for Verification and Validation in Computational Fluid Dynamics and Heat Transfer: An American National Standard*. American Society of Mechanical Engineers, 2006.

[41] American Society of Mechanical Engineers. *Standard for Verification and Validation in Computational Fluid Dynamics and Heat Transfer: An American National Standard*. American Society of Mechanical Engineers, 2009.

[42] John O'Sullivan. *Modelling wind flow over complex terrain*. PhD thesis, ResearchSpace@ Auckland, 2012.

[43] AK Pandare and H Luo. A robust and efficient finite volume method for compressible inviscid and viscous two-phase flows. *Journal of Computational Physics*, 371:67–91, 2018. doi: 10.1016/j.jcp.2018.05.018.

[44] J. M. Picone and J. P. Boris. Vorticity generation by shock propagation through bubbles in a gas. *Journal of Fluid Mechanics*, 189:2351, 1988. doi: 10.1017/S0022112088000904.

[45] James J Quirk and Smadar Karni. On the dynamics of a shock–bubble interaction. *Journal of Fluid Mechanics*, 318:129–163, 1996. doi: 10.1017/S0022112096007069.

[46] Devesh Ranjan, John HJ Niederhaus, Jason G Oakley, Mark H Anderson, Riccardo Bonazza, and Jeffrey A Greenough. Shock-bubble interactions: Features of divergent shock-refraction geometry observed in experiments and simulations. *Physics of Fluids*, 20(3):036101, 2008. doi: 10.1063/1.2840198.

[47] Shafiqur Rehman, Luai M. Al-Hadhrami, Md. Mahbub Alam, and J.P. Meyer. Empirical correlation between hub height and local wind shear exponent for different sizes of wind turbines. *Sustainable Energy Technologies and Assessments*, 4:45 – 51, 2013. ISSN 2213-1388.

[48] PJ Richards and RP Hoxey. Appropriate boundary conditions for computational wind engineering models using the k-ε turbulence model. In *Computational Wind Engineering 1*, pages 145–153. Elsevier, 1993.

[49] Patrick J Roache. *Fundamentals of verification and validation*. hermosa publ., 2009.

[50] FE Sanville et al. A new method of specifying the flow capacity of pneumatic fluid power valves. *Hydraulic Pneumatic Power*, 17(195):120–126, 1971.

[51] Santhosh K Shankar, Soshi Kawai, and Sanjiva K Lele. Two-dimensional viscous flow simulation of a shock accelerated heavy gas cylinder. *Physics of Fluids*, 23(2):024102, 2011. doi: 10.1063/1.3553282.

[52] Keh-Ming Shyue. A fluid-mixture type algorithm for compressible multicomponent flow with Mie–Grüneisen equation of state. *Journal of Computational Physics*, 171(2):678–707, 2001. doi: 10.1145/2645703.

[53] Keh-Ming Shyue. A wave-propagation based volume tracking method for compressible multicomponent flow in two space dimensions. *Journal of Computational Physics*, 215(1):219–244, 2006. doi: 10.1016/j.jcp.2005.10.030.

[54] Keh-Ming Shyue. An Eulerian interface-sharpening algorithm for compressible gas dynamics. *Modeling, Simulation and Optimization of Complex Processes-HPSC 2012*, pages 221–231, 2014. doi: 10.1007/978-3-319-09063-4_18.

[55] Keh-Ming Shyue and Feng Xiao. An Eulerian interface sharpening algorithm for compressible two-phase flow: the algebraic THINC approach. *Journal of Computational Physics*, 268:326–354, 2014. doi: 10.1016/j.jcp.2014.03.010.

[56] Kwok Kai So. *Uncertainty Analysis of Shock-Bubble Interaction*. PhD thesis, Universität München, 2014.

[57] David J Stensrud and Jon A Skindlov. Gridpoint predictions of high temperature from a mesoscale model. *Weather and forecasting*, 11(1):103–110, 1996.

[58] Brandon Storm and Sukanta Basu. The wrf model forecast-derived low-level wind shear climatology over the united states great plains. *Energies*, 3(2):258–276, 2010.

[59] N Sudani, M Sato, T Karasawa, J Noda, A Tate, and M Watanabe. Irregular effects on the transition from regular to mach reflection of shock waves in wind tunnel flows. *Journal of Fluid Mechanics*, 459:167–185, 2002.

[60] Bruno Sudret. Global sensitivity analysis using polynomial chaos expansions. *Reliability engineering & system safety*, 93(7):964–979, 2008.

[61] Bruno Sudret, Stefano Marelli, and Christos Lataniotis. Sparse polynomial chaos expansions as a machine learning regression technique. In *International Symposium on Big Data and Predictive Computational Modeling*. ETH Zürich, 2015.

[62] Orkun Temel, Laurent Bricteux, and Jeroen van Beeck. Coupled wrf-openfoam study of wind flow over complex terrain. *Journal of Wind Engineering and Industrial Aerodynamics*, 174:152–169, 2018.

[63] the Joint Committee for Guides in Metrology. *Guide to the expression of uncertainty in measurement, GUM 1995, with minor modifications*. the Joint Committee for Guides in Metrology, 2008.

[64] Eleuterio F Toro. *Riemann solvers and numerical methods for fluid dynamics: a practical introduction*. Springer Science & Business Media, 2013. doi: 10.1007/b79761.

[65] Lloyd N Trefethen. Is gauss quadrature better than clenshaw–curtis? *SIAM review*, 50(1): 67–87, 2008.

[66] Timothy G Trucano, Martin Pilch, and William L Oberkampf. General concepts for experimental validation of asci code applications. Technical report, Sandia National Labs., Albuquerque, NM (US); Sandia National Labs ⋯, 2002.

[67] B van Leer. Towards the ultimate conservative difference scheme. V. a second-order sequel to Godunov's method. *Journal of Computational Physics*, 32:101–136, 1979. doi: 10.1016/0021-9991(79)90145-1.

[68] Henk Kaarle Versteeg and Weeratunge Malalasekera. *An introduction to computational fluid dynamics: the finite volume method*. Pearson education, 2007.

[69] Zhi-Hua Wang, Elie Bou-Zeid, and James A Smith. A coupled energy transport and hydrological model for urban canopies evaluated using a wireless sensor network. *Quarterly Journal of the Royal Meteorological Society*, 139(675):1643–1657, 2013.

[70] Norbert Wiener. The homogeneous chaos. *American Journal of Mathematics*, 60(4):897–936, 1938. ISSN 00029327, 10806377. URL http://www.jstor.org/stable/2371268.

[71] Andrzej A Wyszogrodzki, Shiguang Miao, and Fei Chen. Evaluation of the coupling between mesoscale-wrf and les-eulag models for simulating fine-scale urban dispersion. *Atmospheric research*, 118:324–345, 2012.

[72] F Xiao, Y Honma, and T Kono. A simple algebraic interface capturing scheme using hyperbolic tangent function. *International Journal for Numerical Methods in Fluids*, 48(9): 1023–1040, 2005. doi: 10.1016/S0021-9991(02)00050-5.

[73] Feng Xiao, Satoshi Ii, and Chungang Chen. Revisit to the THINC scheme: A simple algebraic VOF algorithm. *Journal of Computational Physics*, 230(19):7086 – 7092, 2011. ISSN 0021-9991. doi: https://doi.org/10.1016/j.jcp.2011.06.012. URL http://www.sciencedirect.com/science/article/pii/S0021999111003615.

[74] Dongbin Xiu. Efficient collocational approach for parametric uncertainty analysis. *Commun. Comput. Phys*, 2(2):293–309, 2007.

[75] Dongbin Xiu. *Numerical Methods for Stochastic Computations: A Spectral Method Approach*. Princeton University Press, Princeton, NJ, USA, 2010. ISBN 0691142122, 9780691142128. doi: 10.2307/j.ctv7h0skv.

[76] Dongbin Xiu and George Em Karniadakis. The wiener–askey polynomial chaos for stochastic differential equations. *SIAM journal on scientific computing*, 24(2):619–644, 2002.

[77] Dongbin Xiu and George Em Karniadakis. Modeling uncertainty in flow simulations via generalized polynomial chaos. *Journal of Computational Physics*, 187(1):137 – 167, 2003. ISSN 0021-9991. doi: https://doi.org/10.1016/S0021-9991(03)00092-5. URL http://www.sciencedirect.com/science/article/pii/S0021999103000925.

[78] Dongbin Xiu and George Em Karniadakis. Modeling uncertainty in flow simulations via generalized polynomial chaos. *Journal of computational physics*, 187(1):137–167, 2003. doi: 10.1016/S0021-9991(03)00092-5.

[79] Norman J Zabusky. Vortex paradigm for accelerated inhomogeneous flows: Visiometrics for the Rayleigh-Taylor and Richtmyer-Meshkov environments. *Annual review of fluid mechanics*, 31(1):495–536, 1999. doi: 10.1146/annurev.fluid.31.1.495.

[80] Frank J Zajaczkowski, Sue Ellen Haupt, and Kerrie J Schmehl. A preliminary study of assimilating numerical weather prediction data into computational fluid dynamics models for wind prediction. *Journal of Wind Engineering and Industrial Aerodynamics*, 99(4):320–329, 2011.

[81] Zhigang Zhai, Ting Si, Xisheng Luo, and Jiming Yang. On the evolution of spherical gas interfaces accelerated by a planar shock wave. *Physics of Fluids*, 23(8):084104, 2011. doi: 10.1063/1.3623272.

A

Convergence of the pseudospectral collocation in case of SBI simulation

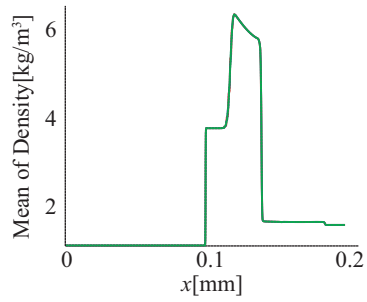

(a) Mean of density

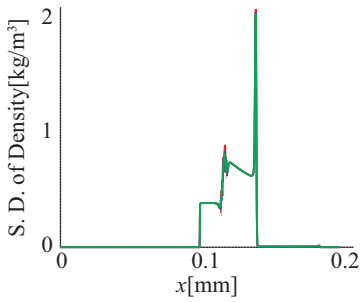

(b) Std. deviation of density

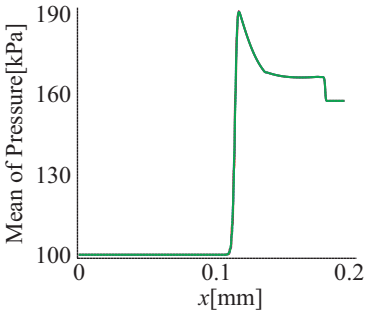

(c) Mean of pressure

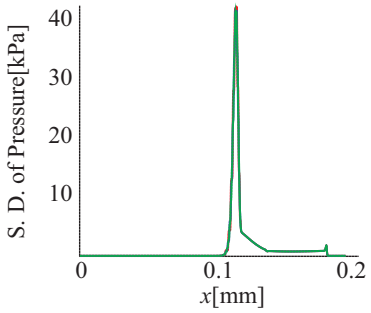

(d) Std. deviation of pressure

Fig.A.1: Statistics for density and pressure over the symmetric plane calculated with the pseudospectral collocation method using different numbers of sample simulations at 135 μs. There are three lines in each frame representing the results of the pseudospectral collocation method using 17 (red line), 33 (blue line), and 65 (green line) samples

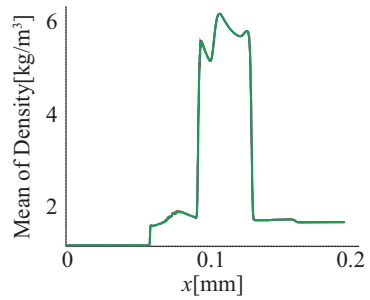

(a) Mean of density

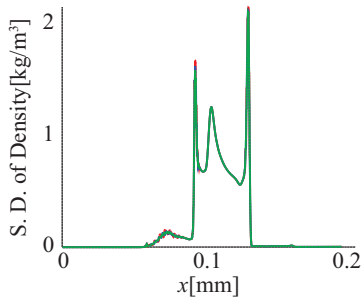

(b) Std. deviation of density

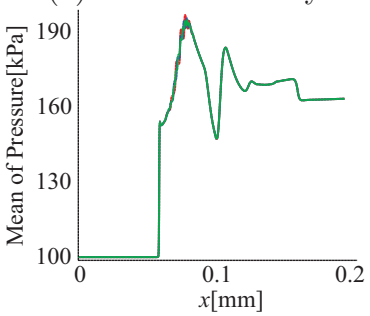

(c) Mean of pressure

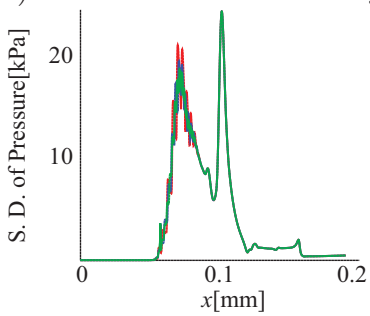

(d) Std. deviation of pressure

Fig.A.2: Same as Fig.A.1, but at 247 μs

The accuracy of the pseudospectral collocation method used for uncertainty quantification in this work depends on the number of sample simulations[75]. To confirm whether 17 sample cases are enough for the uncertainty analysis presented in this paper, we measured and compared the means and standard deviations of the converging SBI with 17, 33, and 65 samples.

The computational condition is the same as the converging case described in section 3. We compared the mean and standard deviation along the symmetric plane over the calculation domain. Figures A.1 and A.2 show the means and standard deviations evaluated with different numbers of sample cases, respectively, at different instants. We only show the results in the bubble and its neighboring region, where the refracted waves are dominant and the discrepancy among the results with different numbers of sample computations is the most significant.

Shown in Fig. A.1, the mean values of density and pressure from the results at 135 μs with 17, 33, and 65 sample cases are very small, see frames (a) and (c). The corresponding standard deviations exhibit some more visible differences, but still not substantial.

The results at 247 μs are shown in Fig. A.2. In frame (a), similar to the results at 135 μs, the mean states of density and pressure do not show a notable difference among the results with different sample cases. The standard deviation in pressure, however, shows a more visible difference around the transmitted wave in frame (d).

Despite some small discrepancies around the transmitted shock, the statistical results do not show substantial difference between the 17-sample case and other two cases with more sample simulations. Thus, the pseudospectral collocation method with 17 samples provides reliable results for both mean and standard deviation in the SBI simulations presented in this work.

B

Notion about the surrogate PCE representation of the pneumatic throttle

In chapter 5, we discussed the estimation of calculation condition using the surrogate PCE representation of numerical simulation. We used 17 points to attain the surrogate PCE representation using stochastic collocation methods. In here, we discuss about the sufficiency of the number of the collocation points used to attain the surrogate model. Fig. B.1 shows the surrogate PCE representation attained from the different number of collocation point. The difference of root square means between two lines evaluated with 201 points in the domain $\xi \in [-1 : 1]$ was 8.6×10^{-7}. This difference is not significant compared with the order of values $\times 10^{-4}$, and the 17 points are assumed as sufficient to represent the simulation system with the surrogate model.

However, the existence of the overfitting, which made the surrogate model constructed from the 17 points wavey, should be mentioned. Despite the blue line shows smooth change within the calculation region, the red line has curve upside and downside around the smooth line. As shown in this figure, despite the fact that the PCE collocation method ensure spectral convergence, overfitting phenomenon like this example could occur. Thus, the evaluation of the constructed surrogated model should be carefully performed based on knowledge about the phenomenon, not only based on the number of the collocation points.

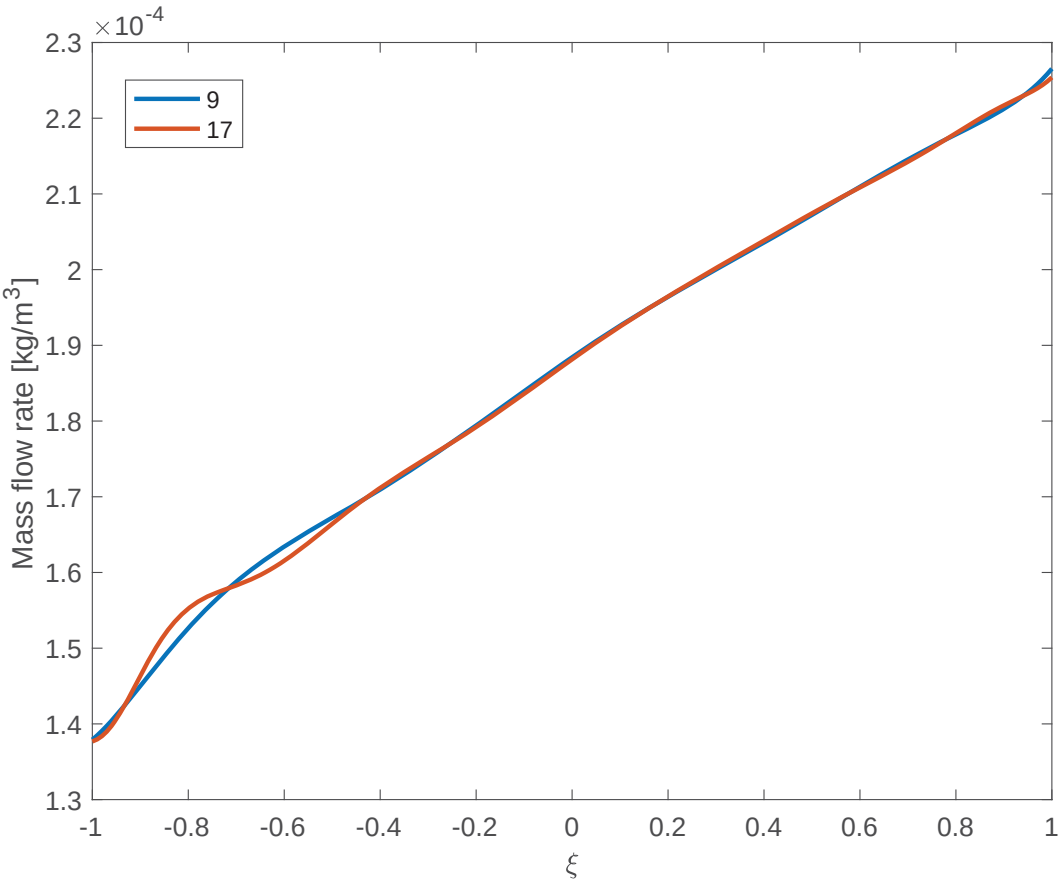

Fig.B.1: The surrogate PCE representation using stochastic collocation method with a pneumatic throttle. There are two lines with the difference of the number of collocation point: 9 (blue line) and 17 (red line)

Acknowledgment

I would like to thank all the people who contributed in some ways to this thesis. Without their guidance and support, this thesis would not have been possible. First and foremost, I would like to express my deepest appreciation to my academic advisor, Prof. Xiao, for accepting me into his group, giving me intellectual freedom in my work, supporting my attendance at various conferences, engaging me in new ideas, and providing invaluable advice ranging from daily life to future development. Those experiences will be great treasures in my whole life.

Then, I would like to thank Prof. Kagawa, who support me with both research and spirit. For the research, he gave experience with experiment and taught me practical knowledge about the fluid phenomenon, which helps me develop and conduct my research. And enormous discussions he provided me also furnished my spiritual growth. I sincerely appreciate his support for both research and sprit.

Dr. Abe is one of the most important peoples who had influenced my thesis topic. He gave valuable discussion when I determine my research topic, and I could get familiar with the topic with his guidance. Dr. Deng also had constructively adviced my research topic. With his help, I could conduct my research efficiently. Dr. Che helped me expands my research topic to a more broad field of fluid mechanics. With discussion with him, valuable knowledge about the wind forecast phenomenon could be attained, and my research field could successfully be expanded. Discussion with the Xiao labs members: especially Iida, Seki, Miyakawa, Unagami also made my research plentiful. Dr. Xie, Dr. Son, Andress, Ronit, Siengdy, Cheng, and other members of the Xiao lab made my research life more enjoyable and helped me conduct my research more productively. I present the highest gratefulness of every member of the Xiao lab who helped me reach my doctoral research accomplished.